

Electronic ISSN: 1309-0267



**International Journal  
of Engineering &  
Applied Sciences**

**I  
J  
E  
A  
S**

**IJEAS**

**Volume 10, Issue 2  
2018**

## **HONORARY EDITORS**

*(in Alphabetical)*

Prof. Atluri, S.N.- University of California, Irvine-USA

Prof. David Hui- University of New Orleans, USA

Prof. Ferreira, A.- Universidade do Porto, PORTUGAL

Prof. Liew, K.M.- City University of Hong Kong-HONG KONG

Prof. Lim, C.W.- City University of Hong Kong-HONG KONG

Prof. Liu, G.R.- National University of Singapore- SINGAPORE

Prof. Malekzadeh, P. — Persian Gulf University, IRAN

Prof. Nath, Y.- Indian Institute of Technology, INDIA

Prof. Omurtag, M.H. -ITU

Prof. Reddy, J.N.-Texas A& M University, USA

Prof. Saka, M.P.- University of Bahrain-BAHRAIN

Prof. Shen, H.S.- Shanghai Jiao Tong University, CHINA

Prof. Xiang, Y.- University of Western Sydney-AUSTRALIA

Prof. Wang, C.M.- National University of Singapore- SINGAPORE

Prof. Wei, G.W.- Michigan State University-USA

## **EDITOR IN CHIEF:**

Ömer Civalek — Akdeniz University *civalek@yahoo.com*

## **ASSOCIATE EDITORS:**

Asst. Prof. Ibrahim AYDOĞDU -Akdeniz University *aydogdu@akdeniz.edu.tr*

Asst. Prof. Sevil Köfteci -Akdeniz University *skofteci@akdeniz.edu.tr*

R.A. Kadir MERCAN -Akdeniz University *mercankadir@akdeniz.edu.tr*

## **EDITORIAL BOARD**

*(The name listed below is not Alphabetical or any title scale)*

Prof. David Hui -University of New Orleans

Prof. Xinwei Wang -Nanjing University of Aeronautics and Astronautics

Asst. Prof. Francesco Tornabene -University of Bologna

Asst. Prof. Nicholas Fantuzzi -University of Bologna

Asst. Prof. Keivan Kiani – K.N. Toosi University of Technology

R. A. Michele Baccocchi -University of Bologna

Asst. Prof. Hamid M. Sedighi -Shahid Chamran University of Ahvaz

Assoc. Prof. Yaghoub Tadi Beni -Shahrekord University

Assoc. Prof. Raffaele Barretta -University of Naples Federico II

Assoc. Prof. Meltem ASİLTÜRK -Akdeniz University meltemasilturk@akdeniz.edu.tr

Asst. Prof. Ferhat Erdal -Akdeniz University eferhat@akdeniz.edu.tr

Prof. Metin AYDOĞDU -Trakya University metina@trakya.edu.tr

Prof. Ayşe DALOĞLU – KTU aysed@ktu.edu.tr

Prof. Candan GÖKCEOĞLU – Hacettepe University cgokce@hacettepe.edu.tr

Prof. Oğuzhan HASANÇEBİ – METU oguzhan@metu.edu.tr

Asst. Prof. Rana MUKHERJĪ – The ICFAI University

Assoc. Prof. Baki ÖZTÜRK – Hacettepe University

Assoc. Prof. İbrahim ATMACA -Akdeniz Universityatmaca@akdeniz.edu.tr

Assoc. Prof. Yılmaz AKSU -Akdeniz University

Assoc. Prof. Hakan ERSOY- Akdeniz University

Assoc. Prof. Mustafa Özgür YAYLI -Uludağ University

Prof. Hakan F. ÖZTOP – Fırat University

Assoc. Prof. Selim L. SANİN – Hacettepe University

Assoc. Prof. Ayla DOĞAN -Akdeniz University

Asst. Prof. Engin EMSEN -Akdeniz University

Asst. Prof. Rifat TÜR – Akdeniz University

Prof. Serkan DAĞ – METU

Prof. Ekrem TÜFEKÇİ – İTÜ

## ABSTRACTING & INDEXING



IJEAS provides unique DOI link to every paper published.

## EDITORIAL SCOPE

The journal presents its readers with broad coverage across some branches of engineering and science of the latest development and application of new solution algorithms, artificial intelligent techniques innovative numerical methods and/or solution techniques directed at the utilization of computational methods in solid and nano-scaled mechanics.

International Journal of Engineering & Applied Sciences (IJEAS) is an Open Access Journal

International Journal of Engineering & Applied Sciences (IJEAS) publish original contributions on the following topics:

Numerical Methods in Solid Mechanics

Nanomechanic and applications

Microelectromechanical systems (MEMS)

Vibration Problems in Engineering

Higher order elasticity (Strain gradient, couple stress, surface elasticity, nonlocal elasticity)

Applied Mathematics

IJEAS allows readers to read, download, copy, distribute, print, search, or link to the full texts of articles.



## CONTENTS

### **Several Stress Resultant and Deflection Formulas for Euler-Bernoulli Beams under Concentrated and Generalized Power/Sinusoidal Distributed Loads**

*By Vebil Yıldırım* ..... 35-63

### **Numerical Modelling of Wheel on the Snow**

*By Mesut Tigdemir, Mahyar Jafarzadyeganeh, Mehmet Çağrı Bayrak, Mehmet Avcar* ..... 64-72

### **Closed-Form Formulas for Hyperbolically Tapered Rotating Disks Made of Traditional Materials under Combined Thermal and Mechanical Loads**

*By Vebil Yıldırım* ..... 73-92

### **On The Stability Analysis of The General Mathematical Modeling of Bacterial Infection**

*By Bahatdin Daşbaşı, İlhan Öztürk* ..... 93-117

### **Thermo-Structural Analysis of First Stage Gas Turbine Rotor Blade Materials for Optimum Service Performance**

*By Aniekan Ikpe E., Oghenefejiro Efe-Ononeme E., Godfrey Ariavie O.* ..... 118-130

### **Derivation of Nonlocal Finite Element Formulation for Nano Beams**

*By Hayri Metin Numanoğlu , Büşra Uzun , Ömer Civalek* ..... 131-139

## Several Stress Resultant and Deflection Formulas for Euler-Bernoulli Beams under Concentrated and Generalized Power/Sinusoidal Distributed Loads

Vebil Yıldırım

Department of Mechanical Engineering, Faculty of Engineering, University of Çukurova, Adana

E-mail address: [vebil@cu.edu.tr](mailto:vebil@cu.edu.tr)

ORCID numbers of authors:  
0000-0001-9955-8423

Received date: 04.06.2018

Accepted date: 08.06.2018

### Abstract

In the present paper, the transfer matrix method based on the Euler-Bernoulli beam theory is exploited to originally achieve some exact analytical formulas for classically supported beams under both the concentrated and generalized power/sinusoidal distributed loads. A general solution procedure is also presented to consider different loads and boundary conditions. Those closed-form formulas can be used in a variety of engineering applications as well as benchmark solutions.

**Keywords:** Transfer matrix method, initial value problem, exact solution, Euler-Bernoulli beam, distributed loads.

### 1. Introduction

As is well known Euler-Bernoulli beam theory called classical beam theory is founded on the following assumptions: i) The cross section of the beam does not significantly deform under applied loads and can be assumed as rigid, ii) The cross section of the beam remains planar and normal to the deformed axis of the beam during the deformation. Due to the assumptions given above, in Euler-Bernoulli beams, which are very good for thin beam applications, transverse shear stress is not taken into account contrary to Timoshenko beams, which are good for thick beams. In Timoshenko beams the cross-section remains planar but does not remain normal to the neutral axis after bending. The basis of Euler-Bernoulli beam theory are well introduced in the text books in engineering educational system. There are also some engineering handbooks which cover Euler-Bernoulli exact solutions of many certain types of problems [1-3]. The present study aims at adding some remarkable closed-form formulas to the deep open repository for Euler-Bernoulli beam bending formulas. To this end the transfer matrix approach which is one of the initial value problem (IVP) solver methods is employed [4-6].

### 2. Application of the Transfer Matrix Method

Let  $x$  be the beam axis (Fig. 1). The governing homogeneous differential equation set for the out-of-plane bending analysis of the beam having uniform section in canonical form is given by [4]



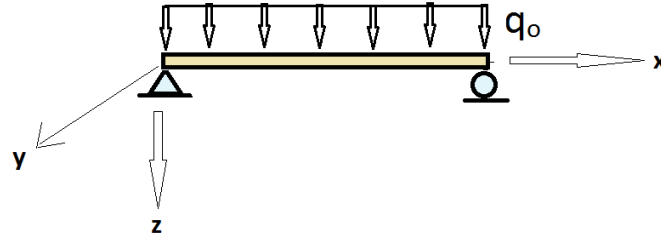


Fig. 1. A beam under uniformly distributed forces

$$\frac{dw(x)}{dx} = -\theta(x), \quad \frac{d\theta(x)}{dx} = \frac{M(x)}{EI}, \quad \frac{dM(x)}{dx} = T(x), \quad \frac{dT(x)}{dx} = 0 \quad (1)$$

where  $w(x)$  is the transverse displacement,  $\theta(x)$  is the rotation,  $M(x)$  is the bending moment, and  $T(x)$  is the shear force. By using the prime symbol for the derivative of the related quantity with respect to  $x$ , Eq. (1) may be written in a compact form as

$$\mathbf{S}'(x) = \begin{bmatrix} 0 & -1 & 0 & 0 \\ 0 & 0 & \frac{1}{EI} & 0 \\ 0 & 0 & 0 & 1 \\ 0 & 0 & 0 & 0 \end{bmatrix} \begin{Bmatrix} w(x) \\ \theta(x) \\ M(x) \\ T(x) \end{Bmatrix} = \mathbf{D} \mathbf{S}(x) \quad (2)$$

where  $\mathbf{S}(x)$  is called the state vector which comprises the cross-sectional quantities at a positive section, and  $\mathbf{D}$  is the differential matrix. Characteristic equation of the differential matrix is

$$|\mathbf{D} - \lambda \mathbf{I}| = \lambda^4 = 0 \quad (3)$$

where  $\mathbf{I}$  refers the unit matrix. Cayley-Hamilton theorem states that every square matrix satisfies its own characteristic equation, and so  $\mathbf{D}^4 = 0$ . Equation (3) suggests that the higher powers of the differential matrix which are equal or greater than four are identically zero. The transfer matrix satisfies the similar type of differential equation for the state vector given in Eq. (2),

$\mathbf{F}'(x) = \mathbf{D} \mathbf{F}(x)$ . If the elements of the differential matrix are constants as in Eq. (2), it is possible to get an exact solution to the transfer matrix. In this case, solution of  $\mathbf{F}'(x) = \mathbf{D} \mathbf{F}(x)$  with the initial conditions,  $\mathbf{F}(x = 0) = \mathbf{I}$ , gives us the exact transfer matrix in the form of a matrix exponential

$$\mathbf{F}(x) = e^{x\mathbf{D}} = \mathbf{I} + x\mathbf{D} + \frac{x^2}{2!}\mathbf{D}^2 + \frac{x^3}{3!}\mathbf{D}^3 \quad (4)$$

In the series solution in Eq. (4), the remaining terms including forth and higher than forth powers of the differential matrix are taken as identical to the zero since  $\mathbf{D}^4 = 0$ .

$$\mathbf{F}(x) = \begin{bmatrix} 1 & -x & -\frac{x^2}{2EI} & -\frac{x^3}{6EI} \\ 0 & 1 & \frac{x}{EI} & \frac{x^2}{2EI} \\ 0 & 0 & 1 & x \\ 0 & 0 & 0 & 1 \end{bmatrix} \quad (5)$$

Suppose that a beam is subjected to both a distributed force  $q(x)$  and a distributed couple moment  $m(x)$  along the beam axis. together with a concentrated force  $P_o$  and a couple moment  $\mu_o$  acting at section  $x = a$ . Under this assumption, the overall transfer matrix relates the state vectors at both ends of the beam as follows

$$\mathbf{S}(L) = \mathbf{F}(L)\mathbf{S}(0) + \int_0^L \mathbf{F}(L - \xi)\mathbf{k}(\xi) d\xi + \mathbf{F}(L - a)\mathbf{K}(a) \quad (6)$$

where

$$\mathbf{S}(L) = \begin{Bmatrix} w(L) \\ \theta(L) \\ M(L) \\ T(L) \end{Bmatrix} = \begin{Bmatrix} w_L \\ \theta_L \\ M_L \\ T_L \end{Bmatrix} \quad (7)$$

$$\mathbf{F}(L - \xi) = \begin{bmatrix} 1 & \xi - L & -\frac{(L - \xi)^2}{2EI} & -\frac{(L - \xi)^3}{6EI} \\ 0 & 1 & \frac{L - \xi}{EI} & \frac{(L - \xi)^2}{2EI} \\ 0 & 0 & 1 & L - \xi \\ 0 & 0 & 0 & 1 \end{bmatrix} \quad (8)$$

$$\mathbf{S}(0) = \begin{Bmatrix} w(0) \\ \theta(0) \\ M(0) \\ T(0) \end{Bmatrix} = \begin{Bmatrix} w_o \\ \theta_o \\ M_o \\ T_o \end{Bmatrix} \quad (9)$$

$$\mathbf{k}(\xi) = \begin{Bmatrix} 0 \\ 0 \\ -m(\xi) \\ -q(\xi) \end{Bmatrix} \quad (10)$$

and

$$\mathbf{K}(a) = \begin{Bmatrix} 0 \\ 0 \\ -\mu_o \\ -P_o \end{Bmatrix} \quad (11)$$

In Eq. (6), column matrix  $\mathbf{k}(\xi)$  signifies the nonhomogeneous solution due to the distributed forces, and  $\mathbf{K}(a)$  is referred to as a discontinuity matrix due to the concentrated intermediate loads. By letting

$$\chi = \int_0^L \mathbf{F}(L - \xi) \mathbf{k}(\xi) d\xi, \quad \kappa = \mathbf{F}(L - a) \mathbf{K}(a) \quad (12)$$

Eq. (6) reads

$$\begin{aligned} w_L &= F(L)_{1,1} w_o + F(L)_{1,2} \theta_o + F(L)_{1,3} M_o + F(L)_{1,4} T_o + \chi_1 + \kappa_1 \\ \theta_L &= F(L)_{2,1} w_o + F(L)_{2,2} \theta_o + F(L)_{2,3} M_o + F(L)_{2,4} T_o + \chi_2 + \kappa_2 \\ M_L &= F(L)_{3,1} w_o + F(L)_{3,2} \theta_o + F(L)_{3,3} M_o + F(L)_{3,4} T_o + \chi_3 + \kappa_3 \\ T_L &= F(L)_{4,1} w_o + F(L)_{4,2} \theta_o + F(L)_{4,3} M_o + F(L)_{4,4} T_o + \chi_4 + \kappa_4 \end{aligned} \quad (13)$$

Boundary conditions for the beam considered in the present study is given in Table 1. In the transfer matrix method, it is necessary to determine all the elements of the initial state vector to get a general solution to the problem. Some of elements of the initial state vector may be given directly as boundary conditions. To find the remaining unknown ones, the boundary conditions given at both ends should be implemented into Eq. (18) by considering Table 1. After determining of the full elements of the initial state vector, all sectional quantities at any section may be easily computed as follows

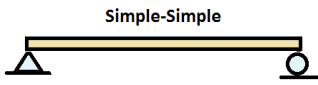
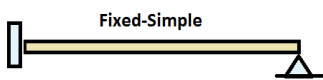
$$\text{For } (0 \leq x < a), \quad \mathbf{S}^I(x) = \mathbf{F}(x) \mathbf{S}(0) + \int_0^x \mathbf{F}(x - \xi) \mathbf{k}(\xi) d\xi \quad (14)$$

$$\text{For } (a \leq x \leq L), \quad \mathbf{S}^{II}(x) = \mathbf{F}(x) \mathbf{S}(0) + \int_0^x \mathbf{F}(x - \xi) \mathbf{k}(\xi) d\xi + \mathbf{F}(x - a) \mathbf{K}(a)$$

If there are more than one discontinuities along the beam axis the following may be observed [4].

$$\mathbf{S}(x) = \mathbf{F}(x) \mathbf{S}(0) + \int_0^x \mathbf{F}(x - \xi) \mathbf{k}(\xi) d\xi + \sum_{i=1}^n \mathbf{F}(x - \xi_i) \mathbf{K}(\xi_i) \quad (15)$$

Table 1. Boundary conditions considered

Classically supported beams		$x = 0$	$x = L$
Simple-Simple (S-S)		$w_o = 0, M_o = 0$	$w_L = 0, M_L = 0$
Clamped-Clamped (C-C)		$w_o = 0, \theta_o = 0$	$w_L = 0, \theta_L = 0$
Clamped-Free (C-F)		$w_o = 0, \theta_o = 0$	$T_L = 0, M_L = 0$
Clamped-Simple (C-S)		$w_o = 0, \theta_o = 0$	$w_L = 0, M_L = 0$

In the following sections the analytical formulas are to be presented for beams under separate distributed and concentrated loads. Since small deformations are assumed, the superposition principle is hold when necessary.

### 3. Solutions for Uniformly Distributed Forces

For only uniformly distributed forces and couple moments acting along the beam,

$$q(x) = -q_o, \quad m(x) = -m_d \quad (16)$$

a general solution takes the following form ( $0 \leq x \leq L$ )

$$\mathbf{S}(x) = \mathbf{F}(x)\mathbf{S}(0) + \int_0^x \mathbf{F}(x - \xi)\mathbf{k}(\xi) d\xi = \mathbf{F}(x)\mathbf{S}(0) + \begin{pmatrix} \frac{x^3(4m_d + xq_o)}{24EI} \\ -\frac{x^2(3m_d + xq_o)}{6EI} \\ -\frac{1}{2}x(2m_d + xq_o) \\ -xq_o \end{pmatrix} \quad (17)$$

#### 3.1. S-S Beam under Uniformly Distributed Loads

Distribution of stress resultants, displacements and rotations in a simply supported beam are found as

$$\begin{aligned} \mathbf{S}_{S-S}^E(x) &= \begin{pmatrix} w(x) \\ \theta(x) \\ M(x) \\ T(x) \end{pmatrix}_{S-S} = \mathbf{F}(x)\mathbf{S}(0) + \int_0^x \mathbf{F}(x - \xi)\mathbf{k}(x) d\xi \\ &= \mathbf{F}(x) \begin{pmatrix} 0 \\ -\frac{L^3 q_o}{24EI} \\ 0 \\ m_d + \frac{Lq_o}{2} \end{pmatrix} + \begin{pmatrix} \frac{x^3(4m_d + xq_o)}{24EI} \\ -\frac{x^2(3m_d + xq_o)}{6EI} \\ -\frac{1}{2}x(2m_d + xq_o) \\ -xq_o \end{pmatrix} = \begin{pmatrix} \frac{x(L^3 - 2Lx^2 + x^3)q_o}{24EI} \\ \frac{(L^3 - 6Lx^2 + 4x^3)q_o}{24EI} \\ \frac{1}{2}x(L - x)q_o \\ m_d + \frac{1}{2}(L - 2x)q_o \end{pmatrix} \end{aligned} \quad (18)$$

For the sake of comparison the followings values at specific sections may be used.

$$\begin{aligned} w_{L/2} &= \frac{5L^4 q_o}{384EI} \\ \theta_o &= -\frac{L^3 q_o}{24EI}, \quad \theta_{L/2} = 0, \quad \theta_L = \frac{L^3 q_o}{24EI} \end{aligned} \quad (19a)$$

$$\begin{aligned} M_{L/2} &= \frac{L^2 q_o}{8} \\ T_o &= m_d + \frac{Lq_o}{2}, \quad T_{L/2} = m_d, \quad T_L = m_d - \frac{Lq_o}{2} \end{aligned} \quad (19b)$$

Comparison of Bernoulli-Euler and Timoshenko beam's dimensionless displacements,  $\bar{w}$ , when  $m_d = 0$  is shown in Fig. 2.

$$\bar{w} = \frac{EI}{q_o L^4} w \quad (20)$$

For  $L/h = 10, 20, 50,$  and  $100$ , the maximum displacements in Euler beam remain constant as  $\bar{w}_{max}^E = 0.0130208$  while it takes different values in Timoshenko beams as  $\bar{w}_{max}^T = 0.0133458, 0.0131021, 0.0130338,$  and  $0.0130241$ , respectively. The maximum displacements in a S-S Euler beam is found as  $\bar{w}_{max}^E = 0.013130$  in Ref. [7], as  $\bar{w}_{max}^E = 0.013152$  in Ref. [8], and as  $\bar{w}_{max}^E = 0.0130208$  in Ref. [9].

It is worth noting that there is no difference in the values of rotation, bending moment, and shearing force in S-S beams subjected to a uniform distributed force along the beam based on the two beam theories. From Fig. 3, it is observed that Timoshenko's beam theory gives somewhat higher displacements in S-S beams than Euler-Bernoulli beam theory.

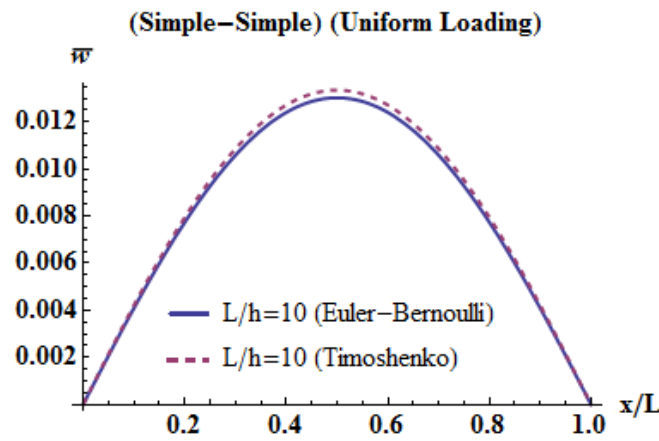


Fig. 2. Dimensionless transverse displacements in a S-S beam based on the two beam theories

### 3.2. C-S Beam under Uniformly Distributed Loads

Variations of stress resultants, displacements and rotations in a fixed-simple supported Euler-Bernoulli beam along the beam axis are

$$\mathbf{S}_{C-S}^E(x) = \begin{Bmatrix} w(x) \\ \theta(x) \\ M(x) \\ T(x) \end{Bmatrix}_{C-S} = \mathbf{F}(x)\mathbf{S}(0) + \int_0^x \mathbf{F}(x-\xi)\mathbf{k}(x) d\xi \quad (21a)$$

$$= \mathbf{F}(x) \begin{Bmatrix} 0 \\ 0 \\ -\frac{1}{8}L^2q_o \\ m_d + \frac{5Lq_o}{8} \end{Bmatrix} + \begin{Bmatrix} \frac{x^3(4m_d + xq_o)}{24EI} \\ -\frac{x^2(3m_d + xq_o)}{6EI} \\ -\frac{1}{2}x(2m_d + xq_o) \\ -xq_o \end{Bmatrix} = \begin{Bmatrix} \frac{x^2(3L-2x)(L-x)q_o}{48EI} \\ -\frac{x(6L^2-15Lx+8x^2)q_o}{48EI} \\ -\frac{1}{8}(L-4x)(L-x)q_o \\ m_d + \frac{1}{8}(5L-8x)q_o \end{Bmatrix}$$

$$(21b)$$

Some specific values of Eq. (21) are as follows

$$\begin{aligned}
 w_{L/2} &= \frac{L^4 q_0}{192EI} \\
 \theta_o &= 0, \quad \theta_{L/2} = -\frac{L^3 q_0}{192EI}, \quad \theta_L = \frac{L^3 q_0}{48EI} \\
 M_o &= -\frac{1}{8}L^2 q_0, \quad M_{L/2} = \frac{L^2 q_0}{16}, \quad M_L = 0 \\
 T_o &= m_d + \frac{5Lq_0}{8}, \quad T_{L/2} = m_d + \frac{Lq_0}{8}, \quad T_L = m_d - \frac{3Lq_0}{8}
 \end{aligned} \tag{22}$$

Elementary theory states that the maximum displacement occurs approximately at  $x = (1 - 0.421535)L$  [3]. For  $L/h = 10, 20, 50$ , and  $100$ , the dimensionless displacements in Euler beam at the section of  $x/L = 0.6$  remain constant as  $\bar{w}_{x/L=0.6}^E = 0.0054$  while it takes different values in Timoshenko beams as  $\bar{w}_{x/L=0.6}^T = 0.00576618, 0.00549162, 0.00541466$ , and  $0.00540367$ , respectively. The transverse deflection was found as  $\bar{w}_{x/L=0.5}^E = 0.00520833$  in both the present study and in Ref. [9]. It may be noted that there are also differences in the bending moment, shearing force, and the rotation in a C-S beam based on the two beam theories. Figure 3 shows the dimensionless transverse displacements in a C-S beam based on the two beam theories. In a C-S beam the differences in the results of the two beam theories become much clearer than S-S beam.

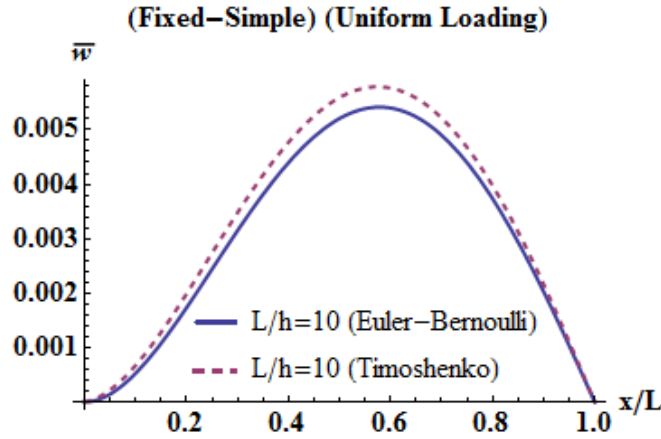


Fig. 3. Dimensionless transverse displacements in a C-S beam based on the two beam theories

### 3.3. C-F Beam under Uniformly Distributed Loads

Stress resultants, displacements and rotations in a fixed-free supported beam vary along the beam axis as

$$\mathbf{S}_{C-F}^E(\mathbf{x}) = \begin{Bmatrix} w(x) \\ \theta(x) \\ M(x) \\ T(x) \end{Bmatrix}_{C-F} = \mathbf{F}(x)\mathbf{S}(0) + \int_0^x \mathbf{F}(x-\xi)\mathbf{k}(x) d\xi \tag{23a}$$

$$\begin{aligned}
 \mathbf{S}_{C-F}^E(x) &= \mathbf{F}(x) \begin{Bmatrix} 0 \\ 0 \\ Lm_d - \frac{L^2q_o}{2} \\ Lq_o \end{Bmatrix} + \begin{Bmatrix} \frac{x^3(4m_d + xq_o)}{24EI} \\ -\frac{x^2(3m_d + xq_o)}{6EI} \\ -\frac{1}{2}x(2m_d + xq_o) \\ -xq_o \end{Bmatrix} \\
 &= \begin{Bmatrix} \frac{x^2(4m_d(x-3L) + (6L^2 - 4Lx + x^2)q_o)}{24EI} \\ -\frac{x(3m_d(x-2L) + (3L^2 - 3Lx + x^2)q_o)}{6EI} \\ \frac{1}{2}(L-x)(2m_d + (x-L)q_o) \\ (L-x)q_o \end{Bmatrix} \quad (23b)
 \end{aligned}$$

Certain values of sectional quantities in a C-F beam are

$$\begin{aligned}
 w_{L/2} &= \frac{L^3(17Lq_o - 40m_d)}{384EI}, \quad w_L = \frac{L^3(3Lq_o - 8m_d)}{24EI} \\
 \theta_{L/2} &= \frac{L^2(18m_d - 7Lq_o)}{48EI}, \quad \theta_L = -\frac{L^2(Lq_o - 3m_d)}{6EI} \\
 M_o &= Lm_d - \frac{L^2q_o}{2}, \quad M_{L/2} = -\frac{1}{8}L(Lq_o - 4m_d) \\
 T_o &= Lq_o, \quad T_{L/2} = \frac{Lq_o}{2}, T_L = 0
 \end{aligned} \quad (24)$$

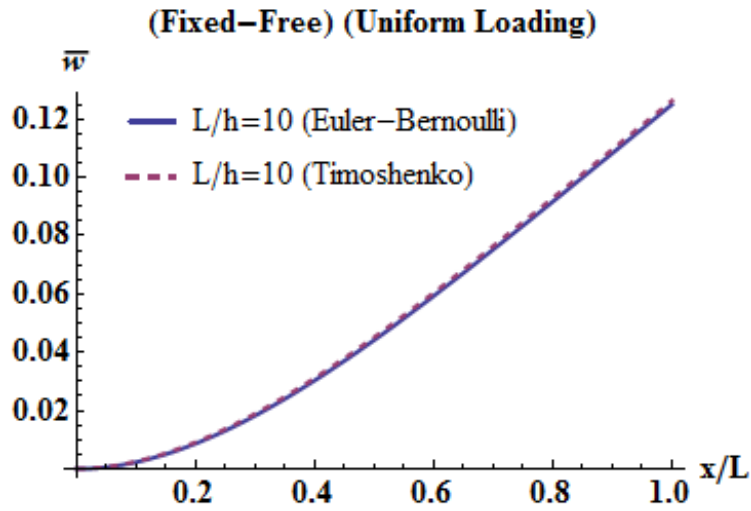


Fig. 4. Dimensionless transverse displacements in a C-F beam based on the two beam theories

Dimensionless transverse displacements in a C-F beam based on the two beam theories is illustrated in Fig. 4 when the beam is subjected only distributed uniform forces. Euler-Bernoulli displacements are again independent from  $L/h$  ratios. The maximum displacement in an Euler-Bernoulli beam is calculated at the free end as  $\bar{w}_L^E = 0.125$ . In Timoshenko beams, those values are to be  $\bar{w}_L^T = 0.1263$  ( $L/h = 10$ ),  $0.125325$  ( $L/h = 20$ ),  $0.125052$  ( $L/h = 50$ ), and  $0.125013$  ( $L/h = 100$ ). Similar to the S-S beam, there is no difference between the results of two beam theories for the rotations, bending moments and shear forces in a C-F beam.

### 3.4. C-C Beam under Uniformly Distributed Loads

Let's consider a fixed-fixed beam. Analytical formulas derived are as follows

$$\begin{aligned} \mathbf{S}_{C-C}^E(x) &= \begin{Bmatrix} w(x) \\ \theta(x) \\ M(x) \\ T(x) \end{Bmatrix}_{C-C} = \mathbf{F}(x)\mathbf{S}(0) \int_0^x \mathbf{F}(x-\xi)\mathbf{k}(x) d\xi \\ &= \mathbf{F}(x) \left\{ \begin{array}{c} 0 \\ 0 \\ -\frac{1}{12}L^2q_o \\ \frac{Lq_o}{2} \end{array} \right\} + \left\{ \begin{array}{c} \frac{x^3(4m_d + xq_o)}{24EI} \\ -\frac{x^2(3m_d + xq_o)}{6EI} \\ -\frac{1}{2}x(2m_d + xq_o) \\ -xq_o \end{array} \right\} = \left\{ \begin{array}{c} \frac{x^2(L-x)^2q_o}{24EI} \\ -\frac{x(L-2x)(L-x)q_o}{12EI} \\ -\frac{1}{12}(L^2 - 6Lx + 6x^2)q_o \\ m_d + \frac{1}{2}(L-2x)q_o \end{array} \right\} \end{aligned} \quad (25)$$

Selected values of sectional quantities in a C-C beam are

$$\begin{aligned} w_{L/2} &= \frac{L^4q_o}{384EI} \\ \theta_o = \theta_{L/2} = \theta_L &= 0 \\ M_o = -\frac{1}{12}L^2q_o, \quad M_{L/2} &= \frac{L^2q_o}{24}, \quad M_L = -\frac{1}{12}L^2q_o \\ T_o = m_d + \frac{Lq_o}{2}, \quad T_{L/2} &= m_d, \quad T_L = m_d - \frac{Lq_o}{2} \end{aligned} \quad (26)$$

Variation of the dimensionless transverse displacement in a C-C beam is demonstrated in Fig. 5 for  $q(x) = q_o$ . As seen from Fig. 5, the maximum dimensionless transverse displacement in a C-C beam occurs at the mid-span of the beam. Based on the Euler-Bernoulli beam theory, the maximum displacement is evaluated as  $\bar{w}_{max}^E = 0.00260417$ . In Timoshenko beams, these values are to be  $\bar{w}_{max}^T = 0.00292917$  ( $L/h = 10$ ),  $0.00268542$  ( $L/h = 20$ ),  $0.00261717$  ( $L/h = 50$ ), and  $0.00260742$  ( $L/h = 100$ ). Similar to the S-S and C-F beams, there is no difference between the results of two beam theories for the rotations, bending moments and shear forces in a C-C beam under uniformly distributed forces.

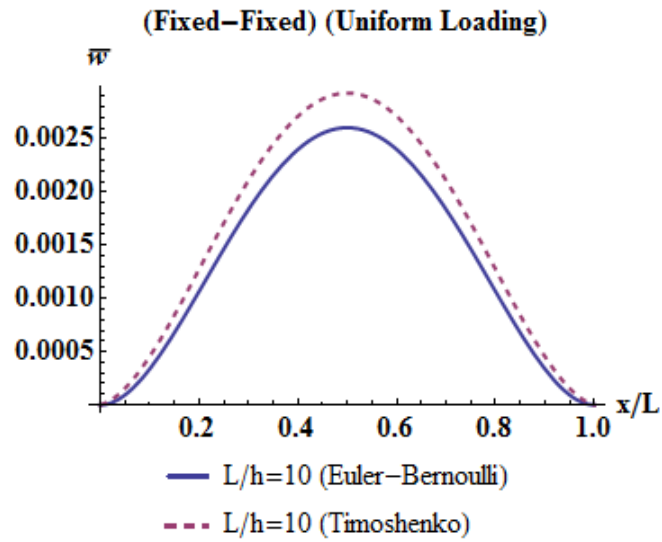


Fig. 5. Dimensionless transverse displacements in a C-C beam based on the two beam theories

#### 4. Solutions for Sinusoidal Distributed Forces

A generalized sinusoidal distributed force [10] may be in the form of (Fig. 6)

$$q(x) = -q_o \sin\left(\frac{n\pi x}{L}\right), \quad n \geq 0 \tag{27}$$

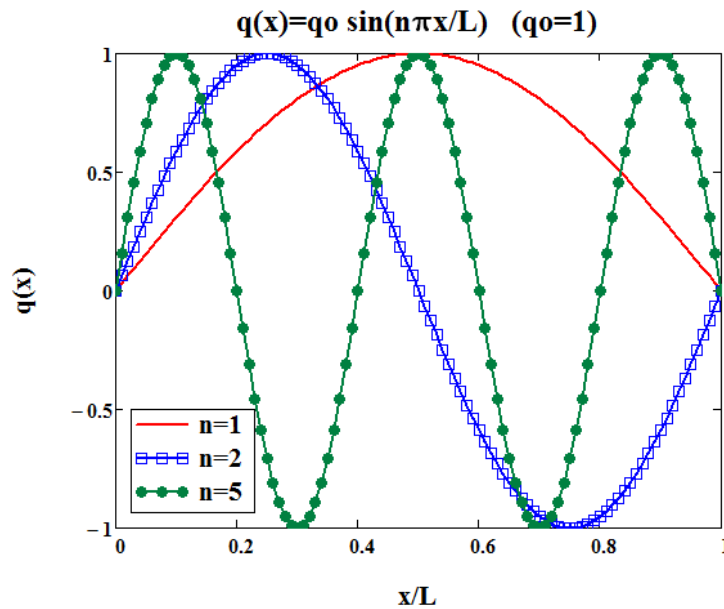


Fig. 6. Generalized sinusoidal loading

In the case of sinusoidal distributed forces in Eq. (27), the particular solution becomes

$$\int_0^x \mathbf{F}(x - \xi) \mathbf{k}(\xi) d\xi = \left\{ \begin{array}{l} \frac{Lq_o \left( 6L^3 \sin\left(\frac{\pi n x}{L}\right) - 6\pi L^2 n x + \pi^3 n^3 x^3 \right)}{6\pi^4 E I n^4} \\ - \frac{Lq_o \left( 2L^2 \cos\left(\frac{\pi n x}{L}\right) - 2L^2 + \pi^2 n^2 x^2 \right)}{2\pi^3 E I n^3} \\ \frac{Lq_o \left( L \sin\left(\frac{\pi n x}{L}\right) - \pi n x \right)}{\pi^2 n^2} \\ \frac{Lq_o \left( \cos\left(\frac{\pi n x}{L}\right) - 1 \right)}{\pi n} \end{array} \right\} \quad (28)$$

A general solution takes the form of  $\mathbf{S}(x) = \mathbf{F}(x)\mathbf{S}(0) + \int_0^x \mathbf{F}(x - \xi)\mathbf{k}(\xi) d\xi$ .

#### 4.1. S-S Beam under Sinusoidal Distributed Loads

The rotation of the section about y- axis and the shearing force at the initial end is found as ( $w_o = 0, M_o = 0$ )

$$\theta_o = \frac{L^3 ((\pi^2 n^2 + 6) \sin(\pi n) - 6\pi n) q_o}{6\pi^4 E I n^4} \quad (29)$$

$$T_o = \frac{L(\pi n - \sin(\pi n)) q_o}{\pi^2 n^2}$$

With the help of Eq. (29), the general solution in a closed form is obtained for simply supported beam under a general sinusoidal load as follows

$$\mathbf{S}(x)_{S-S}^E = \left\{ \begin{array}{l} \frac{Lq_o \left( \begin{array}{l} 6L^3 \sin\left(\frac{\pi n x}{L}\right) \\ + x \sin(\pi n) (\pi^2 n^2 x^2 - L^2 (\pi^2 n^2 + 6)) \end{array} \right)}{6\pi^4 E I n^4} \\ \frac{Lq_o \left( \begin{array}{l} \sin(\pi n) (L^2 (\pi^2 n^2 + 6) - 3\pi^2 n^2 x^2) \\ - 6\pi L^2 n \cos\left(\frac{\pi n x}{L}\right) \end{array} \right)}{6\pi^4 E I n^4} \\ \frac{Lq_o \left( L \sin\left(\frac{\pi n x}{L}\right) - x \sin(\pi n) \right)}{\pi^2 n^2} \\ \frac{Lq_o \left( \pi n \cos\left(\frac{\pi n x}{L}\right) - \sin(\pi n) \right)}{\pi^2 n^2} \end{array} \right\} \quad (30)$$

As may be guessed, in a S-S beam, the variation of  $\theta(x)$ ,  $M(x)$ , and  $T(x)$  remain unchanged in both beam theories. Some chosen values of the sectional quantities are

$$w_{L/2} = \frac{L^4 \left( \begin{array}{l} 16 \sin\left(\frac{\pi n}{2}\right) \\ - (\pi^2 n^2 + 8) \sin(\pi n) \end{array} \right) q_o}{16\pi^4 E I n^4}$$

$$\theta_{L/2} = \frac{L^3 q_o \left( \begin{array}{c} (\pi^2 n^2 + 24) \sin(\pi n) \\ -24\pi n \cos\left(\frac{\pi n}{2}\right) \end{array} \right)}{24\pi^4 E I n^4}, \quad \theta_L = -\frac{L^3 q_o \left( \begin{array}{c} (\pi^2 n^2 - 3) \sin(\pi n) \\ +3\pi n \cos(\pi n) \end{array} \right)}{3\pi^4 E I n^4} \quad (31)$$

$$M_{L/2} = \frac{4L^2 \sin^3\left(\frac{\pi n}{4}\right) \cos\left(\frac{\pi n}{4}\right) q_o}{\pi^2 n^2}$$

$$T_{L/2} = \frac{L q_o \left( \pi n \cos\left(\frac{\pi n}{2}\right) - \sin(\pi n) \right)}{\pi^2 n^2}, \quad T_L = \frac{L q_o (\pi n \cos(\pi n) - \sin(\pi n))}{\pi^2 n^2}$$

If  $n$  is a positive integer ( $\sin(\pi n) = 0$ ), then Eq. (30) turns to be

$$\mathbf{S}(x)_{S-S(n=\text{positive integer})}^E = \left\{ \begin{array}{c} \frac{q_o L^4 \sin\left(\frac{\pi n x}{L}\right)}{\pi^4 E I n^4} \\ - \left( \frac{q_o \pi L^3 n \cos\left(\frac{\pi n x}{L}\right)}{\pi^4 E I n^4} \right) \\ \frac{L^2 q_o \sin\left(\frac{\pi n x}{L}\right)}{\pi^2 n^2} \\ \frac{L q_o \pi n \cos\left(\frac{\pi n x}{L}\right)}{\pi^2 n^2} \end{array} \right\} \quad (32)$$

where  $w_{S-S(n=\text{positive integer})}^E = q_o L^4 \sin\left(\frac{\pi n x}{L}\right) / \pi^4 E I n^4$  overlaps with the result in Ref. [10].

#### 4.2. C-F Beam under Sinusoidal Distributed Loads

In the case of C-F beam, the unknown elements of the initial state vector becomes ( $w_o = 0, \theta_o = 0$ )

$$M_o = \frac{L^2 q_o (\pi n \cos(\pi n) - \sin(\pi n))}{\pi^2 n^2} \quad (33)$$

$$T_o = -\frac{L(\cos(\pi n) - 1)q_o}{\pi n}$$

The general solution may be written with the help of Eq. (33) as

$$S(x)_{C-F}^E = \left\{ \begin{array}{l} Lq_o \left( \begin{array}{l} 6L^3 \sin\left(\frac{\pi nx}{L}\right) \\ +\pi nx \left( \begin{array}{l} \pi nx \left( \begin{array}{l} \pi n(x-3L) \cos(\pi n) \\ +3L \sin(\pi n) \end{array} \right) \\ -6L^2 \end{array} \right) \end{array} \right) \\ \hline Lq_o \left( \begin{array}{l} \pi^2 n^2 x(x-2L) \cos(\pi n) \\ +2L \left( L \left( \cos\left(\frac{\pi nx}{L}\right) - 1 \right) \right) \\ +\pi nx \sin(\pi n) \end{array} \right) \\ \hline Lq_o \left( \begin{array}{l} L \left( \sin\left(\frac{\pi nx}{L}\right) - \sin(\pi n) \right) \\ +\pi n(L-x) \cos(\pi n) \end{array} \right) \\ \hline Lq_o \left( \begin{array}{l} \cos\left(\frac{\pi nx}{L}\right) - \cos(\pi n) \end{array} \right) \\ \hline \pi n \end{array} \right\} \quad (34)$$

Solutions for the rotation, bending moment and shearing force are found as the same in two beam theories. Some particular values of sectional quantities are

$$w_{L/2} = \frac{L^4 q_o \left( \begin{array}{l} 6 \left( \begin{array}{l} 8 \sin\left(\frac{\pi n}{2}\right) \\ +\pi n(\pi n \sin(\pi n) - 4) \end{array} \right) \\ -5\pi^3 n^3 \cos(\pi n) \end{array} \right)}{48\pi^4 EIn^4}, \quad w_L = -\frac{L^4 q_o \left( \begin{array}{l} 2\pi^3 n^3 \cos(\pi n) \\ -3(\pi^2 n^2 + 2) \sin(\pi n) \\ +6\pi n \end{array} \right)}{6\pi^4 EIn^4}$$

$$\theta_{L/2} = \frac{L^3 q_o \left( \begin{array}{l} -8 \cos\left(\frac{\pi n}{2}\right) \\ +\pi n \left( \begin{array}{l} 3\pi n \cos(\pi n) \\ -4 \sin(\pi n) \end{array} \right) + 8 \end{array} \right)}{8\pi^3 EIn^3}, \quad \theta_L = \frac{L^3 q_o \left( \begin{array}{l} (\pi^2 n^2 - 2) \cos(\pi n) \\ -2\pi n \sin(\pi n) + 2 \end{array} \right)}{2\pi^3 EIn^3} \quad (35)$$

$$M_{L/2} = \frac{L^2 q_o \left( \begin{array}{l} 2 \sin\left(\frac{\pi n}{2}\right) \\ -2 \sin(\pi n) + \pi n \cos(\pi n) \end{array} \right)}{2\pi^2 n^2}$$

$$T_{L/2} = \frac{L \left( \cos\left(\frac{\pi n}{2}\right) - \cos(\pi n) \right) q_o}{\pi n}, \quad T_L = 0$$

Since  $\sin(\pi n) = 0$  when  $n$  is a positive integer, Eq. (34) may be cast as follows

$$\mathbf{S}(x)_{C-F(n=\text{positive integer})}^E = \left\{ \begin{array}{l} Lq_o \left( \frac{6L^3 \sin\left(\frac{\pi n x}{L}\right)}{+\pi n x \left( \frac{\pi n x (\pi n (x - 3L) \cos(\pi n))}{-6L^2} \right)} \right) \\ - \frac{6\pi^4 E I n^4}{2\pi^3 E I n^3} \\ Lq_o \left( \frac{\pi^2 n^2 x (x - 2L) \cos(\pi n)}{+2L^2 \left( \cos\left(\frac{\pi n x}{L}\right) - 1 \right)} \right) \\ \frac{Lq_o \left( \frac{L \sin\left(\frac{\pi n x}{L}\right)}{+\pi n (L - x) \cos(\pi n)} \right)}{\frac{\pi^2 n^2}{\pi n}} \\ Lq_o \left( \frac{\cos\left(\frac{\pi n x}{L}\right) - \cos(\pi n)}{\pi n} \right) \end{array} \right\} \quad (36)$$

### 4.3. C-S Beam under Sinusoidal Distributed Loads

For a fixed-simple supported beam, the elements of the initial state vector are obtained as

$$\begin{aligned} w_o &= 0, & \theta_o &= 0 \\ M_o &= \frac{L^2((\pi^2 n^2 + 6) \sin(\pi n) - 6\pi n)q_o}{2\pi^4 n^4} \\ T_o &= \frac{L(2\pi n(\pi^2 n^2 + 3) - 3(\pi^2 n^2 + 2) \sin(\pi n))q_o}{2\pi^4 n^4} \end{aligned} \quad (37)$$

The elements of the state vector at any section are found as

$$\mathbf{S}(x)_{C-S}^E = \left\{ \begin{array}{l} Lq_o \left( \begin{array}{l} 4L^3 \sin\left(\frac{\pi nx}{L}\right) \\ -2\pi nx(2L^2 - 3Lx + x^2) \\ +x^2 \sin(\pi n) \left( \begin{array}{l} (\pi^2 n^2 + 2)x \\ -L(\pi^2 n^2 + 6) \end{array} \right) \end{array} \right) \\ \hline 4\pi^4 EIn^4 \\ Lq_o \left( \begin{array}{l} 2\pi n \left( \begin{array}{l} -2L^2 \cos\left(\frac{\pi nx}{L}\right) \\ +2L^2 - 6Lx + 3x^2 \end{array} \right) \\ +x \sin(\pi n) \left( \begin{array}{l} 2L(\pi^2 n^2 + 6) \\ -3(\pi^2 n^2 + 2)x \end{array} \right) \end{array} \right) \\ \hline 4\pi^4 EIn^4 \\ Lq_o \left( \begin{array}{l} \sin(\pi n) \left( \begin{array}{l} L(\pi^2 n^2 + 6) \\ -3(\pi^2 n^2 + 2)x \end{array} \right) \\ +2\pi n \left( \pi L n \sin\left(\frac{\pi nx}{L}\right) - 3L + 3x \right) \end{array} \right) \\ \hline 2\pi^4 n^4 \\ Lq_o \left( \begin{array}{l} 2\pi^3 n^3 \cos\left(\frac{\pi nx}{L}\right) \\ -3(\pi^2 n^2 + 2) \sin(\pi n) \\ +6\pi n \end{array} \right) \\ \hline 2\pi^4 n^4 \end{array} \right\} \quad (38)$$

Specific values of the elements of the state vector are

$$\begin{aligned}
 w_{L/2} &= -\frac{L^4 \left( \begin{array}{l} (\pi^2 n^2 + 10) \sin(\pi n) \\ +6\pi n - 32 \sin\left(\frac{\pi n}{2}\right) \end{array} \right) q_o}{32\pi^4 EIn^4} \\
 \theta_{L/2} &= \frac{L^3 q_o \left( \begin{array}{l} (\pi^2 n^2 + 18) \sin(\pi n) \\ -2\pi n \left( 8 \cos\left(\frac{\pi n}{2}\right) + 1 \right) \end{array} \right)}{16\pi^4 EIn^4}, \quad \theta_L = -\frac{L^3 q_o \left( \begin{array}{l} (\pi^2 n^2 - 6) \sin(\pi n) \\ +2\pi n + 4\pi n \cos(\pi n) \end{array} \right)}{4\pi^4 EIn^4} \\
 M_{L/2} &= \frac{L^2 \left( \begin{array}{l} (6 - \pi^2 n^2) \sin(\pi n) \\ +2\pi n \left( 2\pi n \sin\left(\frac{\pi n}{2}\right) - 3 \right) \end{array} \right) q_o}{4\pi^4 n^4} \\
 T_{L/2} &= \frac{Lq_o \left( \begin{array}{l} 2\pi^3 n^3 \cos\left(\frac{\pi n}{2}\right) \\ -3(\pi^2 n^2 + 2) \sin(\pi n) + 6\pi n \end{array} \right)}{2\pi^4 n^4} \\
 T_L &= \frac{Lq_o \left( \begin{array}{l} 2\pi^3 n^3 \cos(\pi n) \\ -3(\pi^2 n^2 + 2) \sin(\pi n) + 6\pi n \end{array} \right)}{2\pi^4 n^4}
 \end{aligned} \quad (39)$$

In the case of  $n$  is a positive integer then the followings are obtained from Eq. (38) ( $\sin(\pi n) = 0$  ).

$$\mathbf{S}(x)_{C-S(n=\text{positive integer})}^E = \left\{ \begin{array}{l} \frac{Lq_o \left( \begin{array}{l} 4L^3 \sin\left(\frac{\pi nx}{L}\right) \\ -2\pi nx(2L^2 - 3Lx + x^2) \end{array} \right)}{4\pi^4 EIn^4} \\ \frac{Lq_o 2\pi n \left( \begin{array}{l} -2L^2 \cos\left(\frac{\pi nx}{L}\right) \\ +2L^2 - 6Lx + 3x^2 \end{array} \right)}{4\pi^4 EIn^4} \\ \frac{Lq_o (2\pi n \left( \pi Ln \sin\left(\frac{\pi nx}{L}\right) - 3L + 3x \right))}{2\pi^4 n^4} \\ \frac{Lq_o (2\pi^3 n^3 \cos\left(\frac{\pi nx}{L}\right) + 6\pi n)}{2\pi^4 n^4} \end{array} \right\} \quad (40)$$

#### 4.4. C-S Beam under Sinusoidal Distributed Loads

In this case, the initial bending moment and the initial shearing force are found as ( $w_o = 0, \theta_o = 0$ )

$$M_o = -\frac{2L^2 q_o (\pi n (\cos(\pi n) + 2) - 3 \sin(\pi n))}{\pi^4 n^4}$$

$$T_o = \frac{Lq_o \left( \begin{array}{l} \pi n (\pi^2 n^2 + 6 \cos(\pi n) + 6) \\ -12 \sin(\pi n) \end{array} \right)}{\pi^4 n^4} \quad (41)$$

The state vector at any section reads

$$\mathbf{S}(x)_{c-c}^E = \left\{ \begin{array}{l} Lq_o \left( \begin{array}{l} L^3 \sin\left(\frac{\pi nx}{L}\right) \\ x(2x - 3L) \sin(\pi n) \\ -\pi n(x - L) \left( \begin{array}{l} -L \\ +x \cos(\pi n) \end{array} \right) \\ +x \end{array} \right) \\ \hline \pi^4 E I n^4 \\ Lq_o \left( \begin{array}{l} \pi L^2 (-n) \cos\left(\frac{\pi nx}{L}\right) \\ +(L - x) \left( \begin{array}{l} \pi n(L - 3x) \\ +6x \sin(\pi n) \end{array} \right) \\ +\pi nx(3x - 2L) \cos(\pi n) \end{array} \right) \\ \hline \pi^4 E I n^4 \\ Lq_o \left( \begin{array}{l} 6(L - 2x) \sin(\pi n) \\ +\pi n \left( \begin{array}{l} \pi L n \sin\left(\frac{\pi nx}{L}\right) \\ -4L + 6x \end{array} \right) \\ -2\pi n(L - 3x) \cos(\pi n) \end{array} \right) \\ \hline \pi^4 n^4 \\ Lq_o \left( \begin{array}{l} \pi n \left( \begin{array}{l} \pi^2 n^2 \cos\left(\frac{\pi nx}{L}\right) \\ +6 \cos(\pi n) + 6 \end{array} \right) \\ -12 \sin(\pi n) \end{array} \right) \\ \hline \pi^4 n^4 \end{array} \right. \quad (42)$$

Some values of the elements of the state vector at sections at  $x = L/2$  and  $x = L$  are

$$\begin{aligned}
 w_{L/2} &= \frac{L^4 q_o \left( \begin{array}{l} -\pi n + 8 \sin\left(\frac{\pi n}{2}\right) \\ -4 \sin(\pi n) + \pi n \cos(\pi n) \end{array} \right)}{8\pi^4 E I n^4} \\
 \theta_{L/2} &= - \frac{L^3 q_o \left( \begin{array}{l} \pi n \left( \begin{array}{l} 4 \cos\left(\frac{\pi n}{2}\right) \\ + \cos(\pi n) + 1 \end{array} \right) \\ -6 \sin(\pi n) \end{array} \right)}{4\pi^4 E I n^4} \\
 M_{L/2} &= \frac{L^2 q_o \left( \pi n \sin\left(\frac{\pi n}{2}\right) + \cos(\pi n) - 1 \right)}{\pi^3 n^3}, \quad M_L = \frac{L^2 q_o \left( \begin{array}{l} (\pi^2 n^2 - 6) \sin(\pi n) \\ +2\pi n + 4\pi n \cos(\pi n) \end{array} \right)}{\pi^4 n^4} \\
 T_{L/2} &= \frac{Lq_o \left( \begin{array}{l} \pi^3 n^3 \cos\left(\frac{\pi n}{2}\right) - 12 \sin(\pi n) \\ +6\pi n(\cos(\pi n) + 1) \end{array} \right)}{\pi^4 n^4}, \quad T_L = \frac{Lq_o \left( \begin{array}{l} \pi(\pi^2 n^2 + 6) n \cos(\pi n) \\ +6\pi n - 12 \sin(\pi n) \end{array} \right)}{\pi^4 n^4}
 \end{aligned} \quad (43)$$

When  $n$  is chosen as a positive integer ( $\sin(\pi n) = 0$ ) then

$$\mathbf{S}(x)_{C-C(n=\text{positive integer})}^E = \left\{ \begin{array}{l} Lq_o \left( \begin{array}{l} L^3 \sin\left(\frac{\pi nx}{L}\right) \\ -x\pi n(x-L) \left( \begin{array}{l} -L \\ +x\cos(\pi n) \\ +x \end{array} \right) \end{array} \right) \\ \hline \pi^4 E I n^4 \\ Lq_o \left( \begin{array}{l} \pi L^2 (-n) \cos\left(\frac{\pi nx}{L}\right) \\ +(L-x)(\pi n(L-3x)) \\ +\pi nx(3x-2L)\cos(\pi n) \end{array} \right) \\ \hline \pi^4 E I n^4 \\ Lq_o \left( \begin{array}{l} \pi n \left( \begin{array}{l} \pi L n \sin\left(\frac{\pi nx}{L}\right) \\ -4L+6x \end{array} \right) \\ -2\pi n(L-3x)\cos(\pi n) \end{array} \right) \\ \hline \pi^4 n^4 \\ Lq_o \pi n \left( \begin{array}{l} \pi^2 n^2 \cos\left(\frac{\pi nx}{L}\right) \\ +6\cos(\pi n) + 6 \end{array} \right) \\ \hline \pi^4 n^4 \end{array} \right\} \quad (44)$$

### 5. Solutions for Parabolically Distributed Forces

If a generalized power-type distributed force [10] is concerned (Fig. 7)

$$q(x) = -q_o \left(\frac{x}{L}\right)^n, \quad n \geq 0 \quad (45)$$

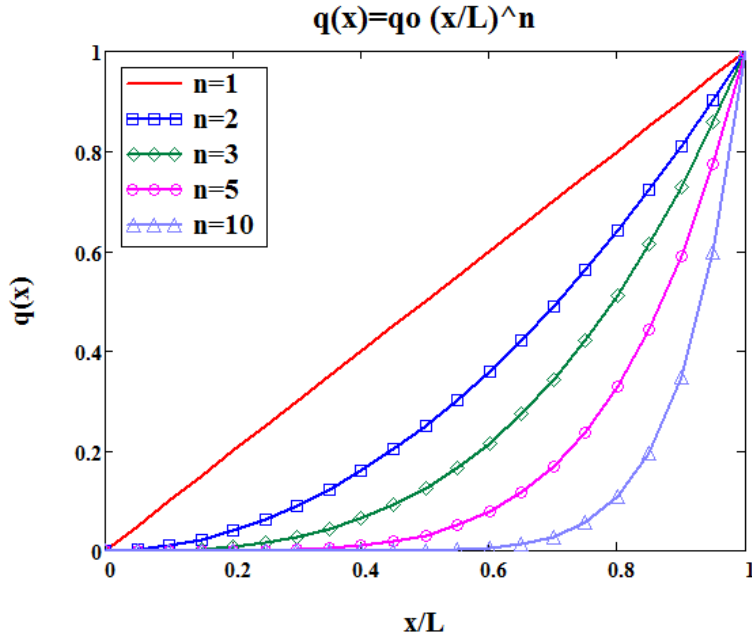


Fig. 7. Generalized power distributed loads

The inhomogeneous solution reads

$$\int_0^x \mathbf{F}(x-\xi)\mathbf{k}(\xi) d\xi = \left\{ \begin{array}{c} \frac{L^{-n}x^{n+4}q_o}{\text{EI}(n+1)(n+2)(n+3)(n+4)} \\ - \frac{L^{-n}x^{n+3}q_o}{\text{EI}(n^3+6n^2+11n+6)} \\ - \frac{L^{-n}x^{n+2}q_o}{n^2+3n+2} \\ - \frac{L^{-n}x^{n+1}q_o}{n+1} \end{array} \right\} \quad (46)$$

### 5.1. S-S Beam under Parabolically Distributed Loads

In this case the state vector is found as

$$\mathbf{S}(x)_{S-S}^E = \mathbf{F}(x)\mathbf{S}(0) + \int_0^x \mathbf{F}(x-\xi)\mathbf{k}(x) d\xi = \left\{ \begin{array}{c} xq_o \left( \begin{array}{c} L^3(n+1)(n+6) \\ +6x^3 \left(\frac{x}{L}\right)^n \\ -L(n+3)(n+4)x^2 \end{array} \right) \\ \frac{6\text{EI}(n+1)(n+2)(n+3)(n+4)}{6\text{EI}(n+1)(n+2)(n+3)(n+4)} \\ q_o \left( \begin{array}{c} -L^3(n+1)(n+6) \\ -6(n+4)x^3 \left(\frac{x}{L}\right)^n \\ +3L(n+3)(n+4)x^2 \end{array} \right) \\ \frac{6\text{EI}(n+1)(n+2)(n+3)(n+4)}{6\text{EI}(n+1)(n+2)(n+3)(n+4)} \\ \frac{xq_o \left( L-x \left(\frac{x}{L}\right)^n \right)}{n^2+3n+2} \\ q_o \left( \frac{L-(n+2)x \left(\frac{x}{L}\right)^n}{(n+1)(n+2)} \right) \end{array} \right\} \quad (47)$$

where the initial rotation and the initial shearing force are found as ( $w_o = 0, M_o = 0$ )

$$\theta_o = -\frac{L^3(n+6)q_o}{6\text{EI}(n+2)(n+3)(n+4)} \quad (48)$$

$$T_o = \frac{Lq_o}{n^2+3n+2}$$

In both theories  $\theta(x), M(x)$  and  $T(x)$  are the same for the beam with simply supported at both ends. In Eq. (47)  $n = 0$  offers a uniformly distributed force (See Eq. 18).

$$w_{(S-S)(n=0)}^E = \frac{x(L^3 - 2Lx^2 + x^3)q_o}{24\text{EI}} = \frac{q_o L^4}{24\text{EI}} \left( \left(\frac{x}{L}\right) - 2\left(\frac{x}{L}\right)^3 + \left(\frac{x}{L}\right)^4 \right)$$

$$\theta_{(S-S)(n=0)}^E = -\frac{(L^3 - 6Lx^2 + 4x^3)q_o}{24\text{EI}} \quad (49)$$

$$M_{(S-S)(n=0)}^E = \frac{1}{2}x(L-x)q_o, \quad T_{(S-S)(n=0)}^E = \frac{1}{2}(L-2x)q_o$$

In the above,  $w_{(S-S)(n=0)}^E$  overlaps with the result in Ref. [9]. In Eq. (47)  $n = 1$  proposes a linearly distributed force (triangular shape).

$$\begin{aligned}
 w_{(S-S)(n=1)}^E &= \frac{x \left( 14L^3 + \frac{6x^4}{L} - 20Lx^2 \right) q_o}{720EI} \\
 \theta_{(S-S)(n=1)}^E &= \frac{\left( -14L^3 - \frac{30x^4}{L} + 60Lx^2 \right) q_o}{720EI} \\
 M_{(S-S)(n=1)}^E &= \frac{1}{6} x \left( L - \frac{x^2}{L} \right) q_o \\
 T_{(S-S)(n=1)}^E &= \frac{1}{6} \left( L - \frac{3x^2}{L} \right) q_o
 \end{aligned} \tag{50}$$

These formulas coincides with the open literature [3].

$$\begin{aligned}
 w(x)_{triangular} &= \frac{q_o L^3 x \left( 7 + 3 \frac{x^4}{L^4} - 10L \frac{x^2}{L^2} \right)}{360EI} \\
 \theta_{o-triangular} &= \frac{7q_o L^3}{360EI}, \theta_{L-triangular} = \frac{8q_o L^3}{360EI} \\
 M(x)_{triangular} &= \frac{q_o L x}{6} \left( 1 - \frac{x^2}{L^2} \right)
 \end{aligned} \tag{51}$$

## 5.2. C-F Beam under Parabolically Distributed Loads

The non-zero elements of the initial state vector are

$$M_o = -\frac{L^2 q_o}{n+2}, \quad T_o = \frac{L q_o}{n+1} \tag{52}$$

Longitudinal variation of the sectional quantities are

$$\mathbf{S}(x)_{C-F}^E = \left\{ \begin{array}{l} x^2 q_o \left( \frac{6L^{-n} x^{n+2}}{(n+1)(n+2)(n+3)(n+4)} + \frac{3L^2}{n+2} - \frac{Lx}{n+1} \right) \\ \frac{6EI}{xL^{-n} q_o \left( (n+3)L^{n+1} \left( \begin{array}{l} (n+2)x \\ -2L(n+1) \end{array} \right) - 2x^{n+2} \right)} \\ \frac{2EI(n+1)(n+2)(n+3)}{L^{-n} q_o \left( L^{n+1} \left( \begin{array}{l} (n+2)x \\ -L(n+1) \end{array} \right) - x^{n+2} \right)} \\ \frac{(n+1)(n+2)}{L q_o - L^{-n} x^{n+1} q_o} \\ n+1 \end{array} \right\} \tag{53}$$

In a cantilever beam  $\theta(x)$ ,  $M(x)$  and  $T(x)$  are the same in both beam theories. A uniformly distributed load is obtained with  $n = 0$  in Eq. (53) (see Eqn. 23).

$$\begin{aligned}
 w_{(C-F)(n=0)}^E &= \frac{x^2(6L^2 - 4Lx + x^2)q_o}{24EI} = \frac{q_o L^4}{24EI} \left( 6 \left( \frac{x}{L} \right)^2 - 4 \left( \frac{x}{L} \right)^3 + \left( \frac{x}{L} \right)^4 \right) \\
 \theta_{(C-F)(n=0)}^E &= -\frac{x(3L^2 - 3Lx + x^2)q_o}{6EI} \\
 M_{(C-F)(n=0)}^E &= -\frac{1}{2}(L-x)^2 q_o \\
 T_{(C-F)(n=0)}^E &= (L-x)q_o
 \end{aligned} \tag{54}$$

In the above, the deflection formula overlaps by Armagan's [10] expression. Sectional quantities in a cantilever beam under linearly distributed forces is obtained with  $n = 1$  in Eq. (53) as follows [3].

$$\begin{aligned}
 w_{(C-F)(n=1)}^E &= \frac{x^2 q_o}{6EI} \left( L^2 + \frac{x^3}{20L} - \frac{Lx}{2} \right) \\
 \theta_{(C-F)(n=1)}^E &= -\frac{x(8L^3 - 6L^2x + x^3)q_o}{24EIL} \\
 M_{(C-F)(n=1)}^E &= -\frac{(L-x)^2(2L+x)q_o}{6L} \\
 T_{(C-F)(n=1)}^E &= \frac{(L-x)(L+x)q_o}{2L}
 \end{aligned} \tag{55}$$

Peddieson et al. [10] presented the following

$$w_{(C-F)-Peddieson \ et \ al.[10]}^E = \frac{L^4 q_o \left( \left( \frac{x}{L} \right)^{4+n} + \frac{(n+1)(n+3)(n+4)}{2} \left( \frac{x}{L} \right)^2 - \frac{(n+2)(n+3)(n+4)}{6} \left( \frac{x}{L} \right) \right)}{EI(n+1)(n+2)(n+3)(n+4)} \tag{56}$$

However, the transverse displacement in Eq. (53) may be rewritten as

$$w_{(C-F)}^E = \frac{L^4 q_o \left( \left( \frac{x}{L} \right)^{4+n} + \frac{(n+1)(n+3)(n+4)}{2} \left( \frac{x}{L} \right)^2 - \frac{(n+2)(n+3)(n+4)}{6} \left( \frac{x}{L} \right) \right)}{EI(n+1)(n+2)(n+3)(n+4)} \tag{57}$$

The author thinks that there must be typographical errors in Peddieson and et al.'s [10] results.

### 5.3. C-S Beam under Parabolically Distributed Loads

The bending moment and the shearing force at the initial section are found as ( $w_o = 0, \theta_o = 0$ )

$$M_o = -\frac{L^2(n+6)q_o}{2(n+2)(n+3)(n+4)} \quad (58)$$

$$T_o = \frac{3L(n+5)q_o}{2(n+1)(n+3)(n+4)}$$

The state vector is to be

$$\mathbf{S}(x)_{C-S}^E = \mathbf{F}(x)\mathbf{S}(0) + \int_0^x \mathbf{F}(x-\xi)\mathbf{k}(x) d\xi = \left\{ \begin{array}{l} \frac{x^2 L^{-n} q_o \left( L^{n+1} \left( \begin{array}{l} L(n+1)(n+6) \\ -(n+2)(n+5)x \\ +4x^{n+2} \end{array} \right) \right)}{4EI(n+1)(n+2)(n+3)(n+4)} \\ \frac{x L^{-n} q_o \left( L^{n+1} \left( \begin{array}{l} 3(n+2)(n+5)x \\ -2L(n+1)(n+6) \\ -4(n+4)x^{n+2} \end{array} \right) \right)}{4EI(n+1)(n+2)(n+3)(n+4)} \\ \frac{L^{-n} q_o \left( L^{n+1} \left( \begin{array}{l} 3(n+2)(n+5)x \\ -L(n+1)(n+6) \\ -2(n+3)(n+4)x^{n+2} \end{array} \right) \right)}{2(n+1)(n+2)(n+3)(n+4)} \\ \frac{q_o \left( \frac{3L(n+5)}{(n+3)(n+4)} - 2L^{-n}x^{n+1} \right)}{2(n+1)} \end{array} \right\} \quad (59)$$

As stated above, a uniformly distributed force is obtained by substituting  $n = 0$  in Eq. (59) (see Eq. 21)

$$w_{(C-S)(n=0)}^E = \frac{x^2(3L-2x)(L-x)q_o}{48EI}$$

$$\theta_{(C-S)(n=0)}^E = -\frac{x(6L^2-15Lx+8x^2)q_o}{48EI} \quad (60)$$

$$M_{(C-S)(n=0)}^E = -\frac{1}{8}(L-4x)(L-x)q_o$$

$$T_{(C-S)(n=0)}^E = \frac{1}{8}(5L-8x)q_o$$

To get a linearly distributed force,  $n = 1$  should be used in Eq. (59).

$$w_{(C-S)(n=1)}^E = \frac{x^2(7L^3-9L^2x+2x^3)q_o}{240EIL}$$

$$\theta_{(C-S)(n=1)}^E = -\frac{x(14L^3-27L^2x+10x^3)q_o}{240EIL} \quad (61)$$

$$M_{(C-S)(n=1)}^E = -\frac{(7L^3-27L^2x+20x^3)q_o}{120L}$$

$$T_{(C-S)(n=1)}^E = \frac{1}{4}\left(\frac{9L}{10} - \frac{2x^2}{L}\right)q_o$$

#### 5.4. C- C Beam under Parabolically Distributed Loads

Initial bending moment and shearing force at the initial section of a C-C Euler-Bernoulli beam are obtained as ( $w_o = 0, \theta_o = 0$ )

$$M_o = -\frac{2L^2q_o}{n^3 + 9n^2 + 26n + 24} \quad (62)$$

$$T_o = \frac{6Lq_o}{n^3 + 8n^2 + 19n + 12}$$

The state vector at any section is

$$\mathbf{S}(x)_{C-C}^E = \mathbf{F}(x)\mathbf{S}(0) + \int_0^x \mathbf{F}(x - \xi)\mathbf{k}(x) d\xi = \begin{pmatrix} \frac{x^2L^{-n}q_o \left( L^{n+1} \begin{pmatrix} L(n+1) \\ -(n+2)x \\ +x^{n+2} \end{pmatrix} \right)}{EI(n+1)(n+2)(n+3)(n+4)} \\ \frac{xL^{-n}q_o \left( L^{n+1} \begin{pmatrix} 3(n+2)x \\ -2L(n+1) \\ -(n+4)x^{n+2} \end{pmatrix} \right)}{EI(n+1)(n+2)(n+3)(n+4)} \\ \frac{L^{-n}q_o \left( -2L^{n+1} \begin{pmatrix} L(n+1) \\ -3(n+2)x \\ -(n+3)(n+4)x^{n+2} \end{pmatrix} \right)}{(n+1)(n+2)(n+3)(n+4)} \\ q_o \left( \frac{6L}{n^3 + 8n^2 + 19n + 12} - \frac{L^{-n}x^{n+1}}{n+1} \right) \end{pmatrix} \quad (63)$$

In the above  $n = 0$  means a uniformly distributed force as follows (see Eq. 25)

$$w_{(C-C)(n=0)}^E = \frac{x^2(L-x)^2q_o}{24EI}$$

$$\theta_{(C-C)(n=0)}^E = -\frac{x(L-2x)(L-x)q_o}{12EI} \quad (64)$$

$$M_{(C-C)(n=0)}^E = -\frac{1}{12}(L^2 - 6Lx + 6x^2)q_o$$

$$T_{(C-C)(n=0)}^E = \frac{1}{2}(L - 2x)q_o$$

For  $n = 1$  the following is achieved

$$w_{(C-C)(n=1)}^E = \frac{x^2(L-x)^2(2L+x)q_o}{120EIL}, \quad \theta_{(C-C)(n=1)}^E = -\frac{x(4L^3 - 9L^2x + 5x^3)q_o}{120EIL} \quad (65)$$

$$M_{(C-C)(n=1)}^E = -\frac{(2L^3 - 9L^2x + 10x^3)q_o}{60L}, \quad T_{(C-C)(n=1)}^E = \left( \frac{3L}{20} - \frac{x^2}{2L} \right) q_o$$

It may be noted that, when  $n = 0$ ,  $\theta(x)$ ,  $M(x)$ , and  $T(x)$  are all the same in both two beam theories. However, they are no longer the same for different values of  $n$ .

## 6. Solutions for Concentrated Force and Moments

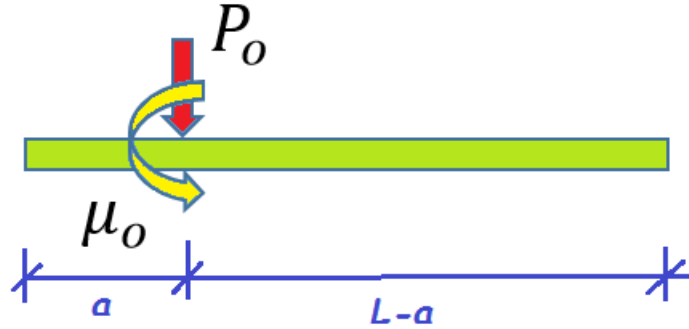


Fig. 8. Concentrated force and couple acting at section  $x = a$

With the help of a discontinuity matrix due to a single couple moment,  $\mu_o$ , and a single force,  $P_o$ , at section  $x = a$  in Eq. (11),  $\mathbf{K}(a) = \{0 \quad 0 \quad -\mu_o \quad -P_o\}^T$ , the following may be obtained for  $a \leq x \leq L$  (Fig. 8)

$$\mathbf{F}(x-a)\mathbf{K}(a) = \begin{Bmatrix} \frac{(a-x)^2((x-a)P_o + 3\mu_o)}{6EI} \\ \frac{(a-x)((x-a)P_o + 2\mu_o)}{2EI} \\ (a-x)P_o - \mu_o \\ -P_o \end{Bmatrix} \quad (66)$$

When only concentrated loads are considered, the general solution is defined in two regions, which are defined as before and after  $x = a$ , as follows (see Eq. 14)

$$\begin{aligned} \mathbf{S}(x)^I &= \mathbf{F}(x)\mathbf{S}(0) \\ \mathbf{S}(x)^{II} &= \mathbf{F}(x)\mathbf{S}(0) + \mathbf{F}(x-a)\mathbf{K}(a) \end{aligned} \quad (67)$$

### 6.1. S-S Beam under Concentrated Force and Moments

In this case the non-zero elements of  $\mathbf{S}(0)$  are

$$\begin{aligned} \theta_o &= \frac{(3a^2 - 6aL + 2L^2)\mu_o - a(a-2L)(a-L)P_o}{6EIL} \\ T_o &= \frac{(L-a)P_o + \mu_o}{L} \end{aligned} \quad (68)$$

The elements of the state vector are

$$\mathbf{S}(x)_{S-S}^I = \mathbf{F}(x)\mathbf{S}(0) = \left\{ \begin{array}{c} \left( \frac{x(a-L)P_o(a^2 - 2aL + x^2)}{-x\mu_o(3a^2 - 6aL + 2L^2 + x^2)} \right) \\ \frac{6EIL}{\left( \frac{\mu_o(3a^2 - 6aL + 2L^2 + 3x^2)}{-(a-L)P_o(a^2 - 2aL + 3x^2)} \right)} \\ \frac{6EIL}{\frac{x((L-a)P_o + \mu_o)}{L}} \\ \frac{(L-a)P_o + \mu_o}{L} \end{array} \right\} \quad (69)$$

$$\mathbf{S}(x)_{S-S}^{II} = \mathbf{F}(x)\mathbf{S}(0) + \mathbf{F}(x-a)\mathbf{K}(a) = \left\{ \begin{array}{c} \left( \frac{(L-x)\left( \frac{\mu_o(3a^2 + x(x-2L))}{-aP_o(a^2 + x(x-2L))} \right)}{6EIL} \right) \\ \frac{6EIL}{\left( \frac{\mu_o(3a^2 + 2L^2 - 6Lx + 3x^2)}{-aP_o(a^2 + 2L^2 - 6Lx + 3x^2)} \right)} \\ \frac{6EIL}{\frac{(L-x)(aP_o - \mu_o)}{L}} \\ \frac{\mu_o - aP_o}{L} \end{array} \right\}$$

When the beam is only subjected to a single force at the mid-span ( $\mu_o = 0, a = L/2$ ) then Eq. (69) becomes

$$\mathbf{S}(x)_{S-S}^I = \left\{ \begin{array}{c} \frac{(3L^2x - 4x^3)P_o}{48EI} \\ \frac{(L^2 - 4x^2)P_o}{16EI} \\ \frac{xP_o}{2} \\ \frac{P_o}{2} \end{array} \right\}, \quad \mathbf{S}(x)_{S-S}^{II} = \left\{ \begin{array}{c} -\frac{(L-x)(L^2 - 8Lx + 4x^2)P_o}{48EI} \\ -\frac{(L-2x)(3L-2x)P_o}{16EI} \\ \frac{1}{2}(L-x)P_o \\ -\frac{P_o}{2} \end{array} \right\} \quad (70)$$

The dimensionless displacement may be defined as  $\bar{w} = EIw/(P_oL^3)$  for a point force. From Eq. (70) with  $x = L/2$  it is found as  $\bar{w}_{max} = 1/48 = 0.020833$ . Aydođdu [12] reported it as  $\bar{w}_{max} = 0.022222$ .

## 6.2. C-C Beam under Concentrated Force and Moments

The unknown elements of the initial state vector are

$$M_o = -\frac{(a-L)((L-3a)\mu_o + a(a-L)P_o)}{L^2}, \quad T_o = \frac{(a-L)((a-L)(2a+L)P_o - 6a\mu_o)}{L^3} \quad (71)$$

With the help of the above, the following is written

$$\mathbf{S}(x)_{C-c}^I = \mathbf{F}(x)\mathbf{S}(0) = \left\{ \begin{array}{l} x^2(a-L) \left( \begin{array}{l} 3\mu_o(-3aL+2ax+L^2) \\ +(a-L)P_o \left( \begin{array}{l} 3aL \\ -x(2a+L) \end{array} \right) \end{array} \right) \\ \hline 6EIL^3 \\ x(a-L) \left( \begin{array}{l} 2\mu_o(3a(x-L)+L^2) \\ +(a-L)P_o \left( \begin{array}{l} 2aL \\ -x(2a+L) \end{array} \right) \end{array} \right) \\ \hline 2EIL^3 \\ (a-L) \left( \begin{array}{l} \mu_o(-3aL+6ax+L^2) \\ +(a-L)P_o \left( \begin{array}{l} aL \\ -x(2a+L) \end{array} \right) \end{array} \right) \\ \hline L^3 \\ \frac{(a-L)((a-L)(2a+L)P_o - 6a\mu_o)}{L^3} \end{array} \right\} \quad (72)$$

$$\mathbf{S}(x)_{C-c}^{II} = \mathbf{F}(x)\mathbf{S}(0) + \mathbf{F}(x-a)\mathbf{K}(a) = \left\{ \begin{array}{l} a(L-x)^2 \left( \begin{array}{l} 3\mu_o(a(L+2x)-2Lx) \\ -aP_o(a(L+2x)-3Lx) \end{array} \right) \\ \hline 6EIL^3 \\ a(L-x) \left( \begin{array}{l} aP_o(2ax+L^2-3Lx) \\ -2\mu_o(3ax+L^2-3Lx) \end{array} \right) \\ \hline 2EIL^3 \\ a \left( \begin{array}{l} aP_o(-aL+2ax+2L^2-3Lx) \\ +\mu_o(3a(L-2x)-4L^2+6Lx) \end{array} \right) \\ \hline L^3 \\ \frac{a(6(L-a)\mu_o + a(2a-3L)P_o)}{L^3} \end{array} \right\}$$

When C-C Euler beam is only subjected to a single force at the mid-span ( $\mu_o = 0, a = L/2$ ) then Eq. (72) becomes

$$\mathbf{S}(x)_{C-c}^I = \left\{ \begin{array}{l} \frac{x^2(3L-4x)P_o}{48EI} \\ \frac{x(L-2x)P_o}{8EI} \\ -\frac{1}{8}(L-4x)P_o \\ \frac{P_o}{2} \end{array} \right\}, \quad \mathbf{S}(x)_{C-c}^{II} = \left\{ \begin{array}{l} -\frac{(L-4x)(L-x)^2P_o}{48EI} \\ \frac{(L-2x)(L-x)P_o}{8EI} \\ \frac{1}{8}(3L-4x)P_o \\ -\frac{P_o}{2} \end{array} \right\} \quad (73)$$

### 6.3. C-F Beam under Concentrated Force and Moments

For a C-F Euler-Bernoulli beam under concentrated force and moments, the initial state vector is determined as

$$\mathbf{S}(0) = \{0 \quad 0 \quad (\mu_o - aP_o) \quad P_o\}^T \quad (74)$$

Variation of the sectional quantities along the beam is

$$\mathbf{S}(x)_{C-F}^I = \mathbf{F}(x)\mathbf{S}(0) = \begin{Bmatrix} -\frac{x^2((x-3a)P_o + 3\mu_o)}{6EI} \\ \frac{x((x-2a)P_o + 2\mu_o)}{2EI} \\ (x-a)P_o + \mu_o \\ P_o \end{Bmatrix} \quad (75)$$

$$\mathbf{S}(x)_{C-F}^{II} = \mathbf{F}(x)\mathbf{S}(0) + \mathbf{F}(x-a)\mathbf{K}(a) = \begin{Bmatrix} \left( \frac{3a(a-2L)\mu_o}{-(a^3 - 3a^2L + 3aL^2 - 3L^3)P_o} \right) \\ \frac{2a\mu_o - (a^2 - 2aL + 2L^2)P_o}{6EI} \\ \frac{2EI}{(a-L)P_o} \\ 0 \end{Bmatrix}$$

If only a single force acts on a C-F Euler-Bernoulli beam at section  $x = L$ , solutions in two regions become ( $\mu_o = 0$  and  $a = L$ )

$$\mathbf{S}(x)_{C-F}^I = \begin{Bmatrix} \frac{x^2(3L-x)P_o}{6EI} \\ \frac{x(x-2L)P_o}{2EI} \\ (x-L)P_o \\ P_o \end{Bmatrix} \quad (76)$$

$$\mathbf{S}(x)_{C-F}^{II} = \begin{Bmatrix} \frac{L^3P_o}{3EI} \\ -\frac{L^2P_o}{2EI} \\ 0 \\ 0 \end{Bmatrix}$$

#### 6.4. C-S Beam under Concentrated Force and Moments

Unknown elements of the initial state vector are

$$M_o = \frac{(3a^2 - 6aL + 2L^2)\mu_o - a(a-2L)(a-L)P_o}{2L^2} \quad (77)$$

$$T_o = \frac{(a^3 - 3a^2L + 2L^3)P_o - 3a(a-2L)\mu_o}{2L^3}$$

For this boundary condition, the whole elements of the state vector at any section are defined by

$$\mathbf{S}(x)_{C-S}^I = \mathbf{F}(x)\mathbf{S}(0) = \left\{ \begin{array}{l} x^2 \left( \begin{array}{l} 3\mu_o \left( \begin{array}{l} a^2(x-3L) \\ +2aL(3L-x) - 2L^3 \end{array} \right) \\ +(a-L)P_o \left( \begin{array}{l} a^2(3L-x) \\ +2aL(x-3L) + 2L^2x \end{array} \right) \end{array} \right) \\ \hline \begin{array}{l} 12EIL^3 \\ \left( \begin{array}{l} x\mu_o \left( \begin{array}{l} a^2(6L-3x) \\ +6aL(x-2L) + 4L^3 \end{array} \right) \\ +x(a-L)P_o \left( \begin{array}{l} x(a^2-2aL-2L^2) \\ -2aL(a-2L) \end{array} \right) \end{array} \right) \\ \hline 4EIL^3 \\ \left( \begin{array}{l} \mu_o \left( \begin{array}{l} 3a^2(L-x) \\ +6aL(x-L) + 2L^3 \end{array} \right) \\ -(a-L)P_o \left( \begin{array}{l} a^2(L-x) \\ +2aL(x-L) + 2L^2x \end{array} \right) \end{array} \right) \\ \hline 2L^3 \\ \left( \begin{array}{l} (a^3-3a^2L+2L^3)P_o \\ -3a(a-2L)\mu_o \end{array} \right) \\ \hline 2L^3 \end{array} \right\} \quad (78)$$

$$\mathbf{S}(x)_{C-S}^{II} = \mathbf{F}(x)\mathbf{S}(0) + \mathbf{F}(x-a)\mathbf{K}(a) = \left\{ \begin{array}{l} a(L-x) \left( \begin{array}{l} aP_o \left( \begin{array}{l} -2aL^2 + x^2(a-3L) \\ -2Lx(a-3L) \end{array} \right) \\ +3\mu_o \left( \begin{array}{l} a(2L^2+2Lx-x^2) \\ +2Lx(x-2L) \end{array} \right) \end{array} \right) \\ \hline \begin{array}{l} 12EIL^3 \\ a \left( \begin{array}{l} aP_o \left( \begin{array}{l} -Lx(2a+3x) \\ +ax^2-2L^3+6L^2x \end{array} \right) \\ +\mu_o \left( \begin{array}{l} 6Lx(a+x)-3ax^2 \\ +4L^3-12L^2x \end{array} \right) \end{array} \right) \\ \hline 4EIL^3 \\ a(L-x)(3(a-2L)\mu_o - a(a-3L)P_o) \\ \hline 2L^3 \\ a(a(a-3L)P_o - 3(a-2L)\mu_o) \\ \hline 2L^3 \end{array} \right\}$$

If  $\mu_o = 0$  and  $a = L/2$ , Eq. (77) turns to be

$$\mathbf{S}(x)_{C-S}^I = \left\{ \begin{array}{l} \frac{x^2(9L-11x)P_o}{96EI} \\ \frac{x(11x-6L)P_o}{32EI} \\ \frac{1}{16}(11x-3L)P_o \\ \frac{11P_o}{16} \end{array} \right\}, \quad \mathbf{S}(x)_{C-S}^{II} = \left\{ \begin{array}{l} -\frac{(L-x)(2L^2-10Lx+5x^2)P_o}{96EI} \\ -\frac{(4L^2-10Lx+5x^2)P_o}{32EI} \\ \frac{5}{16}(L-x)P_o \\ -\frac{5P_o}{16} \end{array} \right\} \quad (79)$$

## 7. Conclusions

In the present study some remarkable formulas are proposed for the bending behavior of classically supported Euler-Bernoulli beams under both distributed and concentrated loads via the transfer matrix approach. For classical boundary conditions it is observed that, Euler-Bernoulli beam solutions are independent from  $L/h$  ratios. This is an expected conclusion. The present formulas which also comprise the point and distributed couple moments may be very useful to the readers. It is worth noting that sectional quantities at positive sections may be obtained by using those formulas. Since the present analysis is a linear elastic, the superposition principle is hold under combined loads.

## References

- [1] Young, W.C., Budynas, R.G., Roark's Formulas for Stress and Strain, Seventh Edition, McGraw-Hill, New York, ISBN 0-07-072542-X, 2002.
- [2] Köktürk, U., Makina Mühendisinin El Kitabı Cilt 1, Nobel Akademik Yayıncılık, ISBN 975927101X, 2005. (in Turkish)
- [3] Miller ve Kirişler, (08.06.2018), [http://www.guven-kutay.ch/ozet-konular/06a\\_miller\\_kirisler.pdf](http://www.guven-kutay.ch/ozet-konular/06a_miller_kirisler.pdf), 2018. (in Turkish)
- [4] İnan M., The Method of Initial Values and the Carry-Over Matrix in Elastomechanics, ODTÜ Publication, Ankara, No: 20, 1968.
- [5] Arici, M., Granata, M.F., Analysis of curved incrementally launched box concrete bridges using the Transfer Matrix Method, *Bridge Structures*, 3(3-4),165-181, 2007.
- [6] Arici, M., Granata, M.F., Generalized curved beam on elastic foundation solved by Transfer Matrix Method, *Structural Engineering & Mechanics*, 40(2), 279-295, 2011.
- [7] Reddy, J.N., Pang, S.D., Nonlocal continuum theories of beams for the analysis of carbon nanotubes, *J. Appl. Phys.* 103, 023511, 2008.
- [8] Civalek, Ö., Demir, Ç., Bending analysis of microtubules using nonlocal Euler–Bernoulli beam theory, *Applied Mathematical Modelling*, 35, 2053–2067, 2011.
- [9] Tuna, M., Kirca, M., Exact solution of Eringen's nonlocal integral model for bending of Euler–Bernoulli and Timoshenko beams, *Int J Eng Sci*, 105, 80–92, 2016.
- [10] Peddieson, J., Buchanan, G.R., McNitt, R.P., Application of nonlocal continuum models to nanotechnology, *Int. J. Eng. Sci.*, 41, 305–312, 2003.
- [11] Karamanli, A., Elastostatic deformation analysis of thick isotropic beams by using different beam theories and a meshless method, *International Journal of Engineering Technologies*, 2(3), 83-93, 2016.
- [12] Aydoğdu, M., A general nonlocal beam theory: Its application to nanobeam bending, buckling and vibration, *Physica E*, 41, 1651–1655, 2009.

## Numerical Modelling of Wheel on the Snow

Mesut Tigdemir <sup>a</sup>, Mahyar Jafarzadyeganeh <sup>b</sup>, Mehmet Çağrı Bayrak <sup>c</sup>, Mehmet Avcar <sup>d\*</sup>

<sup>a, c, d</sup> Department of Civil Engineering, Faculty of Engineering, Suleyman Demirel University, Cunur, Isparta, Turkey

<sup>b</sup> Graduate School of Natural and Applied Sciences, Suleyman Demirel University, Cunur, Isparta, Turkey  
E-mail address: [mtigdemir.acd@yahoo.com](mailto:mtigdemir.acd@yahoo.com) <sup>a</sup>, [mahyar.yeganeh1993@gmail.com](mailto:mahyar.yeganeh1993@gmail.com) <sup>b</sup>, [mcbayrak@yahoo.com](mailto:mcbayrak@yahoo.com) <sup>c</sup>, [mehmetavcar@yahoo.com](mailto:mehmetavcar@yahoo.com) <sup>d\*</sup>

ORCID numbers of authors:

0000-0002-5303-2722 <sup>a</sup>, 0000-0002-2973-2198 <sup>b</sup>, 0000-0002-9995-7325 <sup>c</sup>, 0000-0002-0689-0601 <sup>d</sup>

Received date: 27.06.2018

Accepted date: 26.07.2018

### Abstract

*In the present study, a numerical model is developed for wheel-snow interaction using finite element method based software. For this aim, the model of tire is designed using SolidWorks and ANSYS Design modeler. The analyses of the prepared models are performed using ANSYS Explicit Dynamics considering Mooney-Rivlin tire model. Frictional relationship between wheel and snow ground is established considering snow erosion as linear, in the analyses. Six different mesh sizes are considered, the effect of mesh size and number on the accuracy of the obtained results and solution time is discussed. Finally, it is concluded that models with 0.025 m and 0.02 m mesh sizes give more accurate results than the others and a strong linear proportion exists between the number of iteration and the mesh size.*

**Keywords:** Finite Element Method; Modelling; Snow; Wheel; Mesh size.

### 1. Introduction

The basic function of the wheel is to ensure contact between the vehicle and the surface of coating. This contact is provided by vulcanized rubber which is covering of the tread. The contact area between tire tread and ground is an average 150cm<sup>2</sup>. The contact between wheel and road surface provides the vehicle driving comfort and road holding. Friction force between wheel and snow, vertical force of vehicle, directional and angular velocity are the important parameters that effect the performance of the vehicle. At the same time, it has been observed that the internal pressure of the wheel is effective in handling, also [1].

The numerical analysis of wheel using finite element method is usually performed with three different methods, the first one is analyzing the contact area; the second one is designing and analyzing the two-dimensional model, and the last one is analyzing the discretized three-dimensional model. From the results of experimental analyses, it has been found that the third method proves more accurate results than the other methods [2-7].



According to previous studies, for isotropic systems the node-centered and triangular mesh cell-centered approaches presented more accurate results than the other ones. At the same time for quadrilateral mesh cell-centered approach is also accurate. Moreover, it should be noted that minimum required element number in the forward plastic zone must be equal to sum of the number of elements in plastic zone and loading cycles planned to be applied in the [8-10].

In recent days, experimental analyses are more costly than numerical ones such as finite element analysis, however, in case of unconscious use finite element method may cause loss of time. In order to get similar results, it is necessary to select the correct system. Hence, discretization known as a part of the system and plays an important role in gaining time [11-13].

The purpose of this study is to determine the value of the tire and its sinking on the snow, shear stress, strain and stresses occurred on the snow, which is designed by ANSYS software [14] based on finite element method. The model of tire is designed by SolidWorks, then in ANSYS Design modeler, snow material on the surface contacts, dimensions are prepared in  $1.8 \times 1.4 \times 0.2$  m. The analysis of the prepared models are done by ANSYS Explicit Dynamics. It's designed for the 195/60 R15 wheel with size specifications to observe its effects on the snow, in the model, internal pressure of wheel is defined 200 kPa. In the ANSYS program, for the wheel model used, Mooney- Rivlin tire model is utilized. In the structure of radial tires, ropes are placed in the wheel's pattern vertical and steel wires are on the heel connection. At the same time, the used wires in body and heel parts are placed parallel in pattern of wheel. Frictional relationship between wheel and snow ground is established. And friction coefficient of ANSYS program is assumed to be 0.3. Snow erosion is considered linear. A vertical force of 4.5 kN was applied to the wheel. To increase the quality of the element of the snow surface, element size is defined as 0.02 m. The wheels both perform rotating and displacement movement, angular and shift speed, for the forward movement of the wheels from rim center, it's placed in the center of wheel. In this case limit time 0.2 second is given for the solution.

## 2. Modeling of Tire on Snow

ANSYS-Explicit dynamics software is used to analyze the model where the modeling of wheels and snow materials is described as well as the 195/60R15 wheel is designed in Solidworks software. This model is defined in Step format in ANSYS Design modeler. Fig. 1. shows, snow material designed in Design modeler with 1.8m length, 1.4m width and 0.2m height as tangent to the wheel tread. Mesh dimensions were selected as 0.015m, 0.02m, 0.025m, 0.03m, 0.035m and 0.04 m.

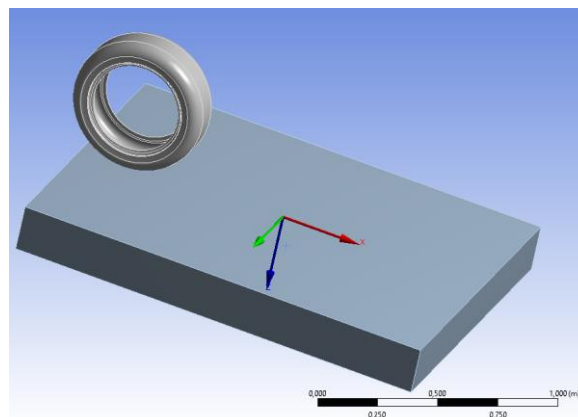


Fig. 1. Solid Works model of wheel and snow

The inner liner, tread and sidewall of the wheel are described as Mooney-Rivlin hyper-elastic material, hence two parameter Mooney-Rivlin strain energy potential is defined as follow:

$$W = C_{10}(I_1 - 3) + C_{01}(I_2 - 3) + \frac{1}{d}(J - 1)^2 \quad (1)$$

where,  $W$ ,  $I_1$ ,  $I_2$ ,  $C_{10}$ ,  $C_{01}$  and  $d$  are strain energy potential, first deviatoric strain invariant, second deviatoric strain invariant, material constants characterizing the deviatoric deformation of the material and material incompressibility parameter, respectively.

Besides, the initial shear modulus is defined as:

$$\mu = 2(C_{10} - C_{01}) \quad (2)$$

The material properties are available in ANSYS material library [14], as  $C_{10}=150$  kPa;  $C_{01}= 15$  kPa,  $\rho=1000$  kg/m<sup>3</sup>.

In the structure of radial tires body ply is perpendicular to tread pattern. The body ply model is presented in Fig. 2. Here, the following material properties were considered:  $E_{ply}=9.87$  GPa;  $\nu_{ply}=0.3$ ;  $\rho_{ply}=1500$  kg/m<sup>3</sup>.

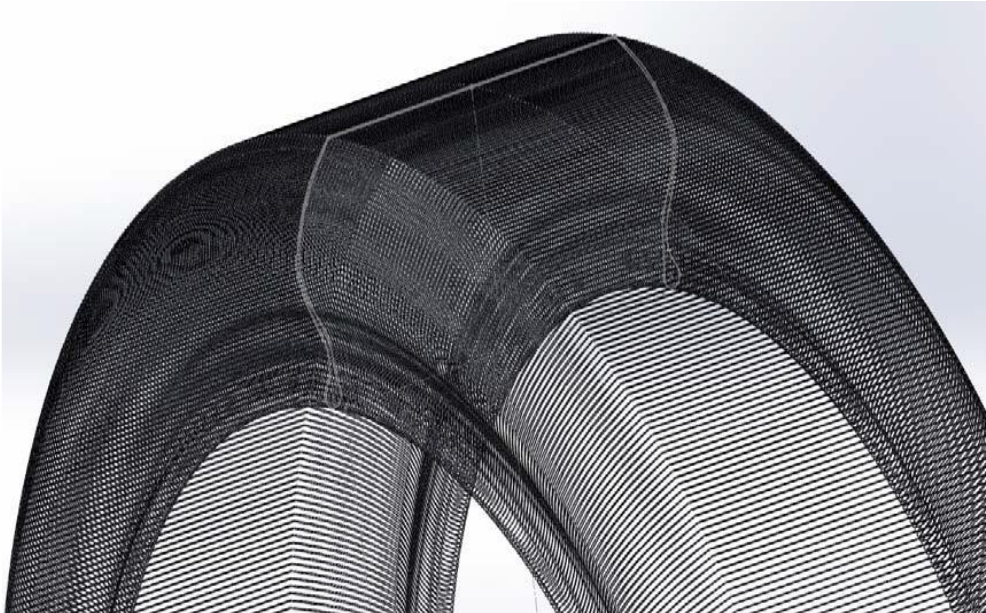


Fig. 2. The Model of Body Ply

The belts are placed parallel to tread pattern and the model is illustrated in Fig. 3. Here, the following material properties were considered:  $E_{belt}=172.2$ GPa;  $\nu_{belt}=0.3$ ;  $\rho_{belt} =5900$  kg/m<sup>3</sup>.



Fig. 3. The Model of Belts

Snow can be regarded as the cellular form in which ice crystals stick together. Here the low-density snow material is defined as Drucker-Prager model and the considered material properties are  $E_{D-P}=13.79$  MPa;  $\nu_{D-P}=0.3$ ;  $\rho_{D-P}=200$  kg/m<sup>3</sup>,  $\delta_{D-P}=5$  kPa  $\phi_{D-P}=22.538^\circ$ , where  $\delta$  and  $\phi$  represents Drucker-Prager cohesion and Drucker-Prager friction angle, respectively.

The average load for each wheel of vehicles is 4.5 kN. Directional and angular velocities are selected as 0.5 m/s and 1 rad/s, respectively, an internal pressure of 200 kPa is defined to the wheels and the coefficient of friction of snow is defined as 0.3.

### 3. Illustrative Examples

In this section, six numerical analyses are performed to examine the given problem. Analyses were performed ANSYS Explicit dynamics. Here, the wheel moved 0.2 seconds after it is left on the snow. During this time the wheel has traveled 10 cm. The type of mesh is automatically selected, and the mesh sizes are defined as described in the modeling section.

#### Example 1:

In the first example, sinking on the snow for different mesh sizes is examined and results are presented in Fig. 4. It is found that except the mesh size of 0.015 m, all models have shown almost similar results. By considering the other mesh sizes in the last part, tire sinkage is between 12 and 14 cm on snow. By observing the size as if mesh 0.02 and 0.25 m, nearly the same results happened. At the same time, the values in the models of 0.035 and 0.04 m in mesh size which are close to each other are exhibited while. The 0.035 m mesh size model exhibited values close to 0.030, while the values in the beginning are similar to the 0.04 m mesh size model. However, considering the previous studies, the 0.025 and 0.02 m mesh size models show more accurate results than the other models.

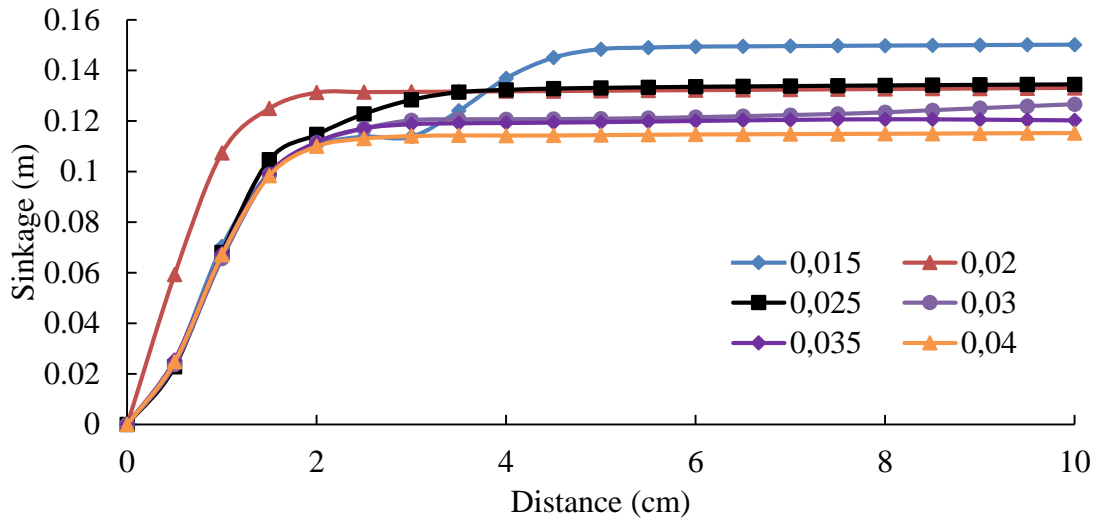


Fig. 4. The variation of tire sinkage on snow for different mesh sizes

**Example 2:**

In the second example, the values of shear stress formed on the snow for different mesh sizes are investigated and results were plotted in Fig. 5. Similar to the sinking results on snow, 0.015 m mesh size model showed different results than the others. Here, 0.02 and 0.025 m mesh size models values are similar. In the beginning (up to 3 cm travel), the 0.03 m mesh size model exhibited values close to the 0.04 m mesh size results; however, between 3 and 7 cm of progress the 0.03 m mesh size model showed close values to the 0.02 and 0.025 mesh size models, in the last part (7-10 cm travel), 0.03m mesh size model’s shear stress values are between 0.035 and 0.04 m mesh size models. The 0.035 and 0.04 m mesh size models exhibited different results in the first 2 cm of progress, but showed close results in the last 5-10 cm progress. Consequently, considering the previous studies, the 0.02 and 0.025 m mesh size models showed more accurate results than the other models.

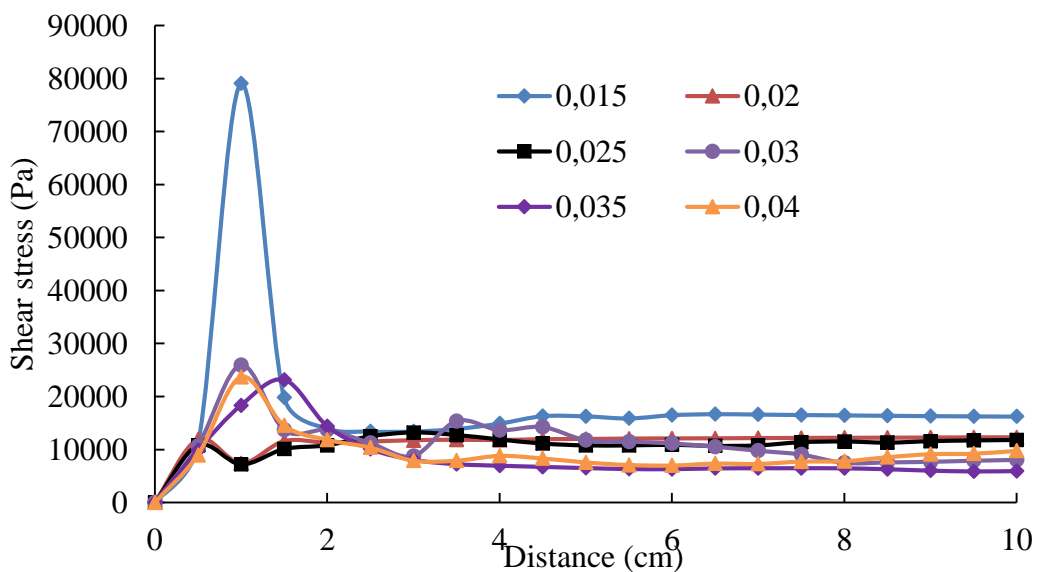


Fig. 5. The variation of shear stress for different mesh sizes

### Example 3:

In the third example, the values of normal stress formed on the snow for different mesh sizes are studied and results are given in Fig. 6. In all models except for the 0.015 m mesh size model, first linear increase is observed, then, followed by unregulated change and finally linear decrease observed. 0.020 and 0.025 m mesh size models exhibited nearly equal results to each other. However, the 0.030, 0.035, and 0.040 m mesh size models showed different values in the first 5 cm travel, they showed values close to the 0.02 and 0.025 m mesh size models at the end point.

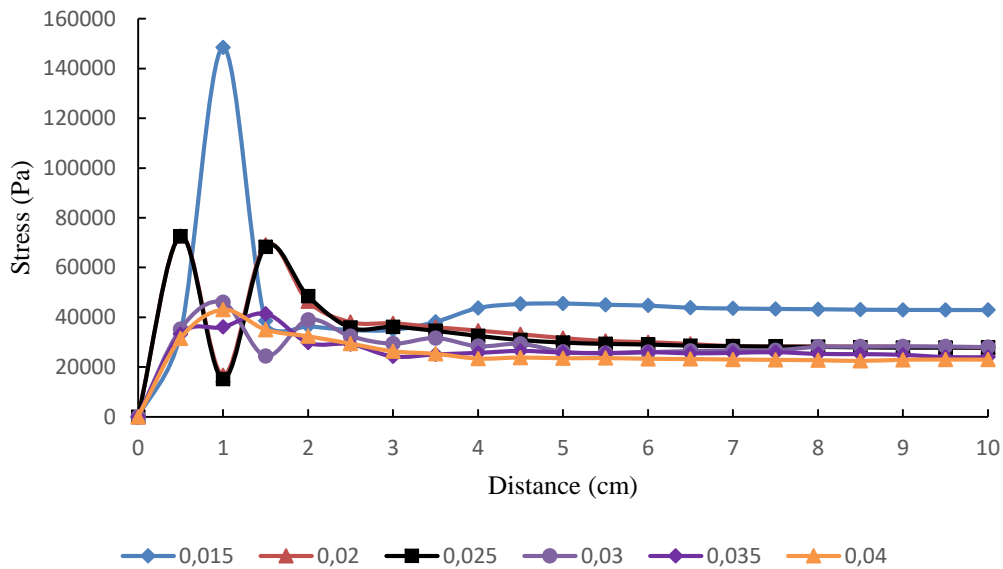


Fig. 6. The variation of normal stress for different mesh sizes

### Example 4:

In the fourth example, the values of strain formed on the snow for different mesh sizes are investigated and results were plotted in Fig. 7. First, when the 0.015 m mesh size model is examined, two intense changes are observed in the snow deformation curve of this model and it is found that it has higher value than the other models. As it can be seen in this graph, 0.02 and 0.025 m mesh size models displayed close behavior in the last 6 cm progress, but the 0.02 m mesh size model at the first 4 cm showed a strong increase compared to the 0.025 model. When the other models were compared, it is observed that, although they showed similar results at the first 0.5 cm progression, they had different values in the following sections.

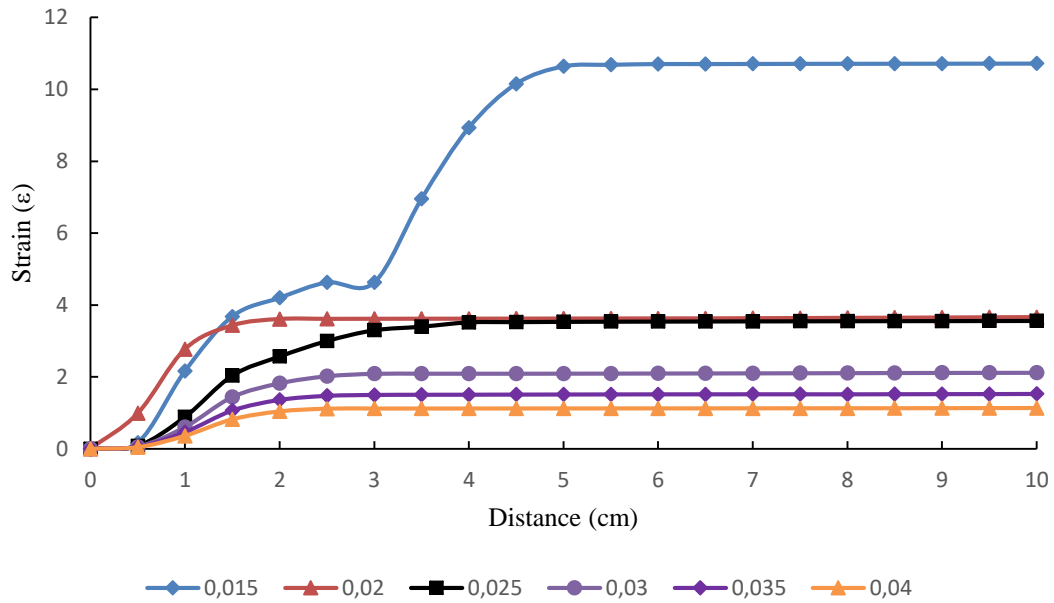


Fig. 5. The variation of strain for different mesh sizes

**Example 5:**

In the fifth example, the relation between mesh size and solution time is studied and results are presented in Fig. 8. It is found that, there is a strong linear relationship between exponential of the mesh size and the solution time, i.e., the solution time increases as the mesh size gets exponentially smaller.

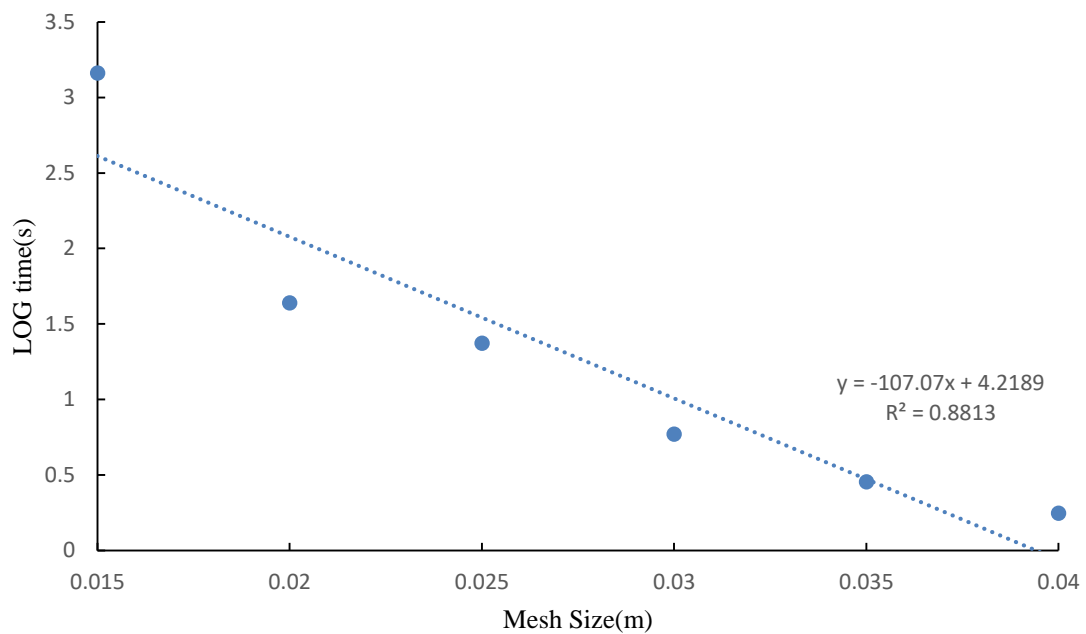


Fig. 6. The variation of time logarithm versus mesh size

### Example 6:

In the last example, the relationship between mesh size and number of iteration was discussed and results are plotted in Fig. 9. It is concluded that, there is a strong linear proportion between the number of solution iteration and the exponential mesh size i.e., the mesh size exponentially increases as the number of cycles decreases.

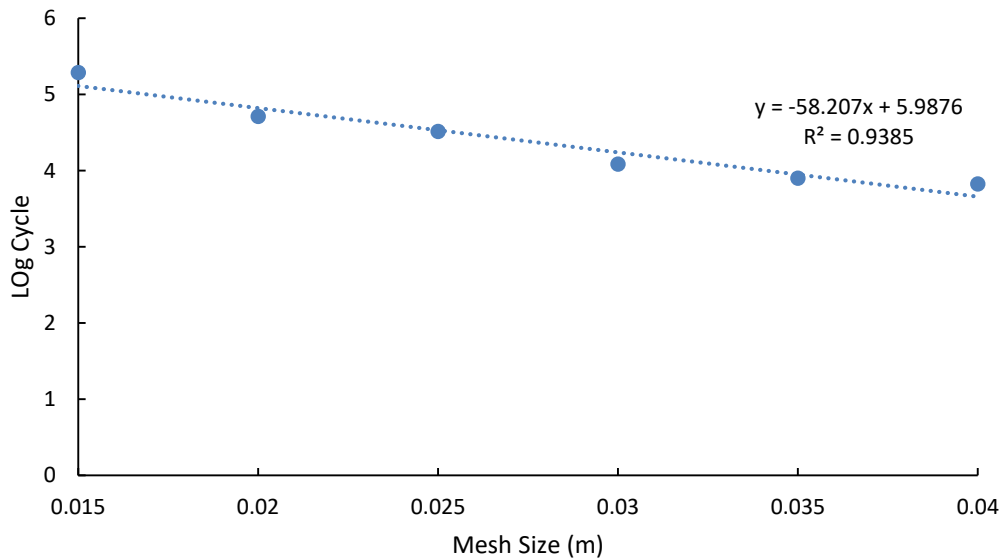


Fig. 9. The variation of number of iteration versus mesh size

## 4. Conclusion

In the present study, a numerical model is developed for wheel-snow interaction using finite element method based software. For this aim, the model of tire is designed using SolidWorks and ANSYS Design modeler. The analyses of the prepared models are performed using ANSYS Explicit Dynamics considering Mooney- Rivlin tire model. Frictional relationship between wheel and snow ground is established considering snow erosion as linear, in the analyses. Six different mesh sizes are considered, the effect of mesh size and number on the accuracy of the obtained results and solution time is discussed. Briefly, it was found that for sinking, shear stress, normal stress and strain of the snow 0.025 and 0.02 m mesh size models show more accurate results than the other models as well as there is a strong linear proportion between the number of solution iteration and the mesh size i.e., the mesh increases as the number of cycles decreases.

## References

- [1] Jafarzadyeganeh, M., Modeling and developing a new generation tire chain with finite element analysis (FEA), Institute Of Natural And Applied Sciences, MSc.Thesis, Isparta, 2017.
- [2] Danielson, K.T., Noor, A.K., Green, J.S., Computational strategies for tire modeling and analysis, Computers & Structures, 4, 673-693, 1996.

- [3] Mousseau, C.W., Hulbert, G.M., An efficient tire model for analysis of spindle forces produced by a tire impacting large obstacles, *Computer Methods in Applied Mechanics and Engineering*, 135, 15-34, 1996.
- [4] Xiangquiao Y., Non-linear three-dimensional finite element modeling of radial tires, *Mathematics and computers in simulation*, 58, 51–70, 2001.
- [5] Lee, J.H. Finite element modeling of interfacial forces and contact stresses of pneumatic tire on fresh snow for combined longitudinal and lateral slips, Elsevier, *Journal of Terramechanics*, 48, 171-197, 2011.
- [6] Cho, J.R., Numerical estimation of rolling resistance and temperature distribution of 3-D periodic patterned tire, *International Journal of Solids and Structures*, 50, 86-96, 2013.
- [7] Wei, C., Olatunbosun, O.A., Transient dynamic behaviour of finite element tire traversing obstacles with different heights, *Journal of Terramechanics*, 1-16, 2014.
- [8] Katz, A., Sankaran, V., Mesh quality effects on the accuracy of cfd solutions on unstructured meshes, 49th AIAA Aerospace Sciences Meeting including the New Horizons Forum and Aerospace Exposition, *Aerospace Sciences Meetings*, 4 - 7 January 2011,
- [9] Hou, C.Y., Development of a varying mesh scheme for finite element crack closure analysis, *Engineering Fracture Mechanics*, 148, 42-59, 2015.
- [10] Tigdemir M., Jafarzadyeganeh M., Avcar M., Finite element modelling of wheel on the snow. 4th international conference on computational and experimental science and engineering, 1, 452, 2017.
- [11] Yan, X., Non-linear three-dimensional finite element modeling of radial tires, *Mathematics and Computers in Simulation*, 58(1), 51–70, 2001.
- [12] Borstad, C.P., McClung, D.M., Numerical modeling of tensile fracture initiation and propagation in snow slabs using nonlocal damage mechanics, *Cold Regions Science and Technology*, 69(2-3), 145-155, 2011
- [13] Krmela, J., Krmelová, Replacement of Belt Structure for FEA of Tire, *Procedia Engineering*, 132-136, 2016.
- [14] ANSYS, 2016. Academic Student Engineering Simulation Software.

## Closed-Form Formulas for Hyperbolically Tapered Rotating Disks Made of Traditional Materials under Combined Thermal and Mechanical Loads

Vebil Yıldırım

Department of Mechanical Engineering, Faculty of Engineering, University of Çukurova, Adana, Turkey  
E-mail address: [vebil@cu.edu.tr](mailto:vebil@cu.edu.tr)

ORCID numbers of authors:  
0000-0001-9955-8423

Received date: 12.07.2018

Accepted date: 24.07.2018

### Abstract

Using the true temperature distribution along the radial coordinate, closed-form formulas are offered for readers to study the thermo-mechanical behavior of variable thickness disks having both convergent and divergent hyperbolic thickness profiles made of conventional materials. Internal and external pressures, centrifugal forces and thermal loads due to the differences in prescribed surface temperatures are all considered with three boundary conditions: free-free (a circular annulus), fixed-free (a disk mounted on a rotating shaft at the inner surface), and fixed-fixed (a disk mounted on a rotating shaft at the inner surface and cased at the outer surface) boundary conditions. A parametric study is also conducted in almost real working environment in which the outer surface of the disk has considerably higher temperature rather than the inner surface. The thermomechanical linear elastic response of a hyperbolic mounted rotating disk subjected to the external pressure induced by blades is originally handled by those proposed formulas.

**Keywords:** Variable thickness disk, nonuniform rotating disk, closed-form elasticity solution, exact solution, analytical solution, thermomechanical, thermal analysis.

### 1. Introduction

As a rotating machinery element, rotating disks may operate as a circular annulus or as a disk attaching a rotating shaft at its center. A rigid casing may exist at the outer surface of such a disk. Their thickness may vary along the radial direction linearly, hyperbolically, parabolically, exponentially or so on and so forth. It may be made of any kind of traditional or advanced materials. Rotating disks may act in high temperature environments like turbine rotors, flywheels and gears and may be subjected to simultaneously external pressures due to the existence of the blades. In such cases, the thermo-mechanical analyses come into prominence in the design of such structures. It is obvious that the existence of closed-form formulas that can be directly used in the design stage in relation to the subject matter is to be of great convenience for engineers.

Thermal-related analyses of uniform disks made of an isotropic and homogeneous materials have paid much attention than disks having varying section properties and made of advanced



composite materials [1-10]. From those, Güven and Altay [1] investigated the elastic–plastic stress distribution of a solid disk due to nonuniform heat source under external pressure. Kulkarni and Deshmukh [4] addressed the thermal stresses in a thick annular disk under steady temperature field. Nejad and Afshin [6] offered an analytical solution of transient thermoelastic behaviors of rotating pressurized disks subjected to arbitrary boundary and initial conditions. Kaur et al. [8] observed that thermal effect in the disk increase the value of circumferential stress at the internal surface and radial stresses at the external surface for compressible as compare to incompressible material. Based on a variational principle considering the radial displacement field as unknown, Nayak and Saha [9] evaluated the influence of thermo-mechanical loading on stresses and deformation states in a rotating disk with varying thicknesses. They considered different disk geometries as well as temperature distribution profiles to calculate the limit angular speed of the disks under thermo-mechanical loading. Yıldırım [10] offered a consistent and an all-in-one analytical study for the determination of heat-induced, pressure-induced, and centrifugal force-induced axisymmetric exact deformation and stresses in a thick-walled spherical vessel, a cylindrical vessel, and a uniform disk at specified constant surface temperatures and at a constant angular velocity. Yıldırım [10] included both the inner and outer pressures in the formulation of annular structures made of an isotropic and homogeneous linear elastic material. For disks, three different boundary conditions were taken into account to consider mechanical engineering applications in the study [10].

Thermal-related analyses of uniform disks made of anisotropic materials [11-19] and functionally graded materials [20-28] are other investigation themes. Unfortunately, the number of studies on the thermal/thermal related analysis of variable thickness disks made of either functionally graded (FG) materials [29-42] or traditional materials [43-46] are not enough. In those studies, a variable-thickness disk is generally considered as a combination of multi-layered uniform disks [29, 30-32, 34, 36, 40]. For example, Chiba [29] assumed the annular disk is to be a multilayered one with stepwise thickness variation, where each layer is assumed to have constant deterministic material properties. Bayat et al. [30] considered a rotating FG disk with either parabolic or hyperbolic thickness under a steady temperature field. The disk was assumed to be composed of sub-disks of uniform thicknesses. In another study, Bayat et al. [31] analyzed the thermoelastic bending of FGM rotating disks based on the first order shear deformation theory. Bayat et al. [32] studied on a thermo elastic analysis for axisymmetric rotating disks made of temperature-dependent power-law FG material with variable thickness. It was assumed in Ref. [32] that the temperature field is to be uniformly distributed over the disk surface and varied in the radial direction. Bayat et al. [32] presented semi-analytical solutions for the displacement field for solid/annular disks under free-free and fixed-free boundary conditions. Bayat et al. [33] also offered exact elastic solutions for axisymmetric variable-thickness hollow rotating disks with heat source made of functionally power-law-graded (FG) materials under free-free and fixed-free boundary conditions. They showed that the temperature distribution in a hyperbolic disk is the smallest compared with other thickness profiles. A hyperbolic-convergent FG disk has smaller stresses because of thermal load compared with the uniform disk. Nie and Batra [35] studied axisymmetric stresses in a rotating disk made of a rubber-like material that was modeled as isotropic, linear thermoelastic, and incompressible. Damircheli and Azadi [36] carried out thermal and mechanical stress analyses of a rotating disk having either parabolically or hyperbolically varying thicknesses made of functionally graded material by using finite element method (FEM). By utilizing a 2D plane stress analysis and assuming a power form temperature distribution of over the disk with the higher temperature at the outer surface, Hassani et al. [37] obtained stress and strains of rotating disks with non-uniform thickness and material properties subjected to thermo-elastic loading

under different boundary conditions. They used semi-exact methods of Liao's homotopy analysis method (HAM), Adomian's decomposition method and He's variational iteration method (VIM). Hassani et al. [37] compared the results of those three methods with Runge–Kutta's solutions. Tütüncü and Temel [38] studied numerically the thermoelastic analysis of FG rotating disks of variable thickness. Golmakani [39] scrutinized large deflection thermoelastic analysis of FG solid and hollow rotating axisymmetric disk with uniform and variable thickness subjected to thermo-mechanical loading. Kurşun and Topçu [40] handled the elastic stress analysis of a hollow disk with variable thickness made of FG materials under linearly increasing temperature distribution. Mahdavi et al. [41] worked on the thermoplastic analysis of FG rotating hyperbolic disks by dividing the domain into some finite sub-domains in the radial direction, in which the properties were assumed to be constant. Recently, Jabbari et al. [42] presented a thermoelastic analysis of rotating disks with different thickness profiles made of power-graded and exponential-graded materials subjected to internal pressure. They verified the results with finite element method.

As stated above, there are also relatively less study on the thermal-related analyses of isotropic and homogeneous disks with varying thickness. By using hyper-geometric differential equation in terms of radial displacement, Vivio and Vullo [43] and Vullo and Vivio [44] introduced an analytical procedure for evaluation of elastic stresses and strains in rotating conical disks and in non-linear variable thickness rotating disks made of an isotropic and homogeneous material, either solid or annular, subjected to thermal loads. In the presence of the linear thermal gradient, Garg et al. [45] analyzed the steady state creep in a rotating disk having linearly varying thickness and made of composite containing silicon carbide particles (SiC) in a matrix of pure aluminium. Çetin et al. [46] studied analytically an elastic stress analysis of annular isotropic and homogeneous bi-material hyperbolic disks subjected to the mechanical and thermo-mechanical loads.

As can be seen from the literature survey mentioned above, the realm of the thermal-related analyses of such disks having varying thicknesses needs further works.

In the present study, the exact distribution of the temperature along the radial coordinate in a hyperbolic disk is, first, obtained analytically based on the solution of Fourier heat-conduction differential equation under thermal boundary conditions defined by specified surface temperatures. This closed-form solution for temperature distribution is, then, substitute in the Navier equation obtained for the elasto-static response of such disks. Finally, Navier equations containing thermal effects are solved by applying mechanical boundary conditions. In the solution process of both the heat conduction and Navier equations, both of which are in the form of a second order differential equation with constant coefficients, a well-known Euler-Cauchy technique is employed [47]. Those formulas are compared with those available in the open literature.

## 2. Formulation of the Thermal Behavior of the Disk

An accurate solution of the temperature field in the structure is a crucial first step to study the thermal-related analyses in an appropriate manner. The rate of the heat flux,  $\mathbf{q}$ , in a solid object is proportional to the temperature gradient,  $\nabla T$ . The Fourier law governing the heat transfer by conduction is

$$\mathbf{q} = -k\nabla T = -k \text{ grad}(T) \quad (1)$$

where  $k$  is the thermal conductivity. Temperature gradient is given in cylindrical coordinates,  $(r, \theta, z)$ , by

$$\nabla T = \text{grad}(T) = \frac{\partial T}{\partial r} \mathbf{e}_r + \frac{1}{r} \frac{\partial T}{\partial \theta} \mathbf{e}_\theta + \frac{\partial T}{\partial z} \mathbf{e}_z \quad (2)$$

where  $(\mathbf{e}_r, \mathbf{e}_\theta, \mathbf{e}_z)$  are the unit vectors in cylindrical coordinates,  $r$  is the radial coordinate,  $\theta$  is the circumferential coordinate. By using the first law of thermodynamics, Fourier heat conduction equation may be written as follows.

$$\rho c_p \frac{\partial T}{\partial t} + \text{div}(\mathbf{q}) = \dot{q}_{gen} \quad (3)$$

where  $\rho$  is the density, and  $c_p$  is the specific heat capacity,  $\dot{q}_{gen}$  is the heat generation per unit volume. Using Eq. (1) the following may be written for the divergence of the heat flux as

$$\text{div}(\mathbf{q}) = \nabla \cdot \mathbf{q} = -k(\nabla \cdot \nabla T) = -k\Delta T = -k\nabla^2 T \quad (4)$$

By assuming that there is no heat generation in the structure,  $\dot{q}_{gen} = 0$ , and the steady state case ( $\partial T / \partial t = 0$ ) exists, substitution of Eq. (4) into the heat conduction equation (3) gives the Laplacian of the temperature that is the divergence of the gradient of the temperature as follows

$$k\nabla^2 T = k \left( \frac{1}{r} \frac{\partial}{\partial r} \left( r \frac{\partial T}{\partial r} \right) + \frac{1}{r^2} \frac{\partial^2 T}{\partial \theta^2} + \frac{\partial^2 T}{\partial z^2} \right) = 0 \quad (5)$$

This is a differential equation governing steady state 3-D temperature distribution for both cylinders and discs having uniform thickness and constant thermal conductivity without heat generation. As observed from this equation and Eq. (1), both the temperature field and heat flux distribution will be the same for both cylinders and disks with uniform thickness. However, a disk with variable thickness offers different temperature and heat flux profiles than hollow cylinders and uniform disks even for a constant thermal conductivity. For axisymmetric problems (derivatives with respect to  $\theta$  and  $z$  are all zero) of a variable thickness disk, Eq. (5) takes the form of

$$\frac{k}{rh(r)} \frac{d}{dr} \left( rh(r) \frac{dT(r)}{dr} \right) = 0 \quad (6)$$

It can be concluded from the above that the temperature field is to be the same for all materials exhibiting both isotropy and homogeneity properties as in the traditional materials although the material type is to be of important in the heat flux calculations. For any thickness profile,  $h(r)$ , defined by a differentiable function, Eq. (6) may also be written as

$$\frac{d^2 T(r)}{dr^2} + \left( \frac{1}{r} + \frac{dh(r)}{dr} \frac{1}{h(r)} \right) \frac{dT(r)}{dr} = 0 \quad (7)$$

Now, consider a hyperbolic disc profile defined by

$$h(r) = h_o \left( \frac{r}{a} \right)^m \quad (8)$$

where  $a$  denotes the inner radius of the disk,  $m$  is the profile parameter, and  $h_o$  is the reference thickness (Fig. 1). While  $m > 0$  defines divergent hyperbolic profiles,  $m < 0$  identifies convergent ones. Uniform thickness disks are characterized by  $m = 0$  (Fig. 1).

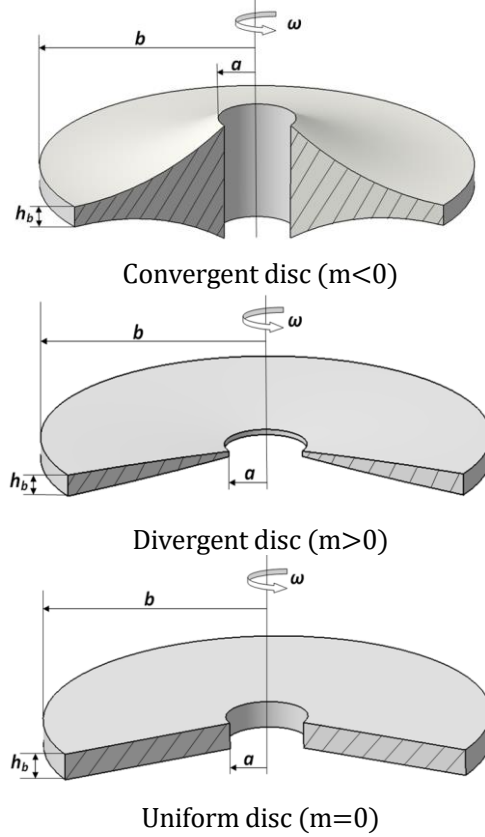


Fig. 1. 3-D view of convergent/divergent hyperbolic and uniform disc profiles

Substitution of Eq. (8) into Eq. (7) gives

$$\frac{d^2T(r)}{dr^2} + \frac{(1+m)}{r} \frac{dT(r)}{dr} = 0 \quad (9)$$

This is an Euler-Cauchy type differential equation with constant coefficients. Solution of Eq. (9) is given by [47]

$$T(r) = C_1 r^{\mu_1} + C_2 r^{\mu_2} \quad (10)$$

where  $\mu_1$  and  $\mu_2$  are the distinct characteristic real roots of the differential equation while  $C_1$  and  $C_2$  are integration constants. All types of thermal boundary conditions such as Dirichlet's, Neumann's, Robin's and mixed boundary conditions may be applied to determine the integration constants of the physical problem. In the present study the first kind boundary conditions (Dirichlet) are to be considered.

$$T(a) = T_a, \quad T(b) = T_b \quad (11)$$

In the above,  $T_a$  and  $T_b$  are the inner surface and outer surface temperatures, respectively. Considering Eq. (10) together with Eq. (11), a closed form solution for the temperature distribution in a hyperbolic disk along the radial coordinate is obtained as follows

$$T(r)^{(hyperbolic)} = r^{-m} \left( \frac{a^m b^m (T_b - T_a)}{a^m - b^m} \right) + \left( \frac{a^m T_a - b^m T_b}{a^m - b^m} \right) = r^{-m} \psi_1 + \psi_2 \quad (12)$$

As seen from Eq. (12), temperature distribution in a hyperbolic disk becomes indefinite when the uniform thickness is concerned with  $m = 0$ . In this case either a numerical value very close to zero but not exactly equal to zero such as  $m = 0.000000000001$  may be used directly in Eq. (12) or Eq. (9) is resolved for  $m = 0$  under the same boundary conditions [11] to get the following

$$T(r)^{(uniform)} = \left( \frac{\ln a T_b - T_a \ln b}{\ln a - \ln b} \right) + \left( \frac{T_a - T_b}{\ln a - \ln b} \right) \ln r = \phi_2 + \phi_1 \ln r \quad (13)$$

### 3. Formulation of the Thermo-mechanical Behavior of the Disk

Under small deformations and a state of axisymmetric plane stress assumptions for thin plates, field equations of a variable thickness rotating disk made of a traditional material in polar coordinates  $(r, \theta)$  are reduced to

$$\varepsilon_r(r) = \frac{du_r(r)}{r}, \quad \varepsilon_\theta(r) = \frac{u_r(r)}{r} \quad (14a)$$

$$\sigma_r(r) = \frac{E}{(1-\nu^2)} \varepsilon_r(r) + \frac{E\nu}{(1-\nu^2)} \varepsilon_\theta(r) - \frac{E(1+\nu)}{(1-\nu^2)} \alpha T \quad (14b)$$

$$\sigma_\theta(r) = \frac{E\nu}{(1-\nu^2)} \varepsilon_r(r) + \frac{E}{(1-\nu^2)} \varepsilon_\theta(r) - \frac{E(1+\nu)}{(1-\nu^2)} \alpha T \quad (14c)$$

$$\frac{d}{dr} (rh(r)\sigma_r(r)) - h(r)\sigma_\theta(r) = -\rho h(r)\omega^2 r^2 \quad (14d)$$

where  $u_r(r)$  is the radial displacement,  $\varepsilon_r(r)$  and  $\varepsilon_\theta(r)$  are the radial and circumferential strains, respectively;  $\sigma_r(r)$  is the radial stress,  $\sigma_\theta(r)$  is the hoop stress,  $\omega$  is a constant angular velocity,  $\rho$  is the material density,  $E$  is Young's modulus,  $\alpha$  is the coefficient of expansion of the disc material and  $\nu$  is Poisson's ratio.

Equations (14a) are called the strain-displacement relations, Eqs. (14b) and (14c) are referred to as linear elastic stress-strain relations, and finally Eq. (14d) is the equilibrium equation under the centrifugal forces. Navier equation which is in the form of a second order differential equation with variable coefficients is derived from the field equations given in Eq. (14) as follows

$$\begin{aligned} \frac{d^2 u_r(r)}{dr^2} + \left( \frac{1}{r} + \frac{dh(r)}{dr} \frac{1}{h(r)} \right) \frac{du_r(r)}{dr} \\ + \left( -\frac{1}{r^2} + \frac{\nu}{r} \frac{dh(r)}{dr} \frac{1}{h(r)} \right) u_r(r) = -\frac{(1-\nu^2)}{E} \rho \omega^2 r - \alpha(1+\nu) \frac{dT(r)}{dr} \end{aligned} \quad (15)$$

By using Eqs. (8) and (12), Eq. (15) may be written for a hyperbolic disk as follows

$$\frac{d^2 u_r(r)}{dr^2} + \frac{(1+m)}{r} \frac{du_r(r)}{dr} + \frac{(-1+mv)}{r^2} u_r(r) = -\frac{(1-\nu^2)}{E} \rho \omega^2 r + r^{-(1+m)} \Delta \quad (16)$$

where

$$\Delta = -m\alpha(1+\nu)\psi_1 \quad (17)$$

For a uniform thickness disk, Eq. (15) is rewritten by considering Eq. (13) as follows [10]

$$\frac{d^2 u_r(r)}{dr^2} + \frac{1}{r} \frac{du_r(r)}{dr} - \frac{1}{r^2} u_r(r) = -\frac{(1-\nu^2)}{E} \rho \omega^2 r + \alpha(1+\nu) \frac{\phi_1}{r} \quad (18)$$

#### 4. Closed-form Solutions of Navier Equations

The closed-form solutions of both Eqs. (16) and (18) under each mechanical boundary conditions presented in Table 1 are to be given in this section. Those formulas may be used by recalling that the superposition principle holds.

$$u_r(r)^{(Thermomechanical)} = u_r(r)^{(Pressure)} + u_r(r)^{(Rotation)} + u_r(r)^{(Thermal)} \quad (19)$$

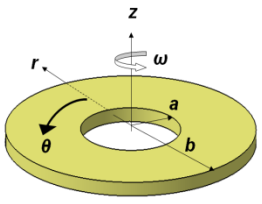
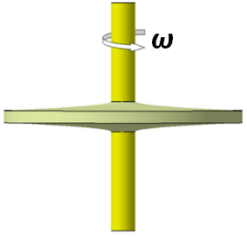
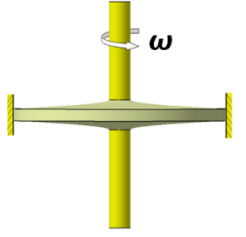
$$\sigma_r(r)^{(Thermomechanical)} = \sigma_r(r)^{(Pressure)} + \sigma_r(r)^{(Rotation)} + \sigma_r(r)^{(Thermal)}$$

$$\sigma_\theta(r)^{(Thermomechanical)} = \sigma_\theta(r)^{(Pressure)} + \sigma_\theta(r)^{(Rotation)} + \sigma_\theta(r)^{(Thermal)}$$

The equivalent von-Mises stresses by an axisymmetric plane stress assumption may be computed by

$$\sigma_{eq}(r)^{(Thermomechanical)} = \left( \sqrt{\sigma_r(r)^2 + \sigma_\theta(r)^2} - \sigma_r(r)\sigma_\theta(r) \right)^{(Thermomechanical)} \quad (20)$$

Table 1. Mechanical boundary conditions

Free-Free (circular annulus)	Fixed-Free (mounted disk)	Fixed-Fixed (mounted and cased disk)
		
$\sigma_r(a) = -p_a$ $\sigma_r(b) = -p_b$	$u_r(a) = 0$ $\sigma_r(b) = -p_b$	$u_r(a) = 0$ $u_r(b) = 0$

#### 4.1. Under Mechanical Pressure Loads

Elastic fields in a hyperbolic disk subjected to both the internal and external pressures ( $\omega = 0$ ,  $\alpha = 0$ ) are found under free-free conditions as

$$u_r(r)_{(Free-Free)}^{(Pressure)} = \left\{ -\frac{2(\nu^2 - 1)p_a a^{\frac{1}{2}(m+\phi+2)} r^{\frac{1}{2}(-m-\phi)} \left( \begin{array}{l} b^\phi(m - 2\nu - \phi) \\ -r^\phi(m - 2\nu + \phi) \end{array} \right)}{E(a^\phi - b^\phi)(m - 2\nu + \phi)(-m + 2\nu + \phi)} \right\} \\ + \left\{ -\frac{2(\nu^2 - 1)p_b b^{\frac{1}{2}(m+\phi+2)} r^{\frac{1}{2}(-m-\phi)} \left( \begin{array}{l} a^\phi(-m + 2\nu + \phi) \\ +r^\phi(m - 2\nu + \phi) \end{array} \right)}{E(a^\phi - b^\phi)(m - 2\nu + \phi)(-m + 2\nu + \phi)} \right\} \quad (21a)$$

$$\sigma_r(r)_{(Free-Free)}^{(Pressure)} = \left\{ \frac{p_a a^{\frac{1}{2}(m+\phi+2)} (b^\phi - r^\phi) r^{\frac{1}{2}(-m-\phi-2)}}{a^\phi - b^\phi} \right\} \\ + \left\{ \frac{p_b (a^\phi - r^\phi) b^{\frac{1}{2}(m+\phi+2)} r^{\frac{1}{2}(-m-\phi-2)}}{b^\phi - a^\phi} \right\} \quad (21b)$$

$$\sigma_\theta(r)_{(Free-Free)}^{(Pressure)} = \left\{ \frac{p_a a^{\frac{1}{2}(m+\phi+2)} r^{\frac{1}{2}(-m-\phi-2)} \left( \begin{array}{l} b^\phi(m - 2\nu - \phi)(\nu(m + \phi) - 2) \\ +r^\phi(m - 2\nu + \phi)(-m\nu + \nu\phi + 2) \end{array} \right)}{(a^\phi - b^\phi)(m - 2\nu - \phi)(m - 2\nu + \phi)} \right\} \\ + \left\{ \frac{p_b b^{\frac{1}{2}(m+\phi+2)} r^{\frac{1}{2}(-m-\phi-2)} \left( \begin{array}{l} a^\phi(m - 2\nu - \phi)(\nu(m + \phi) - 2) \\ +r^\phi(m - 2\nu + \phi)(-m\nu + \nu\phi + 2) \end{array} \right)}{(a^\phi - b^\phi)(m - 2\nu + \phi)(-m + 2\nu + \phi)} \right\} \quad (21c)$$

under fixed-free conditions as

$$u_r(r)_{(Fixed-Free)}^{(External Pressure)} = \left\{ -\frac{2(\nu^2 - 1)p_b (a^\phi - r^\phi) b^{\frac{1}{2}(m+\phi+2)} r^{\frac{1}{2}(-m-\phi)}}{E(a^\phi(m - 2\nu + \phi) + b^\phi(-m + 2\nu + \phi))} \right\} \quad (22a)$$

$$\sigma_r(r)_{(Fixed-Free)}^{(External Pressure)} = \left\{ -\frac{p_b b^{\frac{1}{2}(m+\phi+2)} r^{\frac{1}{2}(-m-\phi-2)} \left( \begin{array}{l} a^\phi(m - 2\nu + \phi) \\ +r^\phi(-m + 2\nu + \phi) \end{array} \right)}{a^\phi(m - 2\nu + \phi) + b^\phi(-m + 2\nu + \phi)} \right\} \quad (22b)$$

$$\sigma_\theta(r)_{(Fixed-Free)}^{(External Pressure)} = \left\{ -\frac{p_b b^{\frac{1}{2}(m+\phi+2)} r^{\frac{1}{2}(-m-\phi-2)} \left( \begin{array}{l} a^\phi(\nu(m + \phi) - 2) \\ +r^\phi(-m\nu + \nu\phi + 2) \end{array} \right)}{a^\phi(m - 2\nu + \phi) + b^\phi(-m + 2\nu + \phi)} \right\} \quad (22c)$$

In Eqs. (21) and (22)

$$\Phi = \sqrt{4 + m^2 - 4m\nu} \quad (23)$$

Equation (21) is a special application of formulas derived for functionally graded disks in Ref. [48]. Homogeneous solutions of Eq. (18) for free-free disks are ( $\omega = 0$ ,  $\alpha = 0$ )

$$u_r(r)_{(Free-Free/Uniform\ Thickness)}^{(Pressure)} = \left\{ -\frac{a^2 p_a (b^2 (\nu + 1) - (\nu - 1) r^2)}{Er(a^2 - b^2)} \right\} + \left\{ \frac{b^2 p_b (a^2 (\nu + 1) - (\nu - 1) r^2)}{Er(a^2 - b^2)} \right\} \quad (24a)$$

$$\sigma_r(r)_{(Free-Free/Uniform\ Thickness)}^{(Pressure)} = \left\{ \frac{a^2 p_a (b^2 - r^2)}{r^2 (a^2 - b^2)} \right\} + \left\{ \frac{b^2 (a^2 - r^2) p_b}{r^2 (b^2 - a^2)} \right\} \quad (24b)$$

$$\sigma_\theta(r)_{(Free-Free/Uniform\ Thickness)}^{(Pressure)} = -\left\{ \frac{a^2 p_a (b^2 + r^2)}{r^2 (a^2 - b^2)} \right\} + \left\{ \frac{b^2 (a^2 + r^2) p_b}{r^2 (a^2 - b^2)} \right\} \quad (24c)$$

Closed-form solutions in Eq. (24) overlaps with Roark's formulas [49]. For a uniform mounted disk subjected to the only external pressure, solutions become

$$u_r(r)_{(Fixed-Free/Uniform\ Thickness)}^{(External\ Pressure)} = \left\{ \frac{b^2 (\nu^2 - 1) p_b (a - r)(a + r)}{Er(a^2 (\nu - 1) - b^2 (\nu + 1))} \right\} \quad (25a)$$

$$\sigma_r(r)_{(Fixed-Free/Uniform\ Thickness)}^{(External\ Pressure)} = \left\{ \frac{b^2 p_b ((\nu + 1) r^2 - a^2 (\nu - 1))}{r^2 (a^2 (\nu - 1) - b^2 (\nu + 1))} \right\} \quad (25b)$$

$$\sigma_\theta(r)_{(Fixed-Free/Uniform\ Thickness)}^{(External\ Pressure)} = \left\{ \frac{b^2 p_b (a^2 (\nu - 1) + (\nu + 1) r^2)}{r^2 (a^2 (\nu - 1) - b^2 (\nu + 1))} \right\} \quad (25c)$$

To the best of the author's knowledge, Eqs. (22) and (25) are offered for the first time in the present study. These equations may be directly used to better simulate aero-disks subjected to blade pressures.

## 4.2. Under Mechanical Centrifugal Forces

If a disk is assumed to only rotate about an axis passing through its centroid at a constant angular velocity, the general solution of Eq. (16) is to be

$$u_r(r)_{(Rotation)} = r^{\frac{1}{2}(-m-\Phi)} (B_1 + B_2 r^\Phi) + r^3 \Omega \quad (26a)$$

$$\sigma_r(r)_{(Rotation)} = \frac{1}{2} \left( \frac{E}{1 - \nu^2} \right) r^{\frac{1}{2}(-2-m-\Phi)} \left( \begin{array}{l} -B_1 (m - 2\nu + \Phi) \\ + B_2 r^\Phi (-m + 2\nu + \Phi) \\ + 2r^{\frac{1}{2}(6+m+\Phi)} (3 + \nu) \Omega \end{array} \right) \quad (26b)$$

$$\sigma_\theta(r)_{(Rotation)} = \frac{1}{2} \left( \frac{E}{1 - \nu^2} \right) r^{\frac{1}{2}(-2-m-\Phi)} \left( \begin{array}{l} B_2 r^\Phi (2 - m\nu + \nu\Phi) \\ - B_1 (-2 + \nu(m + \Phi)) \\ + 2r^{\frac{1}{2}(6+m+\Phi)} (1 + 3\nu) \Omega \end{array} \right) \quad (26c)$$

where

$$\Phi = \sqrt{4 + m^2 - 4m\nu}, \quad \Omega = \frac{(-1 + \nu^2) \rho \omega^2}{E(8 + m(3 + \nu))} \quad (27)$$

and

$$B_1^{(Free-Free)} = \frac{2(\nu + 3)\Omega a^\Phi b^{\frac{1}{2}(m+\Phi+6)} - 2(\nu + 3)\Omega b^\Phi a^{\frac{1}{2}(m+\Phi+6)}}{(a^\Phi - b^\Phi)(m - 2\nu + \Phi)} \quad (28a)$$

$$B_2^{(Free-Free)} = \frac{2(\nu + 3)\Omega \left( a^{\frac{1}{2}(m+\Phi+6)} - b^{\frac{1}{2}(m+\Phi+6)} \right)}{(a^\Phi - b^\Phi)(m - 2\nu - \Phi)}$$

$$B_1^{(Fixed-Free)} = \frac{\Omega b^\Phi a^{\frac{1}{2}(m+\Phi+6)}(m - 2\nu - \Phi) + 2(\nu + 3)\Omega a^\Phi b^{\frac{1}{2}(m+\Phi+6)}}{a^\Phi(m - 2\nu + \Phi) + b^\Phi(-m + 2\nu + \Phi)} \quad (28b)$$

$$B_2^{(Fixed-Free)} = -\frac{\Omega \left( a^{\frac{1}{2}(m+\Phi+6)}(m - 2\nu + \Phi) + 2(\nu + 3)b^{\frac{1}{2}(m+\Phi+6)} \right)}{a^\Phi(m - 2\nu + \Phi) + b^\Phi(-m + 2\nu + \Phi)}$$

$$B_1^{(Fixed-Fixed)} = \frac{\Omega \left( b^\Phi a^{\frac{1}{2}(m+\Phi+6)} - a^\Phi b^{\frac{1}{2}(m+\Phi+6)} \right)}{a^\Phi - b^\Phi} \quad (28c)$$

$$B_2^{(Fixed-Fixed)} = -\frac{\Omega \left( a^{\frac{1}{2}(m+\Phi+6)} - b^{\frac{1}{2}(m+\Phi+6)} \right)}{a^\Phi - b^\Phi}$$

Solutions (26) is a special case of the formulas in Refs. [50-51]. If a uniform rotating disk is concerned, solutions turn to be [10, 49]

$$u_r(r)_{(Free-Free/Uniform)}^{(Rotation)} = \frac{\rho\omega^2(a^2(\nu + 3)(b^2(\nu + 1) - (\nu - 1)r^2) - (\nu - 1)r^2(b^2(\nu + 3) - (\nu + 1)r^2))}{8Er} \quad (29a)$$

$$\sigma_r(r)_{(Free-Free/Uniform)}^{(Rotation)} = \frac{(\nu + 3)\rho\omega^2(a^2 - r^2)(r^2 - b^2)}{8r^2} \quad (29b)$$

$$\sigma_\theta(r)_{(Free-Free/Uniform)}^{(Rotation)} = \frac{\rho\omega^2(a^2(\nu + 3)(b^2 + r^2) + r^2(b^2(\nu + 3) - (3\nu + 1)r^2))}{8r^2} \quad (29c)$$

and

$$u_r(r)_{(Fixed-Free/Uniform)}^{(Rotation)} = \frac{(\nu^2 - 1)\rho\omega^2(a - r)(a + r) \left( \begin{array}{l} a^2(b^2(\nu + 1) - (\nu - 1)r^2) \\ + b^2((\nu + 1)r^2 - b^2(\nu + 3)) \end{array} \right)}{8Er(a^2(\nu - 1) - b^2(\nu + 1))} \quad (30a)$$

$$\sigma_r(r)_{(Fixed-Free/Uniform)}^{(Rotation)} = \frac{\rho\omega^2(r^2 - b^2) \left( \begin{array}{l} a^4(\nu^2 - 1) \\ - a^2(\nu - 1)(\nu + 3)(b^2 + r^2) \\ + b^2(\nu + 1)(\nu + 3)r^2 \end{array} \right)}{8r^2(a^2(\nu - 1) - b^2(\nu + 1))} \quad (30b)$$

$$\sigma_{\theta}(r)_{(Fixed-Free/Uniform)}^{(Rotation)} = \frac{\rho\omega^2 \begin{pmatrix} a^4(\nu^2 - 1)(b^2 + r^2) \\ -a^2(\nu - 1)(b^4(\nu + 3) + (3\nu + 1)r^4) \\ -b^2(\nu + 1)r^2(b^2(\nu + 3) - (3\nu + 1)r^2) \end{pmatrix}}{8r^2(a^2(\nu - 1) - b^2(\nu + 1))} \quad (30c)$$

and

$$u_r(r)_{(Fixed-Fixed/Uniform\ Thickness)}^{(Rotation)} = \frac{(\nu^2 - 1)\rho\omega^2(r^2 - a^2)(r^2 - b^2)}{8Er} \quad (31a)$$

$$\sigma_r(r)_{(Fixed-Fixed/Uniform\ Thickness)}^{(Rotation)} = \frac{\rho\omega^2 \begin{pmatrix} a^2((\nu + 1)r^2 - b^2(\nu - 1)) \\ +r^2(b^2(\nu + 1) - (\nu + 3)r^2) \end{pmatrix}}{8r^2} \quad (31b)$$

$$\sigma_{\theta}(r)_{(Fixed-Fixed/Uniform\ Thickness)}^{(Rotation)} = \frac{\rho\omega^2 \begin{pmatrix} a^2(b^2(\nu - 1) + (\nu + 1)r^2) \\ +r^2(b^2(\nu + 1) - (3\nu + 1)r^2) \end{pmatrix}}{8r^2} \quad (31c)$$

### 4.3. Under Thermal Loads

If a disk is assumed to be subjected only thermal loads induced by temperature differences at the inner and outer surfaces, the homogeneous plus particular solutions of Eq. (16) are to be

$$u_r(r)^{(Thermal)} = r^{-m} \left( r^{\frac{m-\Phi}{2}} (C_1 + C_2 r^{\Phi}) + r\chi \right) \quad (32a)$$

$$\sigma_r(r)^{(Thermal)} = -\frac{1}{2} \left( \frac{EA}{1-\nu^2} \right) r^{-1-m-\frac{\Phi}{2}} \begin{pmatrix} C_2 r^{\frac{m}{2}+\Phi} (m - 2\nu - \Phi) \\ + C_1 r^{m/2} (m - 2\nu + \Phi) \\ + 2r^{1+\frac{\Phi}{2}} (-1 + m - \nu)\chi \end{pmatrix} - \frac{E\alpha(r^{-m}\psi_1 + \psi_2)}{1-\nu} \quad (32b)$$

$$\sigma_{\theta}(r)^{(Thermal)} = \frac{1}{2} \left( \frac{E}{1-\nu^2} \right) r^{-1-m-\frac{\Phi}{2}} \begin{pmatrix} C_2 r^{\frac{m}{2}+\Phi} (2 - m\nu + \nu\Phi) \\ - C_1 r^{m/2} (-2 + \nu(m + \Phi)) \\ - 2r^{1+\frac{\Phi}{2}} (-1 + (-1 + m)\nu)\chi \end{pmatrix} - \frac{E\alpha(r^{-m}\psi_1 + \psi_2)}{1-\nu} \quad (32c)$$

where

$$\psi_1 = \frac{a^m b^m (-T_a + T_b)}{a^m - b^m}, \quad \psi_2 = \frac{a^m T_a - b^m T_b}{a^m - b^m} \quad (33)$$

$$\Delta = -m\alpha(1 + \nu)\psi_1, \quad \chi = \frac{\Delta}{m(-1 + \nu)}, \quad \Phi = \sqrt{4 + m^2 - 4m\nu}$$

and

$$C_1^{(Free-Free)} = \frac{a^{\frac{\Phi-m}{2}} b^{\frac{\Phi-m}{2}} \left( 2ab^{\frac{m+\Phi}{2}} (\alpha(\nu+1)(\psi_2 a^m + \psi_1) + \chi(m-\nu-1)) \right)}{(a^\Phi - b^\Phi)(m-2\nu+\Phi)}$$

(34a)

$$C_2^{(Free-Free)} = \frac{a^{-m/2} b^{-m/2} \left( 2a^{m/2} b^{\frac{\Phi}{2}+1} (\alpha(\nu+1)(\psi_2 b^m + \psi_1) + \chi(m-\nu-1)) \right)}{(a^\Phi - b^\Phi)(m-2\nu-\Phi)}$$

$$C_1^{(Fixed-Free)} = \frac{a^{\frac{\Phi-m}{2}} b^{\frac{\Phi-m}{2}} \left( a\chi b^{\frac{m+\Phi}{2}} (m-2\nu-\Phi) \right)}{a^\Phi (m-2\nu+\Phi) + b^\Phi (-m+2\nu+\Phi)}$$

(34b)

$$C_2^{(Fixed-Free)} = \frac{a^{-m/2} b^{-m/2} \left( 2a^{m/2} b^{\frac{\Phi}{2}+1} (\alpha(\nu+1)(\psi_2 b^m + \psi_1) + \chi(m-\nu-1)) \right)}{a^\Phi (m-2\nu+\Phi) + b^\Phi (-m+2\nu+\Phi)}$$

$$C_1^{(Fixed-Fixed)} = -\frac{\chi a^\Phi b^{\frac{1}{2}(-m+\Phi+2)} - \chi b^\Phi a^{\frac{1}{2}(-m+\Phi+2)}}{a^\Phi - b^\Phi}$$

(34c)

$$C_2^{(Fixed-Fixed)} = \frac{\chi (b^{\frac{1}{2}(-m+\Phi+2)} - a^{\frac{1}{2}(-m+\Phi+2)})}{a^\Phi - b^\Phi}$$

Elastic fields in a uniform disk due to the thermal loads are obtained as

$$u_r(r)_{(Free-Free/Uniform\ Thickness)}^{(Thermal)} = \frac{\begin{pmatrix} a^2(\nu+1) \ln a (\vartheta - 2\alpha\Psi_2) \left( \frac{b^2(\nu+1)}{-(\nu-1)r^2} \right) \\ -b^2(\nu+1) \ln b \left( \frac{a^2(\nu+1)}{-(\nu-1)r^2} \right) (\vartheta - 2\alpha\Psi_2) \\ +(\nu-1)r^2(a-b)(a+b) \left( \frac{2\alpha(\nu+1)\Psi_1 - \vartheta}{+\vartheta(\nu+1)\ln r} \right) \end{pmatrix}}{2(\nu-1)(\nu+1)r(a^2 - b^2)}$$

(35a)

$$\sigma_r(r)_{(Free-Free/Uniform\ Thickness)}^{(Thermal)} = -\frac{E(\vartheta - 2\alpha\Psi_2) \begin{pmatrix} b^2(r^2 - a^2) \ln b \\ +a^2 \ln a (b^2 - r^2) \\ +r^2(a^2 - b^2) \ln r \end{pmatrix}}{2(\nu-1)r^2(a^2 - b^2)}$$

(35b)

$$\sigma_\theta(r)_{(Free-Free/Uniform\ Thickness)}^{(Thermal)} = \frac{E \begin{pmatrix} (\nu+1)(\vartheta - 2\alpha\Psi_2) \begin{pmatrix} a^2 \ln a (b^2 + r^2) \\ -b^2(a^2 + r^2) \ln b \\ +r^2(b^2 - a^2) \ln r \end{pmatrix} \\ -\vartheta(\nu-1)r^2(a^2 - b^2) \end{pmatrix}}{2(\nu^2 - 1)r^2(a^2 - b^2)}$$

(35c)

and

$$u_r(r)_{(Fixed-Free/Uniform)}^{(Thermal)} = \frac{\begin{pmatrix} a^2\vartheta \ln a \left( \frac{b^2(\nu+1)}{-(\nu-1)r^2} \right) - \vartheta r^2 \ln r \left( \frac{b^2(\nu+1)}{-a^2(\nu-1)} \right) \\ -b^2(a^2-r^2) \left( \frac{-2\alpha(\nu+1)\Psi_1}{+(\nu+1)\ln b(\vartheta-2\alpha\Psi_2)+\vartheta} \right) \end{pmatrix}}{2a^2(\nu-1)r-2b^2(\nu+1)r} \quad (36a)$$

$$\sigma_r(r)_{(Fixed-Free/Uniform Thickness)}^{(Thermal)} = \frac{E \begin{pmatrix} (\nu+1)(\vartheta-2\alpha\Psi_2) \left( \frac{b^2 \ln b(a^2(\nu-1)-(\nu+1)r^2)}{+r^2 \ln r(b^2(\nu+1)-a^2(\nu-1))} \right) \\ +a^2(\nu-1)(b^2-r^2)(\vartheta-2\alpha(\nu+1)\Psi_1) \\ -a^2\vartheta(\nu^2-1)\ln a(b^2-r^2) \end{pmatrix}}{2(\nu^2-1)r^2(a^2(\nu-1)-b^2(\nu+1))} \quad (36b)$$

$$\sigma_\theta(r)_{(Fixed-Free/Uniform Thickness)}^{(Thermal)} = \frac{E \begin{pmatrix} a^2(\nu-1)(2\alpha(\nu+1)\Psi_1(b^2+r^2)-\vartheta(b^2+\nu r^2)) \\ +(\nu+1)(\vartheta-2\alpha\Psi_2) \left( \frac{r^2 \ln r(b^2(\nu+1)-a^2(\nu-1))}{-b^2 \ln b(a^2(\nu-1)+(\nu+1)r^2)} \right) \\ +a^2\vartheta(\nu^2-1)\ln a(b^2+r^2)+b^2\vartheta(\nu^2-1)r^2 \end{pmatrix}}{2(\nu^2-1)r^2(a^2(\nu-1)-b^2(\nu+1))} \quad (36c)$$

and

$$u_r(r)_{(Fixed-Fixed/Uniform Thickness)}^{(Thermal)} = \frac{\vartheta \begin{pmatrix} b^2(r^2-a^2)\ln b \\ +a^2 \ln a(b^2-r^2) \\ +r^2(a^2-b^2)\ln r \end{pmatrix}}{2r(a^2-b^2)} \quad (37a)$$

$$\sigma_r(r)_{(Fixed-Fixed/Uniform Thickness)}^{(Thermal)} = \frac{E \begin{pmatrix} a^2\vartheta \ln a((\nu+1)r^2-b^2(\nu-1)) \\ +b^2\vartheta \ln b(a^2(\nu-1)-(\nu+1)r^2) \\ -r^2(a^2-b^2) \left( \frac{-2\alpha(\nu+1)\Psi_1+\vartheta}{+(\nu+1)\ln r(\vartheta-2\alpha\Psi_2)} \right) \end{pmatrix}}{2(\nu^2-1)r^2(a^2-b^2)} \quad (37b)$$

$$\sigma_\theta(r)_{(Fixed-Fixed/Uniform Thickness)}^{(Thermal)} = \frac{E \begin{pmatrix} a^2\vartheta \ln a(b^2(\nu-1)+(\nu+1)r^2) \\ -b^2\vartheta \ln b(a^2(\nu-1)+(\nu+1)r^2) \\ -r^2(a^2-b^2) \left( \frac{-2\alpha(\nu+1)\Psi_1+\vartheta\nu}{+(\nu+1)\ln r(\vartheta-2\alpha\Psi_2)} \right) \end{pmatrix}}{2(\nu^2-1)r^2(a^2-b^2)} \quad (37c)$$

where

$$\Psi_1 = \frac{T_b \ln a - T_a \ln b}{\ln a - \ln b}, \quad \Psi_2 = \frac{T_a - T_b}{\ln a - \ln b} \quad (38)$$

$$\vartheta = \alpha(1+\nu)\Psi_2$$

## 5. Numerical Examples

A disk made of a stainless steel (SUS304) is chosen with the following properties in numerical examples.

$$\begin{aligned}
 a &= 0.5 \text{ m}; b = 1 \text{ m}; \omega = 100 \text{ (rad/s)} \\
 p_a &= 60 \text{ (MPa)}; p_b = 30 \text{ (MPa)}; T_b = 100 \text{ }^\circ\text{C}; T_a = 20 \text{ }^\circ\text{C} \\
 E &= 201.04 \text{ (GPa)}; \rho = 7800 \text{ (kg/m}^3\text{)}; \nu = 0.3262 \\
 \alpha &= 12.33 \cdot 10^{-6} \text{ (1/K)}; k = 15.379 \text{ (W/mK)}
 \end{aligned}$$

Dimensionless elastic fields are defined as follows

$$\begin{aligned}
 \bar{u}_r(r) &= \frac{E}{(1-\nu^2)\rho\omega^2b^3 + (1+\nu)\alpha ET_b b + bp_o} u_r(r) \\
 \bar{\sigma}_r(r) &= \frac{(1-\nu)}{(1-\nu)\rho\omega^2b^2 + \alpha ET_b + (1-\nu)p_o} \sigma_r(r) \\
 \bar{\sigma}_\theta(r) &= \frac{(1-\nu)}{(1-\nu)\rho\omega^2b^2 + \alpha ET_b + (1-\nu)p_o} \sigma_\theta(r)
 \end{aligned} \tag{39}$$

where  $p_o = p_a$  is used for both free-free and fixed-fixed boundary conditions while  $p_o = p_b$  for fixed-free surfaces.

As a first example, the radial temperature distribution in a hyperbolic disk is investigated regarding different profile parameters and aspect ratios defined by ( $a/b$ ). Solutions are illustrated by Fig. 2. As can be seen from Fig. 2 that the differences in the temperature distributions in a hyperbolic disk become much obvious as the aspect ratios get smaller. A convergent disk profile having  $m = -1$  exhibits a linear temperature distribution while the other profile parameters offer different curves. The temperatures at the intermediate surfaces of a disk having divergent profiles decrease faster than convergent ones towards the inner surface and increase slowly towards the outer. It is not suitable the use of a linear temperature profile instead of the true one, except  $m = -1$ , for even uniform disks as seen from Fig. 2.

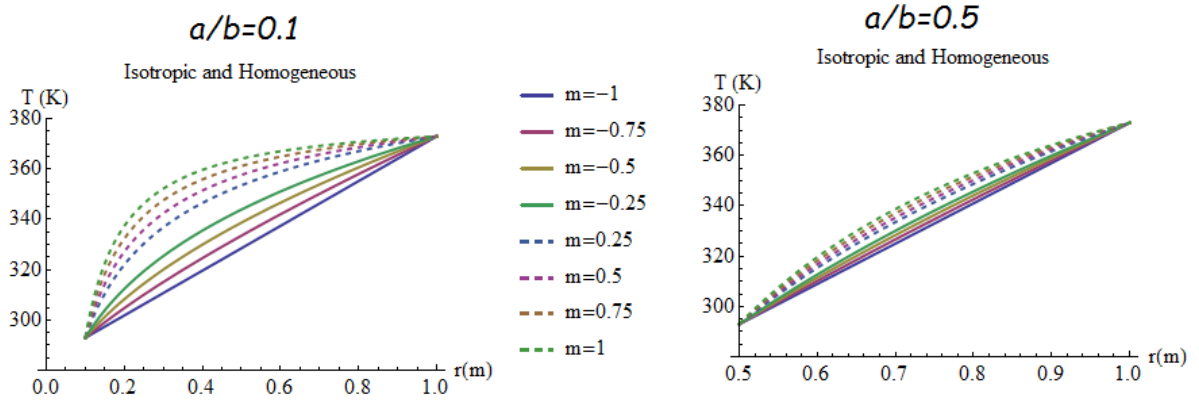


Fig. 2. Variation of the radial temperature distribution with the aspect ratios and profile parameters

As a second example, the radial variations of the elastic fields in a hyperbolic disk with the profile parameters are to be examined. Solutions for three boundary conditions are demonstrated by Fig. 3 in a comparative manner. The numerical values of some equivalent stresses are presented in Table 2.

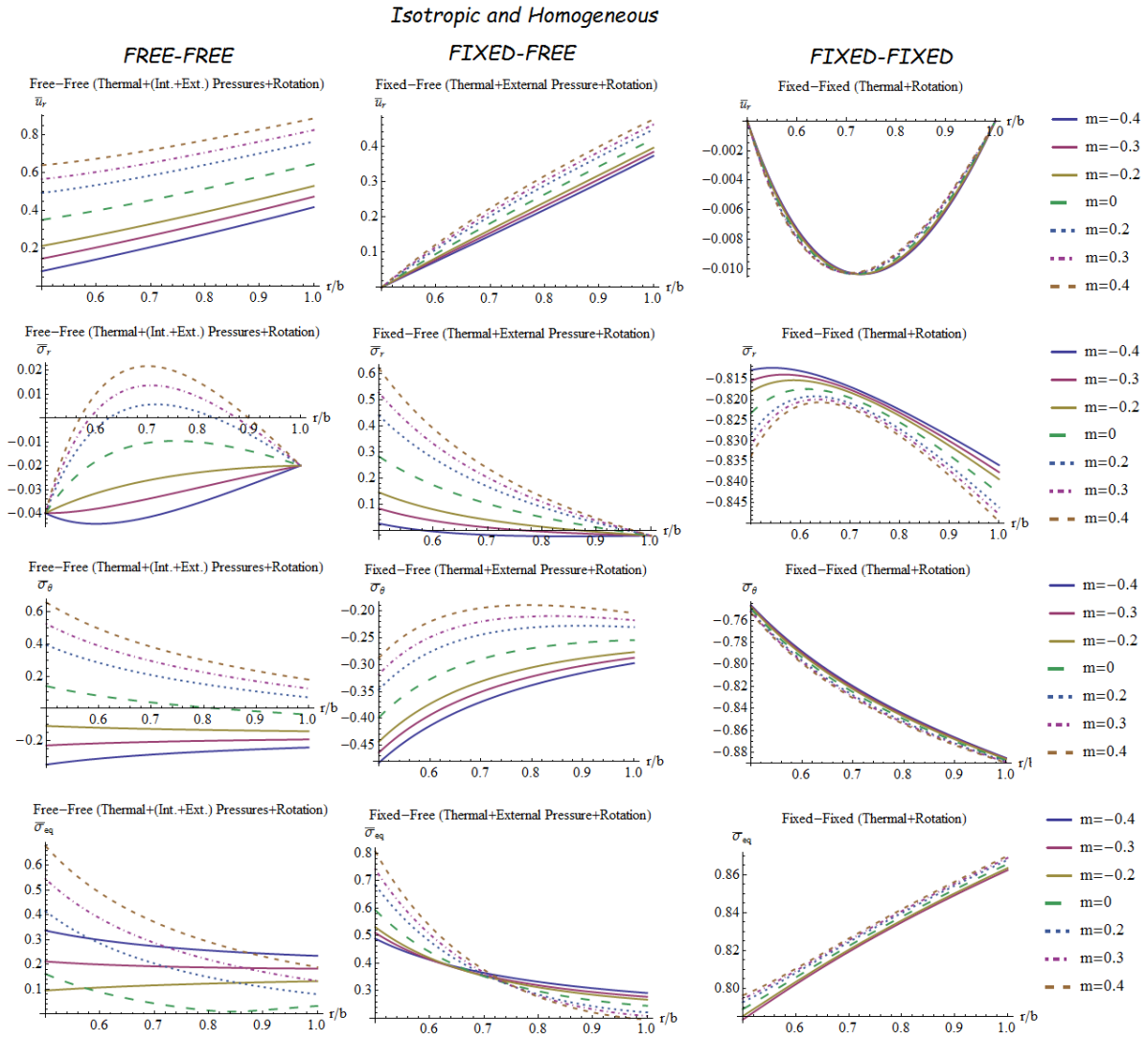


Fig. 3. The radial variations of the elastic fields in a hyperbolic disk with the profile parameters

As can be observed from Fig. 3 that, the curves are in accordance with the related boundary conditions. Observations from this figure are outlined below:

- i. The maximum radial displacement is located at the outer surface for free-free and fixed-free boundary conditions while it is in the vicinity of the mid-surface for fixed-fixed hyperbolic disks.
- ii. The convergent profiles offer smaller radial displacements than divergent and uniform ones under free-free and fixed-free boundary conditions. The radial displacements in divergent hyperbolic disks are higher than even uniform profiles under free-free and fixed-free boundary conditions.

- iii. The radial stress in free-free divergent hyperbolic disks is in compression at the vicinity of both the inner and outer surfaces while it is in tension at the vicinity of mid-surface. However, the radial stresses are all in compression in both uniform and convergent disks under free-free conditions.
- iv. The maximum radial stress is at the inner surface under both free-free and fixed-free conditions except for  $m = -0.4$  in free-free and fixed-fixed disks.
- v. Convergent disk profiles exhibit better response to the radial stress variation than both uniform and divergent ones for fixed-free disks.
- vi. Fixed-fixed disks have radial and hoop stresses which are completely in compression. Convergent disk profiles exhibit better response to the combined thermal and centrifugal loads than uniform and divergent ones under fixed-fixed boundary conditions.
- vii. When the variation of the hoop stresses are concerned, convergent profiles seem to be better than divergent ones under free-free and fixed-fixed boundaries. The converse is true for fixed-free hyperbolic disks.
- viii. For fixed-free disks, divergent profiles having higher parameter values in absolute present better hoop stress distribution.

Table 2. Equivalent stresses in a hyperbolic disk

		$m$						
		$-0.4$	$-0.3$	$-0.2$	$0 (1. \times 10^{-11})$	$0.2$	$0.3$	$0.4$
Fixed-Fixed (thermal + rotation) ( $p_o = p_a$ )								
0.5	0.916974	0.783478	0.785315	0.788975	0.792691	0.794532	0.796368	
0.6	0.980805	0.802161	0.803402	0.805805	0.808167	0.809306	0.810422	
0.7	1.02596	0.819335	0.820365	0.822386	0.824401	0.825389	0.826369	
0.8	1.06088	0.834924	0.835901	0.83786	0.839837	0.840827	0.84182	
0.9	1.08956	0.849215	0.85022	0.852247	0.854303	0.855335	0.856372	
1.	1.11416	0.862506	0.86359	0.865748	0.867921	0.868999	0.870072	
Fixed-Free (thermal + rotation+ external pressure) ( $p_o = p_b$ )								
0.5	0.489025	0.510427	0.531227	0.593047	0.68397	0.740794	0.805348	
0.6	0.412551	0.413534	0.418865	0.440813	0.479528	0.505501	0.535931	
0.7	0.364721	0.356252	0.353188	0.35219	0.359343	0.366401	0.375932	
0.8	0.332283	0.319776	0.312241	0.298309	0.286529	0.281748	0.277884	
0.9	0.309015	0.295211	0.285512	0.265198	0.243728	0.232593	0.221237	
1.	0.291673	0.277947	0.267494	0.245311	0.221319	0.208593	0.195358	
Free-Free (thermal + rotation+ internal and external pressures) ( $p_o = p_a$ )								
0.5	0.337384	0.212439	0.0952687	0.162293	0.41535	0.545674	0.678143	
0.6	0.299193	0.200208	0.10746	0.0890103	0.285386	0.386576	0.48942	
0.7	0.274373	0.192891	0.11637	0.0435495	0.204567	0.287646	0.372081	
0.8	0.257063	0.188267	0.123151	0.0145655	0.149327	0.219918	0.291667	
0.9	0.244496	0.185281	0.128545	0.0161429	0.109388	0.170738	0.233149	
1.	0.235186	0.18336	0.133007	0.033027	0.0805358	0.134429	0.189562	

- ix. For free-free disks, convergent profiles having smaller parameter values in absolute offer better hoop stress variations than divergent ones. For this boundary condition, the uniform disks exhibit the best response to the circumferential stresses together with  $m = -0.2$ .
- x. As to the equivalent von-Misses stresses, fixed-free and fixed-fixed boundaries need convergent disks having higher parameter values in absolute while free-free disks require convergent disk having smaller parameter values.
- xi. Convergent profiles may exhibit almost uniform equivalent stresses under free-free boundary conditions. According to Fig. 3,  $m = -0.2$  is the best for the distribution of equivalent von-Misses stresses under free-free conditions.

## 6. Conclusions

Closed-form formulas were proposed for hyperbolic disks made of traditional materials under free-free, fixed-free, and fixed-fixed boundary conditions to obtain the exact thermo-mechanical fields. Combined thermal loads, internal and external pressures, and centrifugal forces were considered as thermo-mechanical loads. Those formulas are to be very helpful tools in the pre-design stage of such disks.

To the best of the author's knowledge, formulas for the hyperbolic fixed-free disks subjected to the external pressure induced by the existence of the blades have been originally offered in the present study.

## References

- [1] Güven, U., Altay O., Elastic-plastic solid disk with nonuniform heat source subjected to external pressure, *Int J Mech Sci*, 42(5), 831-842, 2000.
- [2] Jahed, H., Shirazi, R., Loading and unloading behaviour of a thermoplastic disc, *Int. J Pressure Vessels Piping*, 78, 637-645, 2001.
- [3] Gogulwar, V.S., Deshmukh, K.C., An inverse quasi-static thermal stresses in an annular disc, *Proceeding of ICADS*, Narosa Publishing House, New Delhi, 2002.
- [4] Kulkarni, V.S., Deshmukh, K.C., Thermal stresses in a thick annular disc, *Journal of Thermal Stresses*, 31(4), 331-342, 2008.
- [5] Genç, M.S., Özşık, G., Yapıcı, H., A numerical study of the thermally induced stress distribution in a rotating hollow disc heated by a moving heat source acting on one of the side surfaces, *P I Mech Eng C-J Mec*, 223(8), 1877-1887, 2009.
- [6] Nejad, M.Z., Afshin, A., Transient thermoelastic analysis of pressurized rotating disks subjected to arbitrary boundary and initial conditions, *Chinese Journal of Engineering*, Article ID 894902, 13 pages, 2014. <http://dx.doi.org/10.1155/2014/894902>
- [7] Rattan, M., Kaushik, A., Chamoli, N., Steady state creep behavior of thermally graded isotropic rotating disc of composite taking into account the thermal residual stress, *European Journal of Mechanics A/Solids*, 60, 315-326, 2016.
- [8] Kaur, J., Thakur, P., Singh, S.B., Steady thermal stresses in a thin rotating disc of infinitesimal deformation with mechanical load, *Journal of Solid Mechanics*, 8(1), 204-211, 2016.
- [9] Nayak, P., Saha, K., Elastic limit angular speed of solid and annular disks under thermomechanical loading, *International Journal of Engineering, Science and Technology*, 8(2), 30-45, 2016.
- [10] Yıldırım, V., Heat-induced, pressure-induced and centrifugal-force-induced exact axisymmetric thermo-mechanical analyses in a thick-walled spherical vessel, an infinite

- cylindrical vessel, and a uniform disc made of an isotropic and homogeneous material, *Int J Eng Appl Sci (IJEAS)*, 9(2), 66-87, 2017. Doi: 10.24107/ijeas.309786.
- [11] Sayman, O. Thermal stress analysis in an aluminum metal-matrix orthotropic disc, *Journal of Reinforced Plastics and Composites*, 23, 1473-1479, 2004.
- [12] Çallıoğlu, H., Topçu, M., Altan, G., Stress analysis of curvilinearly orthotropic rotating discs under mechanical and thermal loading, *Journal of Reinforced Plastics and Composites*, 24(8), 831-838, 2005.
- [13] Çallıoğlu, H., Thermal stress analysis of curvilinear orthotropic rotating disks, *Journal of Thermoplastic Composite Materials*, 20, 357-369, 2007.
- [14] Sen, F., Sayer, M., Elasto-plastic thermal stress analysis in a thermoplastic composite disc under uniform temperature using FEM, *Mathematical and Computational Applications*, 11(1), 31-39, 2006.
- [15] Altan, G., Topçu, M., Bektaş, N.B., Altan, B.D., Elastic-plastic thermal stress analysis of an aluminum composite disc under parabolic thermal load distribution, *J. Mech. Sci. Technol.*, 22(12), 2318–2327, 2008.
- [16] Mohammadi, F., Hadadian, A., Singh, G.J., Analytical solution of pressurized rotating composite disk under thermal loading, *Proceedings of the World Congress on Engineering II: WCE 2010, London, U.K. (4 pages) 2010.*
- [17] Mustafa, M.T., Zubair, S.M., Arif, A.F.M., Thermal analysis of orthotropic annular fins with contact resistance: A closed-form analytical solution, *Appl. Therm. Eng.*, 31, 937–945, 2011.
- [18] Kansal, G., Parvez, M., Thermal stress analysis of orthotropic graded rotating discs, *International Journal of Modern Engineering Research (IJMER)*, 2(5), 3381-3885, 2012.
- [19] Stampoulouglou, I.H., Theotokoglou, E.E., The radially nonhomogeneous thermoelastic axisymmetric problem, *Int J Mech Sci*, 120, 311–321, 2017.
- [20] Bayat, M., Saleem, M., Sahari, B.B., Hamouda, A.M.S., Mahdi, E., Thermo elastic analysis of a functionally graded rotating disk with small and large deflections, *Thin-Wall Struct*, 45, 677–691, 2007.
- [21] Kordkheili, S.A.H., Naghdabadi, R., Thermoelastic analysis of a functionally graded rotating disk, *Compos Struct*, 79, 508–516, 2007.
- [22] Arani, A.G., Mozdianfard, M.R., Maraghi, Z.K., Shajari, A.R., Thermo-piezo-magneto-mechanical stresses analysis of FGPM hollow rotating thin disk, *Int J Mech Mater Des*, 6, 341–349, 2010.
- [23] Afsar, A.M., Go, J., Finite element analysis of thermoelastic field in a rotating FGM circular disk, *Appl. Math. Model*, 34, 3309–3320, 2010.
- [24] Peng, X.L., Li, X.F., Thermal stress in rotating functionally graded hollow circular discs, *Compos Struct*, 92(8), 1896–1904, 2010.
- [25] Kursun, A., Topçu, M., Tetik, T., Stress analysis of functionally graded disc under thermal and mechanical loads, *ICM11, Engineering Procedia*, 10, 2949–2954, 2011.
- [26] Gong, J.F., Ming, P.J., Xuan, L.K., Zhang, W.P., Thermoelastic analysis of three-dimensional functionally graded rotating disks based on finite volume method, *P I Mech Eng C-J Mec*, 228(4), 583–598, 2014.
- [27] Gonczi, D., Ecsedi, I., Thermoelastic analysis of functionally graded hollow circular disk, *Arch Mech Eng*, LXII, 5–18, 2015.
- [28] Yıldırım, V., Thermomechanical characteristics of a functionally graded mounted uniform disc with/without rigid casing, *The Journal of Aerospace Technology and Management (JATM)*, 2018. (to be published)
- [29] Chiba, R., Stochastic thermal stresses in an FGM annular disc of variable thickness with spatially random heat transfer coefficients, *Meccanica*, 44, 159–176, 2009.

- [30] Bayat, M., Saleem, M., Sahari, B.B., Hamouda, A.M.S, Mahdi E., Mechanical and thermal stresses in a functionally graded rotating disk with variable thickness due to radially symmetry loads, *Int. J Pressure Vessels Piping*, 86, 357–372, 2009.
- [31] Bayat, M., Sahari, B.B., Saleem, M., Ali, A., Wong, S.V., Thermoelastic solution of a functionally graded variable thickness rotating disk with bending based on the first-order shear deformation theory, *Thin-Wall Struct*, 47, 568–582, 2009.
- [32] Bayat, M., Sahari, B.B., Saleem, M., Hamouda, A.M.S., Reddy, J.N., Thermo elastic analysis of functionally graded rotating disks with temperature-dependent material properties: uniform and variable thickness, *Journal of Mechanics and Materials in Design*, 5(3), 263–279, 2009.
- [33] Bayat, M., Mohazzab, A.H., Sahari, B.B., Saleem, M., Exact solution for functionally graded variable-thickness rotating disc with heat source, *P I Mech Eng C-J Mec*, 224(11), 2316–2331, 2010.
- [34] Arani, G., Loghman, A., Shajari, A., Amir, S.A.R., Semi-analytical solution of magneto-thermo-elastic stresses for functionally graded variable thickness rotating disks, *J Mech Sci Technol*, 24(10), 2107–2117, 2010.
- [35] Nie, G.J., Batra, R.C., Stress analysis and material tailoring in isotropic linear thermoelastic incompressible functionally graded rotating disks of variable thickness, *Compos Struct*, 92, 720–729, 2010.
- [36] Damircheli, M., Azadi, M., Temperature and thickness effects on thermal and mechanical stresses of rotating FG-disks, *J Mech Sci Technol*, 25(3), 827-836, 2011.
- [37] Hassani, A., Hojjati, M.H., Farrahi, G., Alashti, R.A., Semi-exact elastic solutions for thermo-mechanical analysis of functionally graded rotating disks, *Compos Struct*, 93(12), 3239–3251, 2011.
- [38] Tutuncu, N., Temel, B., An efficient unified method for thermoelastic analysis of functionally graded rotating disks of variable thickness, *Mechanics of Advanced Materials and Structures*, 20(1), 38-46, 2013.
- [39] Golmakani, M.E., Large deflection thermoelastic analysis of shear deformable functionally graded variable thickness rotating disk, *Composites: Part B*, 45, 1143-1155, 2013.
- [40] Kurşun, A., Topçu, M., Thermal stress analysis of functionally graded disc with variable thickness due to linearly increasing temperature load, *Arab J Sci Eng*, 38, 3531–3549, 2013.
- [41] Mahdavi, E., AkbariAlashti, R., Darabi, A.C., Alizadeh, M., Linear thermoplastic analysis of FGM rotating discs with variable thickness, *Iranian Journal of Mechanical Engineering*, 14(2), 73-87, 2013.
- [42] Jabbari, M., Ghannad, M., Nejad, M.Z., Effect of thickness profile and FG function on rotating disks under thermal and mechanical loading, *Journal of Mechanics*, 32(1), 35-46, 2016.
- [43] Vivio, F., Vullo, V., Elastic stress analysis of rotating converging conical disks subjected to thermal load and having variable density along the radius, *Int J Solids Struct*, 44, 7767–7784, 2007.
- [44] Vullo, V., Vivio, F., Elastic stress analysis of non-linear variable thickness rotating disks subjected to thermal load and having variable density along the radius, *Int J Solids Struct*, 45, 5337–5355, 2008.
- [45] Garg, M., Salaria, B.S., Gupta, V.K., Effect of thermal gradient on steady state creep in a rotating disc of variable thickness, *Procedia Eng.*, 55, 542e547. 2013.
- [46] Çetin, E., Kurşun, A., Aksoy, Ş., Çetin, M.T., Elastic stress analysis of annular bi-material discs with variable thickness under mechanical and thermomechanical loads, *World Academy of Science, Engineering and Technology, International Journal of Mechanical, Aerospace, Industrial, Mechatronic and Manufacturing Engineering*, 8(2), 288-292, 2014.
- [47] Zwillinger, D. *Handbook of Differential Equations*, 3rd ed. Boston, MA: Academic Press, p. 120, 1997.

- [48] Yıldırım, V., Effects of inhomogeneity and thickness parameters on the elastic response of a pressurized hyperbolic annulus/disc made of functionally graded material, *Int J Eng Appl Sci*, 9(3), 2017. Doi: 10.24107/ijeas.329433
- [49] Young, W.C., Budynas, R.G., *Roark's Formulas for Stress and Strain*; McGraw Hill, Seventh Edition, New York. 2002.
- [50] Yıldırım, V., Analytic solutions to power-law graded hyperbolic rotating discs subjected to different boundary conditions, *International Journal of Engineering & Applied Sciences (IJEAS)*, 8(1), 38-52, 2016.
- [51] Yıldırım V., A parametric study on the centrifugal force-induced stress and displacements in power-law graded hyperbolic discs, *Latin American Journal of Solids and Structures, LAJSS*, 15(4) e34, 1-16, 2018. Doi: 10.1590/1679-78254229

## On the Stability Analysis of the General Mathematical Modeling of Bacterial Infection

Bahatdin Daşbaşı<sup>a\*</sup>, İlhan Öztürk<sup>b</sup>

<sup>a\*</sup> Kayseri University, Department of Accounting and Finance Management, Faculty of Applied Sciences, TR-38039, Kayseri, Turkey,

<sup>b</sup> Erciyes University, Department of Mathematics, Faculty of Sciences, TR-38039, Kayseri, Turkey  
E-mail address: [dasbasi\\_bahatdin@hotmail.com](mailto:dasbasi_bahatdin@hotmail.com)<sup>a\*</sup>, [ozturki@erciyes.edu.tr](mailto:ozturki@erciyes.edu.tr)<sup>b</sup>

ORCID numbers of authors:  
0000-0001-8201-7495<sup>a</sup>, 0000-0002-1268-6324<sup>b</sup>

Received date: 18.07.2018

Accepted date: 10.08.2018

### Abstract

*In this study, a mathematical model in form ODEs system examined the dynamics among populations of susceptible bacteria and resistant bacteria to antibiotic, antibiotic concentration and hosts immune system cells in an individual (or host), received antibiotic therapy in the case of a local bacterial infection, was proposed. For equilibrium points of this model, both local and global stability analysis have been also performed. In addition that, results of these analysis have been supported by numerical simulations.*

**Keywords:** Mathematical model, Stability analysis, Numerical simulation, Immune system, Antibiotic.

**2010 MSC Subject Classification:** 34D20, 34K60, 92C50, 92D25.

### 1. Introduction

Infections are shown as the main cause of diseases throughout human history and bacterial ones among these are more noticeable [1]. The first respond of host to such infections is through its immune system [2]. In this sense, the different host reactions to fight the same infection may be different due to hosts immune system response. If the host can not provide the respond required to destroy or limit the infection, then additional procedures can be needed. The most prevalent method for struggling bacterial infection is by way of antibiotic therapy. However, the most important problem derived from this therapy is the development of the bacteria resistance ability against the used antibiotic. Resistance to antimicrobial agents is both the reasonable and expected result of the use of these agents to treat human infections [3]. In this respect, the dynamics among antibiotic therapy, immune cells and bacteria in case of bacterial infection in host are significant to find out the character of the infection.

Mathematical models used in analyzed of biological applications are significant tools used not only in researching the spread of infectious diseases of individuals in a population, but also in estimating the timing and expansion of infection and possible reinfection processes in an individual [4,5]. Discovering the early dynamics of acute infections and foreseeing the time of



occurrence and magnitude of the maximum load of the bacteria and the immune system cells can be vital in choice of the efficient interference schemes [6].

In this study, it has been formed a continuous time model considering immune system response of host against bacteria causing infection and the main functions of bacterial resistance occurring due to effect of antibiotic. In this context, the aim of proposed model is to get the specific circumstances connected on the bacteria growth under the pressure of immune cells and antibiotic.

## 2. Mathematical Model

It has constituted this study by considering within-host models. Many of existing mathematical models, which assume that resistance development as a consequence of antibiotic use is in the host, are investigate how antibiotic treatment methods can both cause and be focused to avoid the occurrence of antibiotic resistance [7,8]. In addition that, the influences of the hosts immune system response due to the bacterial infection are often either ignored or presumed at a constant rate. In here, it has been generated the mathematical model comprising the effects of cell-mediated immune response. Also, treatment forms containing antibiotic have implemented in most bacterial infections. The effects of antibiotic therapy by using Holling function is examined. In this sense, it has been investigated the changes in concentrations of the bacteria and immune cells in a host receiving antibiotic treatment to fight off infectious bacteria by mathematical modelling.

It has presumed that  $S(t)$  and  $R(t)$  symbolize the population sizes of susceptible and resistant bacteria to antibiotic at time  $t$ , respectively. In addition that, it has assumed that  $B(t)$  and  $A(t)$  denote the population sizes of immune cells and the antibiotic concentration at time  $t$ , respectively. By aforementioned assumptions, it has obtained the following system of four ODE:

$$\begin{aligned}
 \frac{dS}{dt} &= \beta_S S \left(1 - \frac{S+R}{T}\right) - \bar{\eta} SB - S \frac{E_{max} A}{E_{50} + A} - \mu SA - \sigma SR \\
 \frac{dR}{dt} &= \beta_R R \left(1 - \frac{S+R}{T}\right) - \bar{\eta} RB + \mu SA + \sigma SR \\
 \frac{dB}{dt} &= \beta_B B \left(1 - \frac{B}{\Lambda}\right) - \lambda B(S + R) \\
 \frac{dA}{dt} &= -\alpha A
 \end{aligned} \tag{1}$$

where  $S \equiv S(t)$ ,  $R \equiv R(t)$ ,  $B \equiv B(t)$  and  $A \equiv A(t)$  and the system (1) has to be finished with positive initial conditions  $S(t_0) = S_0$ ,  $R(t_0) = R_0$ ,  $B(t_0) = B_0$  and  $A(t_0) = A_0$ . In addition, the expressions of these parameters are as follows: it is presumed that bacteria have a logistic growth rule and its the carrying capacity is  $T$ . The parameters  $\beta_S$  and  $\beta_R$  are the growth rate of susceptible and resistant bacteria, respectively. Specific mutations emerging resistance to chemical control often include an inherent fitness cost which may be outcomed through reduced reproductive capacity and/or competitive ability [6]. Therefore, it is

$$\beta_S > \beta_R \tag{2}$$

In the same mind in the bacteria growth, immune cells produce by logistic growth rule, and so, they are recruited to the site of infection at rate  $\beta_B$  and its carrying capacity is  $\Lambda$  [9,10]. Immune cells are lost through pathogen-induced apoptosis (at rate  $\lambda$ ). In the presence of the pathogen, this is biological meaningful when proliferation of immune cells is considered. These interacts among bacteria, immune cells and antibiotic have depicted a generalised mathematical model of a local bacterial infection, such as wound infection or tuberculosis. The above scenario related to the parameters used in the model (1) has been graphically described in Fig.1.

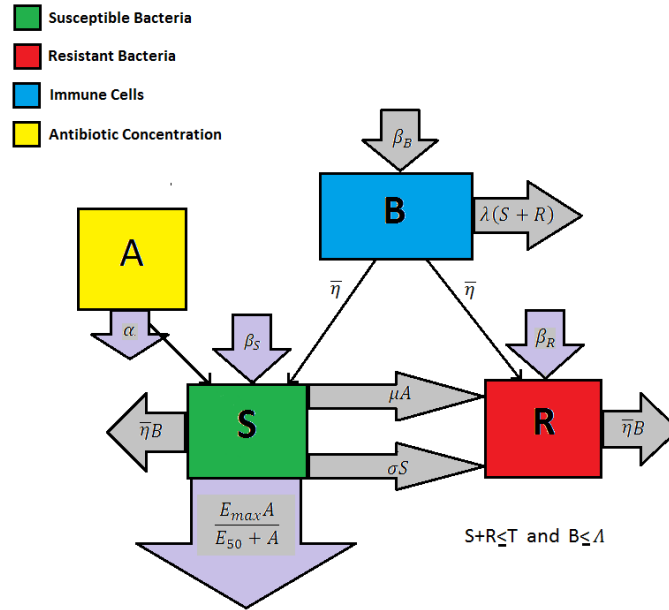


Fig.1. In the model (1), schematic representation of the main interactions involved in an infection treated by antibiotics with S (antibiotic-susceptible bacteria), R (antibiotic-resistant bacteria), B (immune cells, e.g. phagocytes or B cells), A (antibiotic concentration)

It is assumed that antibiotic has administered in dose  $\alpha$  [11,12]. Through the administration of the antibiotic, a number of resistant bacteria to this antibiotic can emerge due to mutations of susceptible bacteria exposed to such antibiotic and this case is modelled by  $\mu SA$  where the mutation rate of susceptible bacteria due to exposure to antibiotic is  $\mu$ . In addition that, the most common form of resistance acquisition to antibiotic is the conjugation including the transfer of genes between susceptible and resistant bacteria [13,14]. Since this transfer occurs between adjacent bacteria in a well mixed population [15,16], we have represented that this interaction through mass action kinetics with a conjugation rate,  $\sigma$ , being proportional to the levels of susceptible and resistant bacteria to antibiotic in the population [17,18].

Moreover, bacteria have per capita rates of death due to immune cells response of host, and so this rate in (1) is  $\bar{\eta}$ . In addition that, susceptible bacteria die due to the antibiotic effect. It has supposed that the effect of the antibiotic on susceptible bacteria is modelled by using a saturating response. This response is  $\frac{E_{max}A}{E_{50}+A}$  where  $E_{max}$  and  $E_{50}$  are the maximum killing rate and the antibiotic concentration needed for half maximum effect, respectively [11,17,19,20]. For the parameters used in the model, it has satisfied

$$\beta_S, \beta_R, \beta_B, T, \Lambda, \mu, \bar{\eta}, E_{max}, E_{50}, \sigma, \lambda, \alpha > 0. \quad (3)$$

For the ease analyze of the model (1), it has changed the variables as follows

$$s = \frac{S}{T}, r = \frac{R}{T}, b = \frac{B}{\Lambda}, a = \frac{A}{\frac{\bar{\eta}\Lambda}{\mu}}. \quad (4)$$

By (4), the model (1) transforms to following system:

$$\begin{aligned} \frac{ds}{dt} &= \eta \left( k_1 s (1 - (s + r)) - bs - \left( \frac{E_{max}}{E_{50}\mu + \eta a} + 1 \right) as - k_4 sr \right) \\ \frac{dr}{dt} &= \eta \left( k_2 r (1 - (s + r)) - br + as + k_4 sr \right) \\ \frac{db}{dt} &= \beta_B b ((1 - b) - k_3 (s + r)) \\ \frac{da}{dt} &= -\alpha a \end{aligned} \quad (5)$$

where

$$\begin{aligned} \frac{\beta_S}{\bar{\eta}\Lambda} = k_1, \frac{\beta_R}{\bar{\eta}\Lambda} = k_2, \frac{\lambda T}{\beta_B} = k_3, \frac{\sigma T}{\bar{\eta}\Lambda} = k_4, \bar{\eta}\Lambda = \eta, \\ k_1, k_2, k_3, k_4, \eta > 0 \end{aligned} \quad (6)$$

Moreover, it is obtained

$$k_1 > k_2 \quad (7)$$

by (2) and (6). The studied region as biological is given by the set

$$\Omega = \{(s, r, b, a) \in R^4: 0 \leq s, r, 0 \leq s + r \leq 1, 0 \leq b \leq 1, 0 \leq a \leq a(0)\}. \quad (8)$$

where  $a(0)$  is positive initial condition of  $a$ .

**Proposition 2.1.** The region  $\Omega$  defining in (8) is positively invariant for the system (5).

**Proof:** From the first and second equations in the system (5), it is

$$\frac{ds}{dt} + \frac{dr}{dt} = (k_1 s + k_2 r) \eta (1 - (s + r)) - b \eta (s + r) - as \frac{\eta E_{max}}{E_{50}\mu + \eta a} \quad (9)$$

Considering the region  $\Omega$ , it has reached the following inequality;

$$\frac{d(s+r)}{dt} \leq k_1\eta(s+r)(1-(s+r)). \quad (10)$$

By the solution according to  $(s+r)$  of inequality (10), it has followed that  $0 \leq s+r \leq 1$  for all  $t \geq 0$ . In the same mind, we have

$$\frac{db}{dt} \leq \beta_B b(1-b) \quad (11)$$

from third equation in system (5). Therefore, it has obtained  $0 \leq b \leq 1$  for all  $t \geq 0$  by (11).

Furthermore, the solution of the last equations of system (5) is

$$a(t) = a(0)e^{-at} \quad (12)$$

with positive initial conditions,  $a(0)$ . From (12), it is obtained that  $0 \leq a \leq a(0)$  for all  $t \geq 0$ . Let consider the vector field of the system (5) limited to the boundary of  $\Omega$ . This field does not includes a point at the exterior of it. Thereby, the solutions starting there is in the region  $\Omega$  for all  $t \geq 0$  and these solutions have biological meaning.

### 3. Qualitative Analysis of System (5)

In here, the equilibrium points of system (5) is founded. Lastly, the analyze of both the local stability and global stability of these equilibrium points is done.

#### 3.1. Equilibrium Points

We have accepted that the general terms of equilibria contained in  $\Omega$  of the system (5) show as  $E_j = (\bar{s}, \bar{r}, \bar{b}, \bar{a})$  for  $j = 1, 2, \dots, 6$ .

**Proposition 3.1.** The system (5) always has the infection-free equilibrium points  $E_0 = (0, 0, 0, 0)$  and  $E_1 = (0, 0, 1, 0)$ , and other points  $E_2 = (0, 1, 0, 0)$  and  $E_3 = (1, 0, 0, 0)$ . If  $k_3 < 1 < k_2$  or  $k_2 < 1 < k_3$ , then  $E_4 = \left(0, \frac{(k_2-1)}{(k_2-k_3)}, \frac{k_2(1-k_3)}{(k_2-k_3)}, 0\right)$  exists. Likewise, when  $k_3 < 1 < k_1$  or  $k_1 < 1 < k_3$ , then  $E_5 = \left(\frac{(k_1-1)}{(k_1-k_3)}, 0, \frac{k_1(1-k_3)}{(k_1-k_3)}, 0\right)$  reveals in  $\Omega$ . Moreover, if  $k_2 < \frac{(1-k_3)(k_1-k_2)}{k_4} + 1 < \min\left\{k_1, \frac{k_1-k_2}{k_4} + 1\right\}$ , then  $E_6 = \left(\frac{1}{k_4} - \frac{k_2 + \frac{k_3}{k_4}(k_1-k_2)}{k_1-k_2+k_4}, \frac{k_1 + \frac{k_3}{k_4}(k_1-k_2)}{k_1-k_2+k_4} - \frac{1}{k_4}, 1 - k_3 \frac{k_1-k_2}{k_1-k_2+k_4}, 0\right)$  exists as another equilibrium points.

**Proof:** The equilibrium points the system (5) in  $\Omega$  are obtained by solving the following system:

$$\begin{aligned} \eta s \left( k_1(1 - (s + r)) - b - \left( \frac{E_{max}}{E_{50}\mu + \eta a} + 1 \right) a - k_4 r \right) &= 0 \\ \eta r \left( k_2(1 - (s + r)) - b + a \frac{s}{r} + k_4 s \right) &= 0 \\ \beta_B b((1 - b) - k_3(s + r)) &= 0 \\ -\alpha a &= 0. \end{aligned} \quad (13)$$

From the last equation of system (13), we have  $\bar{a} = 0$  for all of the equilibrium points. Therefore, (13) transforms to

$$\begin{aligned} s(k_1(1 - (s + r)) - b - k_4 r) &= 0 \\ r(k_2(1 - (s + r)) - b + k_4 s) &= 0 \\ b((1 - b) - k_3(s + r)) &= 0. \end{aligned} \quad (14)$$

By solving (14), it is obtained the equilibrium points following:

$$\begin{aligned} E^I &= \left( \left( \frac{1}{-k_1 + k_2 - k_4} \right) k_2, - \left( \frac{1}{-k_1 + k_2 - k_4} \right) k_1, 0, 0 \right), \\ E_0 &= (0, 0, 0, 0), E_1 = (0, 0, 1, 0), E_2 = (0, 1, 0, 0), E_3 = (1, 0, 0, 0), \\ E_4 &= \left( 0, \frac{k_2 - 1}{k_2 - k_3}, \frac{k_2(1 - k_3)}{k_2 - k_3}, 0 \right), E_5 = \left( \frac{k_1 - 1}{k_1 - k_3}, 0, \frac{k_1(1 - k_3)}{k_1 - k_3}, 0 \right), \\ E_6 &= \left( \frac{1}{k_4} - \frac{k_2 + \frac{k_3}{k_4}(k_1 - k_2)}{k_1 - k_2 + k_4}, \frac{k_1 + \frac{k_3}{k_4}(k_1 - k_2)}{k_1 - k_2 + k_4} - \frac{1}{k_4}, 1 - k_3 \frac{k_1 - k_2}{(k_1 - k_2 + k_4)}, 0 \right). \end{aligned} \quad (15)$$

Althought the equilibrium points  $E_0, E_1, E_2$  and  $E_3$ , on the orijin,  $b$ -axis,  $r$ -axis and  $s$ -axis respectively, always exist in  $\Omega$ , the equilibrium point  $E^I$  in which signs of  $\bar{s}$  and  $\bar{r}$  are opposite due to (6), is not biological meaning. Thereby,  $E^I$  is not in  $\Omega$ . If  $0 < \frac{(k_2 - 1)}{(k_2 - k_3)} < 1$  and  $0 < \frac{k_2(1 - k_3)}{k_2 - k_3} < 1$ , that is,  $k_3 < 1 < k_2$  or  $k_2 < 1 < k_3$ , then an interior planar equilibrium  $E_4$  occuring in the  $r - b$  plane exists in  $\Omega$ . In the same mind, when  $0 < \frac{k_1 - 1}{k_1 - k_3} < 1$  and  $0 < \frac{k_1(1 - k_3)}{k_1 - k_3} < 1$ , that is,  $k_3 < 1 < k_1$  or  $k_1 < 1 < k_3$ ,  $E_5$  occurs in the  $s - b$  plane in  $\Omega$ .

Moreover, if  $0 < 1 - \frac{k_3(k_1 - k_2)}{k_1 - k_2 + k_4} < 1$ ,  $0 < \frac{1}{k_4} - \frac{k_2 + \frac{k_3}{k_4}(k_1 - k_2)}{k_1 - k_2 + k_4} < 1$  and  $0 < \frac{k_1 + \frac{k_3}{k_4}(k_1 - k_2)}{k_1 - k_2 + k_4} - \frac{1}{k_4} < 1$ , that is,  $k_2 < \frac{(1 - k_3)(k_1 - k_2)}{k_4} + 1 < \min \left\{ k_1, \frac{k_1 - k_2}{k_4} + 1 \right\}$ , then  $E_6$ , the interior equilibrium occuring in the  $s - r - b$  plane, exists in  $\Omega$ .

In table 1, proposition 3.1 is summarized.

Table 1. Biological meaning conditions for the equilibrium points founded in proposition 3.1.

The Equilibrium Point	The Biological Existence Condition
$E_0 = (0,0,0,0)$	Always exists
$E_1 = (0,0,1,0)$	Always exists
$E_2 = (0,1,0,0)$	Always exists
$E_3 = (1,0,0,0)$	Always exists
$E_4 = \left(0, \frac{(k_2 - 1)}{(k_2 - k_3)}, \frac{k_2(1 - k_3)}{(k_2 - k_3)}, 0\right)$	$k_3 < 1 < k_2$ or $k_2 < 1 < k_3$
$E_5 = \left(\frac{(k_1 - 1)}{(k_1 - k_3)}, 0, \frac{k_1(1 - k_3)}{(k_1 - k_3)}, 0\right)$	$k_3 < 1 < k_1$ or $k_1 < 1 < k_3$
$E_6 = \left(\frac{1}{k_4} - \frac{k_2 + \frac{k_3}{k_4}(k_1 - k_2)}{k_1 - k_2 + k_4}, \frac{k_1 + \frac{k_3}{k_4}(k_1 - k_2)}{k_1 - k_2 + k_4} - \frac{1}{k_4}, 1 - k_3 \left(\frac{k_1 - k_2}{k_1 - k_2 + k_4}\right), 0\right)$	$k_2 < \frac{(1 - k_3)(k_1 - k_2)}{k_4} + 1$ $< \min \left\{ k_1, \frac{k_1 - k_2}{k_4} + 1 \right\}$

### 3.2. The Analysis of Locally Asymptotically Stability of Equilibrium Points

**Theorem 3.1.** Let  $\frac{dX}{dt} = F(X)$  as a nonlinear first-order autonomous system with its equilibrium point  $\bar{X}$ . In addition that, it is assumed that the Jacobian matrix of  $F$  evaluated at  $\bar{X}$  is  $J(\bar{X})$ . If the characteristic equation of  $J(\bar{X})$ ,

$$\lambda^n + a_1\lambda^{n-1} + a_2\lambda^{n-2} + \dots + a_{n-1}\lambda + a_n = 0,$$

meets the Routh-Hurwitz criteria, that is, the determinants of all of the Hurwitz matrices are positive, then  $\bar{X}$  is locally asymptotically stable. If the determinants of the some Hurwitz matrices are negative, then  $\bar{X}$  is unstable point [21]. In this sense, the Routh-Hurwitz criteria for polynomial of degree  $n = 2, 3, 4$  and  $5$  of the above characteristic equation are summarized as following :

- $n = 2$ :  $a_1, a_2 > 0$ ,  
 $n = 3$ :  $a_1, a_3 > 0$  and  $a_1 a_2 > a_3$ ,  
 $n = 4$ :  $a_1, a_3, a_4 > 0$  and  $a_1 a_2 a_3 > a_3^2 + a_1^2 a_4$ ,  
 $n = 5$ :  $a_1, a_2, a_3, a_4, a_5 > 0$ ,  $a_1 a_2 a_3 > a_3^2 + a_1^2 a_4$   
 and  $(a_1 a_4 - a_5)(a_1 a_2 a_3 - a_3^2 - a_1^2 a_4) > a_5(a_1 a_2 - a_3)^2 + a_1 a_5^2$ .

Locally asymptotically stability (LAS) conditions of equilibrium points in the Table 1 have examined in the following proposition.

**Proposition 3.2.** For the equilibrium points in proposition 3.1, the followings are provided.

- (i)  $E_0$  and  $E_3$  are always unstable points.  
 (ii) If  $k_1 < 1$ , then  $E_1$  is LAS.  
 (iii) If  $1 < k_3$ , then  $E_2$  is LAS.  
 (iv) Let  $k_3 < 1 < k_2$  or  $k_2 < 1 < k_3$ . If  $1 < \frac{(1-k_3)(k_1-k_2)}{k_4} + 1 < k_2$ , then  $E_4$  is LAS.  
 (v) Let  $k_3 < 1 < k_1$  or  $k_1 < 1 < k_3$ . If  $1 < k_1 < \frac{(1-k_3)(k_1-k_2)}{k_4} + 1$ , then  $E_5$  is LAS.  
 (vi) Let  $k_2 < \frac{(1-k_3)(k_1-k_2)}{k_4} + 1 < \min\left\{k_1, \frac{k_1-k_2}{k_4} + 1\right\}$ . If  $k_3 < 1$ , then  $E_6$  is LAS.

**Proof:** For the stability analysis, the functions of the right side of the system (5) are adjusted as the following:

$$\begin{aligned}
 \varphi_1(s, r, b, a) &= \eta \left( k_1 s (1 - (s + r)) - bs - \left( \frac{E_{max}}{E_{50}\mu + \eta a} + 1 \right) as - k_4 sr \right) \\
 \varphi_2(s, r, b, a) &= \eta (k_2 r (1 - (s + r)) - br + as + k_4 sr) \\
 \varphi_3(s, r, b, a) &= \beta_B b ((1 - b) - k_3 (s + r)) \\
 \varphi_4(s, r, b, a) &= -\alpha a
 \end{aligned} \tag{16}$$

That jacobian matrix obtained from (16) is

$$J = \begin{pmatrix} \eta \left( k_1 (1 - (s + r)) - k_1 s - b \right) & -\eta s (k_1 + k_4) & -\eta s & -\eta s \left( \frac{E_{max} E_{50} \mu}{(E_{50} \mu + \eta a)^2} + 1 \right) \\ \eta \left( -k_4 r - \left( \frac{E_{max}}{E_{50} \mu + \eta a} + 1 \right) a \right) & \eta \left( k_2 (1 - (s + r)) \right) & -\eta r & \eta s \\ \eta (a + k_4 r - k_2 r) & -b + k_4 s - k_2 r & -\eta r & \eta s \\ -k_3 b \beta_B & -k_3 b \beta_B & \beta_B \begin{pmatrix} 1 - 2b \\ -k_3 (s + r) \end{pmatrix} & 0 \\ 0 & 0 & 0 & -\alpha \end{pmatrix} \tag{17}$$

Since  $\bar{a} = 0$  in all equilibria of the system (5), the jacobian matrix showed in (17) can be rewritten as follows:

$$J = \begin{pmatrix} \eta \begin{pmatrix} k_1(1 - (s + r)) \\ -k_1s - b - k_4r \end{pmatrix} & -\eta s(k_1 + k_4) & -\eta s & -\eta s \left( \frac{E_{max}}{E_{50\mu}} + 1 \right) \\ \eta r(k_4 - k_2) & \eta \begin{pmatrix} k_2(1 - (s + r)) \\ -b + k_4s - k_2r \end{pmatrix} & -\eta r & \eta s \\ -k_3b\beta_B & -k_3b\beta_B & \beta_B(1 - 2b - k_3(s + r)) & 0 \\ 0 & 0 & 0 & -\alpha \end{pmatrix} \quad (18)$$

For ease of examination, we have assumed that the  $\tau$ -th eigenvalue of the equilibrium point  $E_k$  is displayed as  $\lambda_{k,\tau}$  for  $\tau = 1,2,3,4$  and  $k = 0,1,2, \dots, 6$ .

(i) For  $E_0$ , the jacobian matrix evaluated in (18) is  $J(E_0) = \begin{pmatrix} \eta k_1 & 0 & 0 & 0 \\ 0 & \eta k_2 & 0 & 0 \\ 0 & 0 & \beta_B & 0 \\ 0 & 0 & 0 & -\alpha \end{pmatrix}$ .

Therefore, the eigenvalues are obtained as  $\lambda_{0,1} = \eta k_1$ ,  $\lambda_{0,2} = \eta k_2$ ,  $\lambda_{0,3} = \beta_B$  and  $\lambda_{0,4} = -\alpha$ . From Theorem 3.1,  $E_0$  is unstable point, since all of the eigenvalues have not lie in the left half of the complex plane due to (6).

In the same mind, the jacobian matrix for  $E_3$  is  $J(E_3) = \begin{pmatrix} -\eta k_1 & -\eta(k_1 + k_4) & -\eta & -\eta \left( \frac{E_{max}}{E_{50\mu}} + 1 \right) \\ 0 & \eta k_4 & 0 & \eta \\ 0 & 0 & \beta_B(1 - k_3) & 0 \\ 0 & 0 & 0 & -\alpha \end{pmatrix}$ , and so, the eigenvalues are

$\lambda_{3,1} = -\eta k_1$ ,  $\lambda_{3,2} = \eta k_4$ ,  $\lambda_{3,3} = \beta_B(1 - k_3)$  ve  $\lambda_{3,4} = -\alpha$ . All of these is not negative due to (6). From Theorem 3.1, it can be seen that  $E_3$  is unstable point.

(ii) Jacobian matrix evaluated at the equilibrium point  $E_1$  is  $J(E_1) = \begin{pmatrix} \eta(k_1 - 1) & 0 & 0 & 0 \\ 0 & \eta(k_2 - 1) & 0 & 0 \\ -k_3\beta_B & -k_3\beta_B & -\beta_B & 0 \\ 0 & 0 & 0 & -\alpha \end{pmatrix}$ . Therefore, eigenvalues are  $\lambda_{1,1} = \eta(k_1 - 1)$ ,

$\lambda_{1,2} = \eta(k_2 - 1)$ ,  $\lambda_{1,3} = -\beta_B$  and  $\lambda_{1,4} = -\alpha$ . By (6),  $\lambda_{1,3}$  and  $\lambda_{1,4}$  are negative. If  $k_1 < 1$  (already  $k_1 > k_2$  in (7)), then  $\lambda_{1,1}$  and  $\lambda_{1,2}$  are negative from (6). Considering Theorem 3.1, if  $k_1 < 1$ , then  $E_1$  is LAS.

(iii) Jacobian matrix in (18) for  $E_2$  is  $J(E_2) = \begin{pmatrix} -\eta k_4 & 0 & 0 & 0 \\ \eta(k_4 - k_2) & -\eta k_2 & -\eta & 0 \\ 0 & 0 & \beta_B(1 - k_3) & 0 \\ 0 & 0 & 0 & -\alpha \end{pmatrix}$ .

So, the eigenvalues are founded as  $\lambda_{2,1} = -\eta k_4$ ,  $\lambda_{2,2} = -\eta k_2$ ,  $\lambda_{2,3} = \beta_B(1 - k_3)$  and  $\lambda_{2,4} = -\alpha$ . Due to (6),  $\lambda_{2,1}, \lambda_{2,2}$  and  $\lambda_{2,4}$  are negative. Moreover, when  $1 < k_3$ ,  $\lambda_{2,3} < 0$  (already  $\beta_B > 0$  in (3) and  $\eta > 0$  in (6)). By Theorem 3.1, if  $1 < k_3$ , then  $E_2$  is LAS.

(iv) Let

$$k_3 < 1 < k_2 \text{ or } k_2 < 1 < k_3. \quad (19)$$

In this case,  $E_4$  is in  $\Omega$ . Evaluating  $E_4$  in  $J$ , we have

$$J(E_4) = \begin{pmatrix} \eta \frac{(1-k_3)(k_1-k_2)-k_4(k_2-1)}{(k_2-k_3)} & 0 & 0 & 0 \\ -\eta \frac{(k_2-k_4)(k_2-1)}{(k_2-k_3)} & -\eta \frac{k_2(k_2-1)}{(k_2-k_3)} & -\eta \frac{(k_2-1)}{(k_2-k_3)} & 0 \\ -\beta_B \frac{k_3 k_2 (1-k_3)}{(k_2-k_3)} & -\beta_B \frac{k_3 k_2 (1-k_3)}{(k_2-k_3)} & -\beta_B \frac{k_2(1-k_3)}{(k_2-k_3)} & 0 \\ 0 & 0 & 0 & -\alpha \end{pmatrix}. \quad (20)$$

That two eigenvalues obtained from (20) are  $\lambda_{4,1} = \eta \left( \frac{(1-k_3)(k_1-k_2)-k_4(k_2-1)}{(k_2-k_3)} \right)$  and  $\lambda_{4,2} = -\alpha$ . If

$$\frac{(1-k_3)(k_1-k_2)-k_4(k_2-1)}{(k_2-k_3)} < 0, \quad (21)$$

then  $\lambda_{4,1}$  is negative. Also,  $\lambda_{4,2}$  is negative by (3). The other eigenvalues are founded from the following matrix;

$$J^B(E_4) = \begin{pmatrix} -\eta \frac{k_2(k_2-1)}{(k_2-k_3)} & -\eta \frac{(k_2-1)}{(k_2-k_3)} \\ -\beta_B \frac{k_3 k_2 (1-k_3)}{(k_2-k_3)} & -\beta_B \frac{k_2(1-k_3)}{(k_2-k_3)} \end{pmatrix} \quad (22)$$

where  $J^B(E_4)$  is the block matrix of  $J(E_4)$ . Hence, characteristic equation of (22) is

$$\lambda^2 + \lambda \left( \eta(k_2 - 1) + \beta_B(1 - k_3) \right) \frac{k_2}{(k_2-k_3)} + \eta(k_2 - 1)\beta_B(1 - k_3) \frac{k_2}{(k_2-k_3)} = 0. \quad (23)$$

from (19), let

$$k_2 > 1 > k_3. \quad (24)$$

In case of (24), all of the roots of polynomial in (23) are negative or have negative real parts by Theorem 3.1 ( $n = 2$ ), that is,  $Re\{\lambda_{4,3}, \lambda_{4,4}\} < 0$ . Thus, if (21) and (24) are held, that is,  $1 < \frac{(1-k_3)(k_1-k_2)}{k_4} + 1 < k_2$ , then all of the eigenvalues evaluated at  $E_4$  are negative or have negative reel parts. In this respect, it is LAS.

(v) In analogy to (iv), if  $1 < k_1 < \frac{(1-k_3)(k_1-k_2)}{k_4} + 1$ , then  $E_5$  is LAS.

(vi) Lastly, when

$$k_2 < \frac{(1-k_3)(k_1-k_2)}{k_4} + 1 < \min \left\{ k_1, \frac{k_1-k_2}{k_4} + 1 \right\}. \quad (25)$$

$E_6$  is revealed in  $\Omega$ . That eigenvalues of jacobian matrix evaluated at  $E_6$  are  $\lambda_{6,1} = -\alpha, \lambda_{6,2}, \lambda_{6,3}$  and  $\lambda_{6,4}$ . The  $\lambda_{6,1}$  is negative due to (3). Also,  $\lambda_{6,2}, \lambda_{6,3}$  and  $\lambda_{6,4}$  are founded from following block matrix;

$$J^{B(E_6)} = \begin{pmatrix} -\eta k_1 \bar{s} & -\eta \bar{s}(k_1 + k_4) & -\eta \bar{s} \\ \bar{r}\eta(k_4 - k_2) & -\eta k_2 \bar{r} & -\eta \bar{r} \\ -k_3 \bar{b}\beta_B & -k_3 \bar{b}\beta_B & -\bar{b}\beta_B \end{pmatrix} \quad (26)$$

where

$$E_6 = (\bar{s}, \bar{r}, \bar{b}, \bar{a}) = \left( \frac{1}{k_4} - \frac{k_2 + \frac{k_3}{k_4}(k_1 - k_2)}{k_1 - k_2 + k_4}, \frac{k_1 + \frac{k_3}{k_4}(k_1 - k_2)}{k_1 - k_2 + k_4} - \frac{1}{k_4}, 1 - \frac{k_3(k_1 - k_2)}{k_1 - k_2 + k_4}, 0 \right), \quad (27)$$

$\bar{s}, \bar{r}, \bar{b} > 0$ .

Characteristic equation of (26) is obtained as follows:

$$\lambda^3 + P_1\lambda^2 + P_2\lambda + P_3 = 0 \quad (28)$$

where

$$\begin{aligned} P_1 &= (\eta(k_1\bar{s} + k_2\bar{r}) + \bar{b}\beta_B) \\ P_2 &= \eta \left( \eta \bar{s} \bar{r} k_4 (k_1 - k_2 + k_4) + \bar{b}\beta_B ((k_1\bar{s} + k_2\bar{r}) - k_3(\bar{s} + \bar{r})) \right) \\ P_3 &= \beta_B \bar{b} \eta^2 \bar{s} \bar{r} a_4 (k_1 - k_2 + k_4) \end{aligned} \quad (29)$$

In (29),

$$P_1 > 0 \quad (30)$$

due to (3), (6) and (27) and

$$P_3 > 0 \quad (31)$$

due to (3), (6), (7) and (27). In addition that, it is

$$P_1 P_2 - P_3 = \left( \frac{\eta(k_1\bar{s} + k_2\bar{r})}{\bar{b}\beta_B} \right) \left[ \frac{(k_1 - k_2 + k_4)k_4\bar{r}\eta\bar{s} +}{((k_1\bar{s} + k_2\bar{r}) - k_3(\bar{s} + \bar{r}))\bar{b}\beta_B} \right] - (k_1 - k_2 + k_4)k_4\eta\bar{s}\bar{r}\bar{b}\beta_B,$$

and so,

$$P_1 P_2 - P_3 = \eta(k_1\bar{s} + k_2\bar{r}) \left[ \frac{(k_1 - k_2 + k_4)k_4\bar{r}\eta\bar{s} +}{((k_1\bar{s} + k_2\bar{r}) - k_3(\bar{s} + \bar{r}))\bar{b}\beta_B} \right] + \left( \frac{(k_1\bar{s} + k_2\bar{r}) -}{k_3(\bar{s} + \bar{r})} \right) \bar{b}\beta_B \bar{b}\beta_B \eta \quad (32)$$

By (27), the expression  $(k_1\bar{s} + k_2\bar{r}) - k_3(\bar{s} + \bar{r})$  in (32) can be writing as

$$= k_1 \left( -\frac{k_2}{k_1 - k_2 + k_4} + \frac{1}{k_4} \bar{b} \right) + k_2 \left( \frac{k_1}{k_1 - k_2 + k_4} - \frac{1}{k_4} \bar{b} \right) - k_3 \frac{k_1 - k_2}{k_1 - k_2 + k_4}$$

$$= (k_1 - k_2) \left( \frac{1}{k_4} \bar{b} - k_3 \frac{1}{k_1 - k_2 + k_4} \right) = \frac{k_1 - k_2}{k_4} \left( \left( 1 - \frac{(k_1 - k_2)k_3}{k_1 - k_2 + k_4} \right) - \frac{k_3 k_4}{k_1 - k_2 + k_4} \right).$$

and so,

$$(k_1 \bar{s} + k_2 \bar{r}) - k_3 (\bar{s} + \bar{r}) = \frac{k_1 - k_2}{k_4} (1 - k_3) \quad (33)$$

(already  $k_1 > k_2$  due to (7)). If

$$k_3 < 1, \quad (34)$$

then  $(k_1 \bar{s} + k_2 \bar{r}) - k_3 (\bar{s} + \bar{r}) > 0$ , that is,

$$P_1 P_2 - P_3 > 0 \quad (35)$$

By considering (30), (31) and (35), if (25) and (34) are satisfied, then it is

$$Re\{\lambda_{6,2}, \lambda_{6,3}, \lambda_{6,4}\} < 0 \quad (36)$$

from Theorem 3.1 ( $n = 3$ ). In this respect, we have that  $E_6$  is LAS.

In table 2, proposition 3.2 are summarized.

Table 2. The LAS conditions of the equilibria of system (5).

Equilibrium Points	LAS Conditions
$E_1 = (0,0,1,0)$	$k_1, k_2 < 1$
$E_2 = (0,1,0,0)$	$1 < k_3$
$E_4 = \left( 0, \frac{(k_2 - 1)}{(k_2 - k_3)}, \frac{k_2(1 - k_3)}{(k_2 - k_3)}, 0 \right)$	$1 < \frac{(1 - k_3)(k_1 - k_2)}{k_4} + 1 < k_2 (< k_1)$
$E_5 = \left( \frac{(k_1 - 1)}{(k_1 - k_3)}, 0, \frac{k_1(1 - k_3)}{(k_1 - k_3)}, 0 \right)$	$1 < k_1 < \frac{(1 - k_3)(k_1 - k_2)}{k_4} + 1$
$E_6 = \left( \frac{1}{k_4} - \frac{k_2 + \frac{k_3}{k_4}(k_1 - k_2)}{k_1 - k_2 + k_4}, \frac{k_1 + \frac{k_3}{k_4}(k_1 - k_2)}{k_1 - k_2 + k_4} - \frac{1}{k_4}, 1 - k_3 \left( \frac{k_1 - k_2}{k_1 - k_2 + k_4} \right), 0 \right)$	$k_3 < 1$ and $k_2 < \frac{(1 - k_3)(k_1 - k_2)}{k_4} + 1 < \min \left\{ k_1, \frac{k_1 - k_2}{k_4} + 1 \right\}$

### 3.3. The Analysis of Globally Asymptotically Stability of Equilibrium Points

In here, it has been focused on globally asymptotically stability (GAS) of equilibrium points in Table 2. Let

$$k_1 < 1 < k_3 \tag{37}$$

(already  $k_2 < k_1$  in (7)). When inequality (37) is satisfied, it is clear that the equilibrium points  $E_1 = (0,0,1,0)$  and  $E_2 = (0,1,0,0)$  are LAS in the same sub-region of  $\Omega$ . Description of this case is shown in Fig.2. For the variables  $s = a = 0$  and the parameters  $\beta_B = \eta = 1$ ,  $k_3 = 2$   $k_2 = \frac{1}{3} < k_1 = 1/2$  in the system (5), Fig.2 is plotted via the program pplane.jar. In here, the points (0,1) and (1,0) in plane represent the equilibrium points  $E_1$  and  $E_2$  respectively. Therefore, they are LAS.

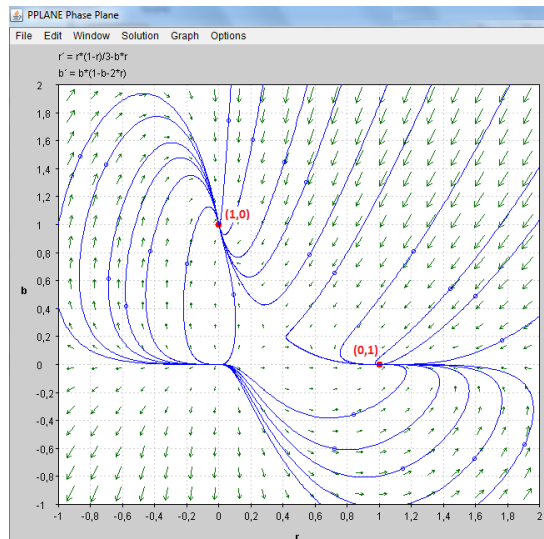


Fig.2. In case of  $s = a = 0$ ,  $\beta_B = \eta = 1$ ,  $k_3 = 2$   $k_2 = \frac{1}{3} < k_1 = 1/2$  in system (5), The LAS of the equilibrium points  $E_1$  and  $E_2$ .

Except for this inequality is held, there is no same sub-region of  $\Omega$  where at least two of the equilibrium points  $E_1, E_2, E_4, E_5$  and  $E_6$  are LAS. In this section, it has been assumed that inequality (37) is not provided because of this reason.

**Proposition 3.3.** Let us denote by  $\Gamma_i$  the LAS region of the equilibrium point  $E_i$  in  $\Omega$  for  $i = 1,2,4,5,6$ . Then  $\Gamma_i \cap \Gamma_j = \emptyset$  for  $i \neq j$  and  $j = 1,2,4,5,6$ .

**Proof:** This situation is evidently in Table 2.

**Proposition 3.4.** It is assumed that  $E_1$  is LAS. In this case, it is GAS. Similarly, if  $E_2$  is LAS, then it is GAS.

**Proof:** In the system (5), each variable in absence of the others has logistic form. Therefore, the GAS analysis of the equilibrium points  $E_1$  and  $E_2$  can be examined in a similar manner to each other.

For  $E_1$ , it is investigated as the following. Let us consider the region  $\Omega_1 = \{b \in R: 0 \leq b \leq 1\}$  given by

$$\frac{db}{dt} = \beta_B b(1 - b), \quad (38)$$

where  $\beta_B > 0$  is the intrinsic growth rate of immune cells and  $\bar{b} = 1$  is the carrying capacity of immune cells. There are two equilibria  $\bar{b} = 0, 1$ . If (38) is solved by separation of its variables, then it is obtained that  $b(t) = \frac{b(0)}{b(0) + (1 - b(0))e^{-\beta_B t}}$ . It can be seen  $\lim_{t \rightarrow \infty} b(t) = 1$ .

Thus,  $\bar{b} = 1$  (namely,  $E_1$ ) is GAS.

**Proposition 3.5.** It is assumed that  $E_4$  is LAS. Then it is GAS. Similarly, if  $E_5$  is LAS, then it is GAS.

**Proof:** Since  $E_4$  and  $E_5$  are present in  $R^2$ , we have benefited from Bendixon-Dulac criteria for analysis of GAS.

Firstly, let us examine the  $E_4$  in the region  $\Omega_2 = \{(r, b) \in R^2: 0 < r < 1, 0 < b < 1\}$ . Moreover, let  $H(r, b) = \frac{1}{rb}$ . It is obviously  $H(r, b) > 0$  and functions  $F_1(r, b)$  and  $F_2(r, b)$  obtained from system (5) are denote as

$$\begin{aligned} F_1(r, b) &= \eta r(k_2(1 - r) - b) \\ F_2(r, b) &= \beta_B b((1 - b) - k_3 r). \end{aligned} \quad (39)$$

Considering  $H(r, b)$ , divergence obtained from these functions in (39) is founded as

$$\begin{aligned} \Delta(r, b) &= \frac{\partial}{\partial r}(F_1 H) + \frac{\partial}{\partial b}(F_2 H) = \frac{\partial}{\partial r} \left( \eta r(k_2(1 - r) - b) \frac{1}{rb} \right) + \frac{\partial}{\partial b} \left( \beta_B b((1 - b) - k_3 r) \frac{1}{rb} \right) \\ &= \frac{\partial}{\partial r} \left( \eta \frac{(k_2(1 - r) - b)}{b} \right) + \frac{\partial}{\partial b} \left( \beta_B \frac{((1 - b) - k_3 r)}{r} \right), \end{aligned}$$

and so,

$$\Delta(r, b) = - \left( \eta \frac{k_2}{b} + \beta_B \frac{1}{r} \right). \quad (40)$$

From (3), (6) and (8), the  $\Delta(r, b)$  in (40) is negative. In this respect, by the Bendixon-Dulac criteria, there is not periodic orbit in the  $r - b$  plane. Because  $E_4$  is LAS in the above plane (namely  $\Omega_2$  and so,  $\Omega$ ), it is GAS. In the same way, it can be seen that  $E_5$  is GAS.

**Definition 3.1.** (LaSalle's extension of the direct method of Lyapunov): The system is of the form

$$\frac{dx_i}{dt} = \dot{x}_i = x_i F_i(x_1, x_2, \dots, x_n), \quad i = 1, 2, \dots, n \quad (41)$$

where  $x_i$  is the density of the  $i - th$  species in the community at time  $t$ . Each  $F_i$  is a continuous function from  $R_+^n$ , the nonnegative cone in  $R^n$ , to  $R$  and is sufficiently smooth to

guarantee that initial value problems associated with (41) have unique solutions in the population orthant,  $R_+^n$ .

Thus, the positive steady-state  $x^*$  of (41) is a globally asymptotically stable, if  $F(x) > 0$  for all  $x \in (0, x^*)$  and  $F(x) < 0$  for all  $x \in (x^*, \infty)$  [22].

Let us consider as  $F_i(x_1, x_2, \dots, x_n) = q_i + \sum_{k=1}^n w_{ik}x_k$ ,  $i = 1, 2, \dots, n$ .

here  $q_i, -w_{ii}$  are positive constants and  $w_{ik}, i \neq k$  are constants with any sign. If we define  $w_{ik}$  and  $q = (q_1, q_2, \dots, q_n)$ , then it can be shown that  $x^* = -W^{-1}q^t$  is a steady-state of system. Let us suppose that  $x^* \in R_+^n$  is positive and  $C = \text{diag}(c_1, c_2, \dots, c_n)$ . Function  $V(x) = \sum_{i=1}^n c_i \left( x_i - x_i^* - x_i^* \ln \frac{x_i}{x_i^*} \right)$  can be used as a Lyapunov function. Clearly,  $V(x)$  satisfied the conditions  $V(x^*) = 0$ ,  $V(x) > 0$  for all  $x \in R_+^n$ ,  $x \neq x^*$ ,  $V(x) \rightarrow \infty$  as  $x \rightarrow \infty$  and  $x \rightarrow 0$ . We have

$$\begin{aligned} \dot{V}(x) &= \sum_{i=1}^n c_i (x_i - x_i^*) \left( q_i + \sum_{k=1}^n w_{ik} x_k \right) = \sum_{i=1}^n c_i (x_i - x_i^*) \left( \sum_{k=1}^n w_{ik} (x_k - x_k^*) \right) \\ &= \frac{1}{2} (x - x^*)^t (CW + W^t C) (x - x^*). \end{aligned}$$

From LaSalle's extension of the direct method of Lyapunov, we have the following

**Theorem 3.2.** The steady-state  $x^*$  of (41) is GAS, if there exists a positive diagonal matrix  $C$  such that  $CW + W^t C$  is a negative semidefinite and the function

$$\dot{V}(x) = \frac{1}{2} (x - x^*)^t (CW + W^t C) (x - x^*)$$

does not vanish identically along a nontrivial solution [21,22].

**Proposition 3.6.** Let  $E_6$  is LAS. If  $0 < 4(k_1 + k_4)(k_2 - k_4) < k_1 k_2$ ,  $4k_3 < k_2$ , then it is GAS.

**Proof:** When the last equation of system (5) are separated, their solutions approach to  $\bar{a} = 0$ . Replacing this value in the first three equations of system (5), we have attained that the asymptotically equivalent system in the region

$$\Omega_3 = \{(s, r, b) \in R^3: 0 < s < 1, 0 < r < 1, 0 < s + r < 1, 0 < b < 1\}. \quad (42)$$

given by

$$\begin{aligned}\frac{ds}{dt} &= s(k_1\eta - k_1\eta s - (k_1 + k_4)\eta r - \eta b) \\ \frac{dr}{dt} &= r(k_2\eta - (k_2\eta - k_4\eta)s - k_2\eta r - \eta b) \\ \frac{db}{dt} &= b(\beta_B - k_3\beta_B s - k_3\beta_B r - \beta_B b).\end{aligned}\tag{43}$$

By Definition 3.1, we have presumed that the Lyapunov function of system (43) defined in the region (42) is

$$V(x) = \sum_{i=1}^3 c_i \left( x_i - x_i^* - x_i^* \ln \frac{x_i}{x_i^*} \right)\tag{44}$$

where each  $x_i^*$  for  $i = 1,2,3$  are component at equilibrium point. Derivative of  $V(x)$  in (44) is

$$\dot{V}(x) = \sum_{i=1}^3 c_i (x_i - x_i^*) (q_i + \sum_{k=1}^3 w_{ik} x_k),\tag{45}$$

By Theorem 3.2, (45) can be writing as following

$$\dot{V}(x) = \frac{1}{2} (x - x^*)^t (CW + W^t C) (x - x^*)\tag{46}$$

where

$$\begin{aligned}x &= \begin{pmatrix} s \\ r \\ b \end{pmatrix}, x^* = \begin{pmatrix} \bar{s} \\ \bar{r} \\ \bar{b} \end{pmatrix}, q = (k_1\eta \quad k_2\eta \quad \beta_B), C = \begin{pmatrix} c_1 & 0 & 0 \\ 0 & c_2 & 0 \\ 0 & 0 & c_3 \end{pmatrix} \\ W &= \begin{pmatrix} w_{11} & w_{12} & w_{13} \\ w_{21} & w_{22} & w_{23} \\ w_{31} & w_{32} & w_{33} \end{pmatrix} = - \begin{pmatrix} k_1\eta & \eta(k_1 + k_4) & \eta \\ \eta(k_2 - k_4) & k_2\eta & \eta \\ k_3\beta_B & k_3\beta_B & \beta_B \end{pmatrix},\end{aligned}\tag{47}$$

In addition that,  $q_{1i}, -w_{ii}$  for  $i, k = 1,2,3$  are positive constants,  $w_{ik}$  for  $i \neq k$  are constants with any sign and  $C$  is a positive diagonal matrix and  $\bar{s}, \bar{r}$  and  $\bar{b}$  are in (23). Moreover,

$$\begin{pmatrix} \bar{s} \\ \bar{r} \\ \bar{b} \end{pmatrix} = x^* = -W^{-1}q^t \text{ such that } \det W \neq 0.$$

By (47), it is obtained that

$$CW + W^t C = - \begin{pmatrix} 2c_1 k_1 \eta & (c_1 + c_2)\eta(k_1 + k_4) & (c_1\eta + c_3 k_3 \beta_B) \\ \eta(c_2(k_2 - k_4) + c_1(k_1 + k_4)) & 2c_2 k_2 \eta & (c_2\eta + c_3 k_3 \beta_B) \\ (c_1\eta + c_3 k_3 \beta_B) & (c_2\eta + c_3 k_3 \beta_B) & 2c_3 \beta_B \end{pmatrix}. \quad (48)$$

If

$$k_2 > k_4, \quad (49)$$

then the matrix  $CW + W^t C$  in (48) is negative-definite.

Moreover, the function  $\dot{V}(x)$  in (46) is

$$\begin{aligned} \dot{V}(x) = & c_1 w_{11} (x_1 - x_1^*)^2 + (c_1 w_{12} + c_2 w_{21})(x_1 - x_1^*)(x_2 - x_2^*) \\ & + c_2 w_{22} (x_2 - x_2^*)^2 + (c_1 w_{13} + c_3 w_{31})(x_1 - x_1^*)(x_3 - x_3^*) \\ & + (c_2 w_{23} + c_3 w_{32})(x_2 - x_2^*)(x_3 - x_3^*) + c_3 w_{33} (x_3 - x_3^*)^2. \end{aligned} \quad (50)$$

(50) can be more clearly written as following

$$\begin{aligned} \dot{V}(x) = & \left[ \frac{1}{2} c_1 w_{11} (x_1 - x_1^*)^2 + (c_1 w_{12} + c_2 w_{21})(x_1 - x_1^*)(x_2 - x_2^*) + \frac{1}{2} c_2 w_{22} (x_2 - x_2^*)^2 \right] \\ & + \left[ \frac{1}{2} c_2 w_{22} (x_2 - x_2^*)^2 + (c_2 w_{23} + c_3 w_{32})(x_2 - x_2^*)(x_3 - x_3^*) + \frac{1}{2} c_3 w_{33} (x_3 - x_3^*)^2 \right] \\ & + \left[ \frac{1}{2} c_1 w_{11} (x_1 - x_1^*)^2 + (c_1 w_{13} + c_3 w_{31})(x_1 - x_1^*)(x_3 - x_3^*) + \frac{1}{2} c_3 w_{33} (x_3 - x_3^*)^2 \right]. \end{aligned} \quad (51)$$

In this sense, (51) does not vanish identically along a nontrivial solution, if the following conditions are met;

$$\begin{aligned} \Delta_1 &= (c_1 w_{12} + c_2 w_{21})^2 - c_1 c_2 w_{11} w_{22} < 0 \\ \Delta_2 &= (c_2 w_{23} + c_3 w_{32})^2 - c_2 c_3 w_{22} w_{33} < 0 \\ \Delta_3 &= (c_1 w_{13} + c_3 w_{31})^2 - c_1 c_3 w_{11} w_{33} < 0 \end{aligned} \quad (52)$$

where  $\Delta_1, \Delta_2$  and  $\Delta_3$  are the discriminant during each of the statement (51). If the elements of a positive diagonal matrix  $C$  are selected, for example, as follows

$$\begin{aligned} c_2 &= \frac{w_{11} w_{22} - 2w_{12} w_{21}}{2w_{21}^2} c_1, \quad c_3 = \frac{w_{22} w_{33} - 2w_{23} w_{32}}{2w_{32}^2} c_2, \\ c_1 &= \frac{w_{11} w_{33} - 2w_{31} w_{13}}{2w_{13}^2} c_3, \quad c_3 > 0, \end{aligned} \quad (53)$$

then it can be seen that inequalities in (52) have provided. From (52) and (53), we have

$$\begin{aligned}\Delta_1 &= 4w_{12}w_{21} - w_{11}w_{22} < 0 \\ \Delta_2 &= 4w_{23}w_{32} - w_{22}w_{33} < 0 \\ \Delta_3 &= 4w_{31}w_{13} - w_{11}w_{33} < 0.\end{aligned}\tag{54}$$

After the elements of the  $W$  matrix in (47) have written its places in (54), we have the following conditions:

$$4(k_1 + k_4)(k_2 - k_4) < k_1k_2, 4k_3 < k_2.\tag{55}$$

Therefore, if inequalities (55) is satisfied, the function  $\dot{V}(x)$  does not vanish identically along a nontrivial solution. By (49) and (55), if

$$0 < 4(k_1 + k_4)(k_2 - k_4) < k_1k_2, 4k_3 < k_2,\tag{56}$$

then  $E_6$  is GAS.

In the following discussion, we have demonstrated some of the contributions our mathematical modelling to the study of complex problems in host-microbe interactions.

#### 4. Numerical study

In our numerical study, the datas of different species of bacteria including *Staphylococcus aureus*, *Mycobacterium tuberculosis*, *Acinetobacter baumannii* and *E. coli* in host have used. In this sense, each bacterial species has been evaluated separately in the model. By this study, dynamics of interactions among size of the bacteria population, concentration of the antibiotic and immune cells in host have examined. The parameter values used for numerical studies are given in the following Table 3.

Table 3. Interpretation and considered values of the parameters used in (1). Data are deduced from the literature (references).

Parameter	Description	Unit	Value <sup>1</sup>	Reference <sup>1</sup>	Value <sup>2</sup>	Reference <sup>2</sup>	Value <sup>3</sup>	Reference <sup>3</sup>	Value <sup>4</sup>	Reference <sup>4</sup>
$\beta_S$	Growth rate of susceptible bacteria	days <sup>-1</sup>	24	[23]	0.8	[1]	1.2	[24]	0.6	[25]
$\beta_R$	Growth rate of resistant bacteria	days <sup>-1</sup>	21.6	[26]	0.5	[1]	0.9	Hypothesis	0.4	Hypothesis
$\beta_B$	Growth rate of immune cells	days <sup>-1</sup>	3	[26]	0.6	[27]	0.6	[27]	0.6	[27]
$\bar{\eta}$	Rate of bacteria destroyed by immune cells	cells <sup>-1</sup> days <sup>-1</sup>	$2.4 \cdot 10^{-4}$	[28]	$10^{-6}$	Hypothesis	$10^{-6}$	Hypothesis	$10^{-6}$	Hypothesis
$\Lambda$	Carrying capacity of immune cells	cells	$1.8 \cdot 10^5$	[28]	$1.8 \cdot 10^5$	[28]	$10^6$	[16]	$10^6$	[16]
$T$	Carrying capacity of bacteria	cells	$10^9$	[23]	$10^9$	[29]	$10^8$	[30]	$10^7$	[31]
$\alpha$	Elimination rate of antibiotic under distinct doses days	days <sup>-1</sup>	3.6	[23]	3.6	[23]	3.6	[23]	3.6	[23]
$\mu$	Mutation rate of susceptible bacteria due antibiotic	days <sup>-1</sup>	$9.8 \cdot 10^{-5}$	[30]	$5.1 \cdot 10^{-9}$	[32]	$9 \cdot 10^{-6}$	Hypothesis	$9.3 \cdot 10^{-6}$	[33]
$\lambda$	Bacterial induced death of immune cells	cells <sup>-1</sup> days <sup>-1</sup>	$6 \cdot 10^{-6}$	[28]	$6 \cdot 10^{-6}$	[28]	$6 \cdot 10^{-6}$	[28]	$6 \cdot 10^{-6}$	[28]
$\sigma$	Conjugation rate constant	days <sup>-1</sup>	$10^{-5}$	[26]	$10^{-7}$	Hypothesis	$10^{-7}$	Hypothesis	$10^{-4}$	Hypothesis
$E_{max}$	Maximum killing rate of susceptible bacteria	days <sup>-1</sup>	36	[23]	36	[23]	36	[23]	36	[23]
$E_{50}$	Antibiotic concentration for half maximum effect on susceptible bacteria	µg/ml	0.25	[23]	0.25	[23]	0.25	[23]	0.25	[23]

To some specific diseases causing of Staphylococcus aureus, Mycobacterium tuberculosis, Acinetobacter baumannii and E. coli, respectively, values of parameters used in the system (2) is obtained from the literature. Antibiotic used is Ciprofloxacin. In addition that, it has showed by <sup>1</sup>, values and references for Staphylococcus aureus, by <sup>2</sup>, values and references for Mycobacterium tuberculosis, by <sup>3</sup>, values and references for Acinetobacter baumannii and by <sup>4</sup>, values and references for E. coli.

Taking into consideration values of the parameters in Table 3, qualitative analysis of the system (5) are supported by numerical simulations. Moreover, it has obtained the following figures in compliance with the results founded in Table 2.

The antibiotic concentration for equilibria of the system (5) is eliminated completely from the body after a while. This circumstance is biological meaning with respect to the antibiotic excreted from body, and it can be seen in Table 2 and in these figures obtained from different positive initial conditions.

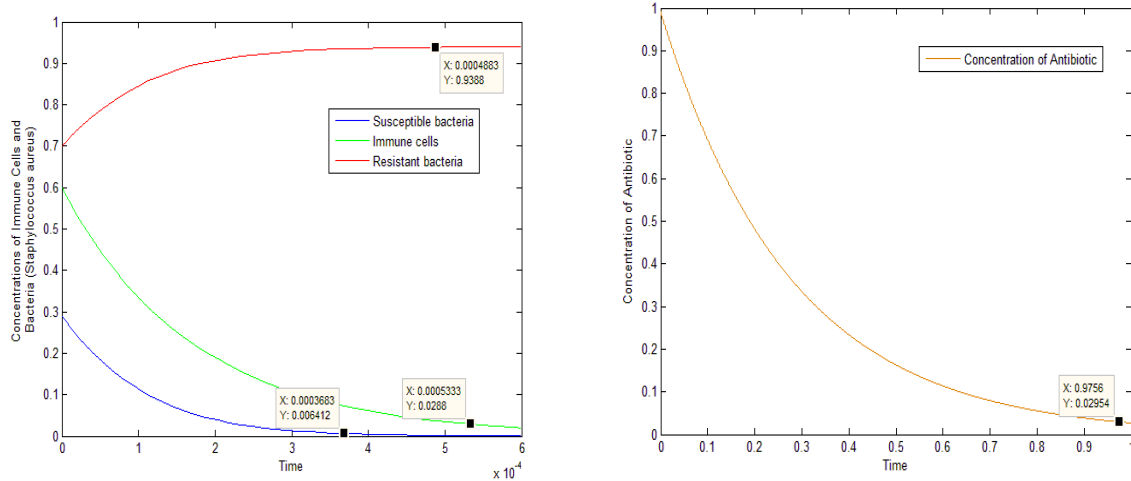


Fig.3. In case of  $1 < k_3 = 2000$ , Temporal course of bacteria population, immune cells and antibiotic by using the parameter values given in Table 3 for the Staphylococcus aureus.

In the Fig.3, it is founded the results relating to stability of  $E_2(0,1,0,0)$  for Staphylococcus aureus. Also, it has observed that other variables except for resistant bacteria have eliminated completely from the body after a while. In here antibiotic concentration has excreted in one day. Within about one week, the resistant bacteria reaches a positive equilibrium point, that is, its carrying capacity, and susceptible bacteria and immune cells are removed completely from the body. In this sense, immune cells do not respond resistant bacteria to antibiotic.

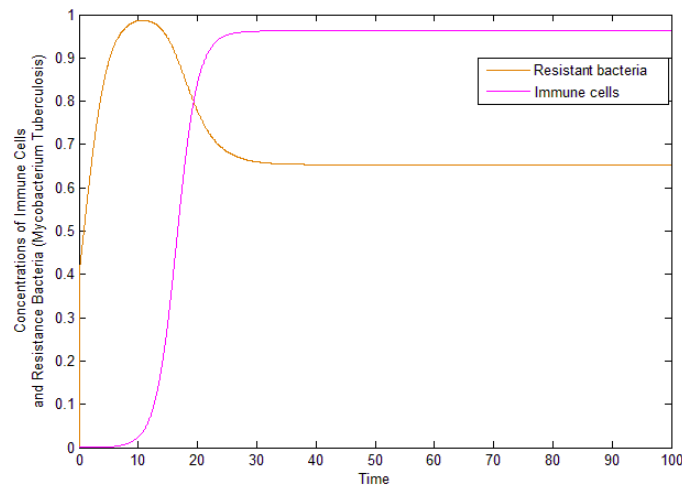


Fig.4. In case of  $1 < \frac{(1-k_3)(k_1-k_2)}{k_4} + 1 = 1.02829 < k_2 = 2.7778$ , Temporal course of bacteria population by using the parameter values given in Table 3 for the Mycobacterium tuberculosis.

Stability of the equilibrium point  $E_4 = (0,0.6534,0.9627,0)$  for Mycobacterium tuberculosis is observed in the Fig.4. Also, while the susceptible bacteria is eliminated, resistant bacteria to antibiotic and immune cells are persist in host. In this Figure, it is seen that the

concentration of the antibiotic and susceptible bacteria have excreted from the body within one day and resistant bacteria and immune cells reach to their positive equilibrium values within 25 days.

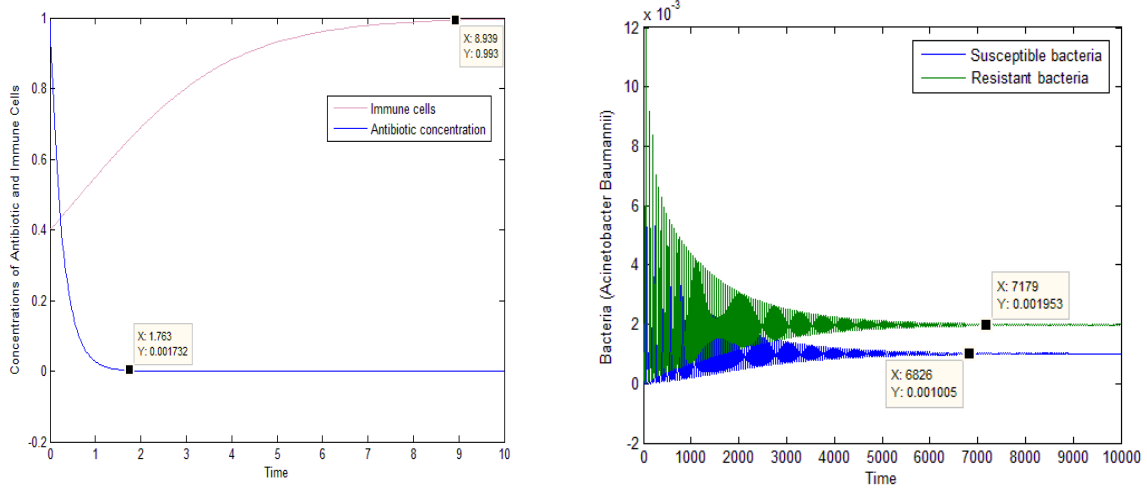


Fig.5. In case of  $k_3 = 0.57 < 1$  and  $k_2 = 0.9 < \frac{(1-k_3)(k_1-k_2)}{k_4} + 1 = 1,00129 < \min \left\{ k_1 = 1.2, \frac{k_1-k_2}{k_4} + 1 = 1.003 \right\}$ , Temporal course of bacteria population, immune cells and antibiotics by using the parameter values given in Table 3 for the *Acinetobacter baumannii*.

In the Fig.5, it has used that the datas obtained for *Acinetobacter baumannii* and we have observed that stability of  $E_6 = (0.001009870389, 0.00198115653, 0.998295114656, 0)$  which the sub-populations of susceptible and resistant bacteria to antibiotic and immune cells persist. In this respect, the antibiotic concentration excreted within 2 days and immune cells reaches a positive equilibria within ten days. Therefore, susceptible and resistant bacteria to antibiotic reach to their a very small positive equilibrium values after a long time under the specific level of immune system cells.

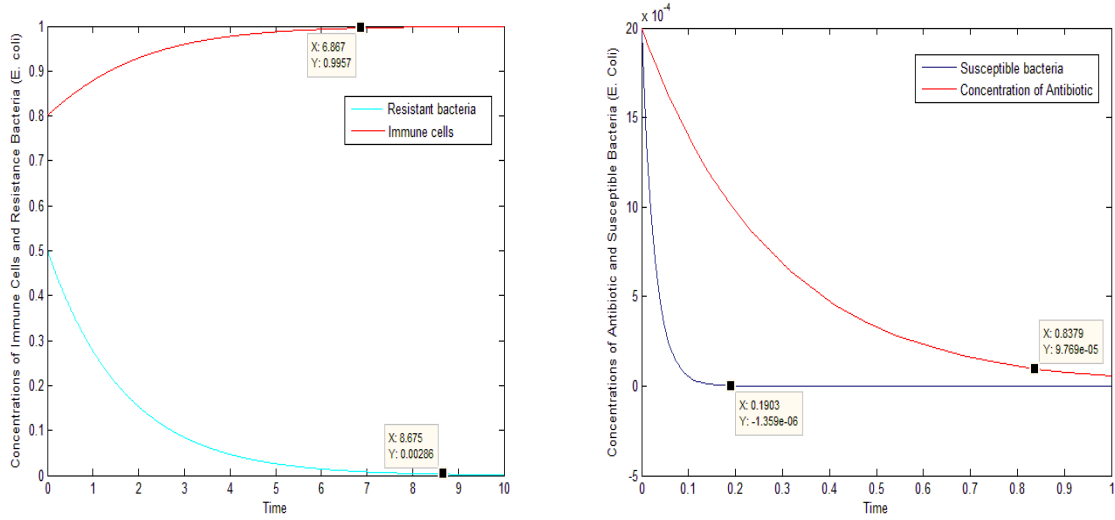


Fig.6. In case of  $k_1 = 0.6 < 1$ , Temporal course of bacteria population, immune cells and antibiotics by using the parameter values given in Table 3 for the E. coli.

Finally, the results relating to stability of  $E_1 = (0,0,1,0)$  have shown in the Fig.6. by using the datas for E. coli. In this sense, antibiotic concentration and susceptible bacteria have eliminated within 24 hours. In 7-10 days, the resistant bacteria has disappeared and the immune cells has reached to it's carrying capacity.

In this study, the effects of antibiotics and immune system cells in case of bacterial infection have been assessed in certain intervals of time.

## 5. Results and Discussions

In this study, the values  $k_1$ ,  $k_2$ ,  $k_3$  and  $k_4$  have stated the conditions identifying the changes in the population sizes of the infectious bacteria, hosts immune cells and antibiotic. With regards to the biological meaning of the parameters describing these statements, the parameter  $k_1$  can be comment as the number of bacteria generated by the fraction of susceptible bacteria surviving under pressure of immune cells independently from both the effect of antibiotic and the conjugation including the transfer of genes between susceptible and resistant bacteria. Analogously,  $k_2$  represents the bacteria generated by resistant bacteria surviving under pressure of immune cells. The parameter  $\frac{1}{k_3}$  can be expressed as the number of cells generated by the fraction of immune cells surviving under pressure of bacteria. Moreover, taking into consideration  $\frac{k_1}{k_4+1} = \frac{\beta_S}{\sigma T + \eta \Lambda}$  in (6), the parameter  $\frac{k_1}{k_4+1}$  can be comment as the number of bacteria generated by the fraction of susceptible bacteria surviving under both the pressure of immune cells and the conjugation including the transfer of genes between susceptible and resistant bacteria independently from the effect of antibiotic. Hence, the biological existence and stability conditions of the equilibria of system (5) obtained from Table 2 have independent from the effect of antibiotic.

Let us held not the inequality (37). In case of  $\frac{1}{k_3} < 1$ , the state expressed only the existence of resistant bacteria independently from the status of all other variables is revealed. When  $1 <$

$\frac{1}{\kappa_3}$ , the status of the other equilibrium point is taken into account. In this sense, the effect of the immune response of the host is very important in terms of the development of the infection.

## References

- [1] Mondragón, E.I., Mosquera, S., Cerón, M., Burbano-Rosero, E.M., Hidalgo-Bonilla, S.P., Esteva, L., P.R-L Jhoana, Mathematical modeling on bacterial resistance to multiple antibiotics caused by spontaneous mutations, *BioSystems*, 117, 60–67, 2014.
- [2] Daşbaşı, B. and Öztürk, İ., Mathematical modelling of bacterial resistance to multiple antibiotics and immune system response, *SpringerPlus*, 5, 1-17, 2016.
- [3] Mahmoud, A. G. and Rice, L. B., Antifungal agents: mode of action, mechanisms of resistance, and correlation of these mechanisms with bacterial resistance, and correlation, *Clin. Microbiol. Rev.*, 12(4), 501–517, 1999.
- [4] Murray, J.D., *Mathematical Biology. I. An introduction*, Springer-Verlag, 3rd Edition, 2002.
- [5] Murray, J.D., *Mathematical Biology. II: Spatial Models and Biomedical Applications*, Springer-Verlag, 3rd Edition, 2003.
- [6] Daşbaşı, B., The Fractional-Order mathematical modeling of bacterial resistance against multiple antibiotics in case of local bacterial infection, *Sakarya University Journal of Science*, 251, 1-13, 2017.
- [7] Alberts, B., Johnson, A., Lewis, J., Raff, M., Roberts, K. and Walter, P.P., *Molecular Biology of the Cell. The Adaptive Immune System*, Garland Science, 4th Edition, 2002.
- [8] Hethcote, H.W., The mathematics of infectious diseases, *SIAM Rev.*, 42, 599-653, 2000.
- [9] Austin, D., Kakehashi, M. and Anderson, R.M., The transmission dynamics of antibiotic-resistant bacteria: The relationship between resistance in commensal organisms and antibiotic consumption, *Proc. R. Soc. Lond. [Biol.]*, 264, 1629–1638, 1997.
- [10] Bonten, M., Austin, J. and Lipsitch, M., Understanding the spread of antibiotic resistant pathogens in hospitals, mathematical models as tools for control, *Clin. Infect. Dis*, 33, 1739-1746, 2001.
- [11] Austin, D. and Anderson, R., Studies of antibiotic resistance within the patient, hospitals and the community using simple mathematical models, *Philos. Trans. R. Soc. Lond. [Biol.]*, 354, 721–738, 1999.
- [12] Imran, M. and Smith, H., The pharmaco dynamics of antibiotic treatment, *Comput. Math. Method Med.*, 7, 229–263, 2006.
- [13] Alanis, A., Resistance to antibiotics: are we in the post-antibiotic era?, *Arch. Med. Res.*,

- 36, 697-705, 2005.
- [14] Tenover, F., Mechanisms of antimicrobial resistance in bacteria, *Am. J. Med.*, 119, 3–10, 2006.
- [15] Bergstrom, C., Lipsitch, M. and Levin, B., Natural selection, infectious transfer and the existence conditions for bacterial plasmids, *Genetics*, 155, 1505–1519, 2000.
- [16] D'Agata, E., Dupont-Rouzeyrol, M., Magal, P., Olivier, D. and Ruan, S., The impact of different antibiotic regimens on the emergence of antimicrobial-resistant bacteria, *PLoSone*, 3, 1-9, 2008.
- [17] Imran, M. and Smith, H., The dynamics of bacterial infection, innate immune response, and antibiotic treatment, *Discrete Contin. Dyn. Syst. B*, 8, 127–147, 2007.
- [18] Whitman, A. and Ashrafiuon, H., Asymptotic theory of an infectious disease model, *J. Math. Biol.*, 53, 287-304, 2006.
- [19] Lipsitch, M. and Levin, B., The population dynamics of antimicrobial chemotherapy, *Antimicrob. Agents Ch.*, 41, 363–373, 1997.
- [20] Nikolaou, M. and Tam, V., A new modeling approach to the effect of antimicrobial agents on heterogeneous microbial populations, *J. Math. Biol.*, 52, 154–182, 2006.
- [21] Allen, L.J.S., An Introduction to Mathematical Biology, London: Pearson Education, 2007.
- [22] Hale, J. and Koçak, H., Dynamics and Bifurcations, New York: Springer-Verlag, 1991.
- [23] Handel, A., Margolis, E. and Levin, B., Exploring the role of the immune response in preventing antibiotic resistance, *J.Theor.Biol.*, 256, 655–662, 2009.
- [24] Antunes, L.C.S., Imperi, F., Carattoli, A. and Visca, P., Deciphering the Multifactorial Nature of *Acinetobacter baumannii* Pathogenicity, *PLoSone*, 6, 2011.
- [25] Freter, R., Freter, R.R. and Brickner, H., Experimental and mathematical models of *Escherichia coli* plasmid transfer in vitro and in vivo, *Infect. Immun.*, 39, 60-84, 1985.
- [26] Ternent, L., Dyson, R.J., Krachler, A.M. and Jabbari, S., Bacterial fitness shapes the population dynamics of antibiotic resistant and susceptible bacteria in a model, *J. Theor. Biol.*, 372, 1-11, 2014.
- [27] Pugliese, A. and Gandolfi, A., A simple model of pathogen–immune dynamics including specific and non-specific immunity, *Math. Biosci.*, 214, 73–80, 2008.
- [28] Smith, A., McCullers, J. and Adler, F., Mathematical model of a three-stage innate immune response to a pneumococcal lung infection, *J. Theor. Biol.*, 276, 106–116, 2011.
- [29] Alavez, J., Avenda, R., Esteva, L., Fuentes, J., Garcia, G. and Gómez, G., Within-host population dynamics of antibiotic-resistant *M. Tuberculosis*, *Math. Med. Biol.*, 24, 35-56,

2006.

- [30] Campion, J.J., McNamara, P.J. and Evans, M.E., Evolution of Ciprofloxacin-Resistant *Staphylococcus aureus* in In Vitro, *Antimicrob. Agents Ch.*, 48, 4733–4744, 2004.
- [31] Carruthers, M. D., Nicholson, P. A., Tracy, E. N. and Munson, R. S., *Acinetobacter baumannii* Utilizes a Type VI Secretion System for Bacterial Competition, *PLoSone*, 8, 1-8, 2013.
- [32] McGrath, M., Pittius, N. C., Helden, P.D., Warren, R.M. and Warner, D.F., Mutation rate and the emergence of drug resistance in *Mycobacterium tuberculosis*, *J. Antimicrob. Chemoth.*, 69, 292-302, 2014.
- [33] Ryan, C.T. and Romesberg, F.E., Induction and Inhibition of Ciprofloxacin Resistance-Confering Mutations in Hypermutator Bacteria, *Antimicrob. Agents Ch.*, 50, 220–225, 2006.

## Thermo-Structural Analysis of First Stage Gas Turbine Rotor Blade Materials for Optimum Service Performance

Aniekan Ikpe E.<sup>a\*</sup>, Oghenefejiro Efe-Ononeme E.<sup>b</sup>, Godfrey Ariavie O.<sup>c</sup>

<sup>a\*,b,c</sup> Institution Department of Mechanical Engineering, Faculty of Engineering, University of Benin, P.M.B. 1154, Nigeria

E-mail address: [ikpeaniekan@gmail.com](mailto:ikpeaniekan@gmail.com)<sup>a\*</sup>, [engrijji@gmail.com](mailto:engrijji@gmail.com)<sup>b</sup>, [ariaviefe@uniben.edu](mailto:ariaviefe@uniben.edu)<sup>c</sup>

ORCID numbers of authors:

0000-0001-9069-9676<sup>a</sup>, 0000-0003-0893-0600<sup>b</sup>, 0000-0002-9614-5962<sup>c</sup>

Received date: 25.07.2018

Accepted date: 10.08.2018

### Abstract

During gas turbine operation, the vibration that occurs at high speed, hot gases entering the combustion chamber and other operational factors affect the longevity of gas turbine blade. This paper is focused on the selection of suitable materials that can withstand the severe working condition and thermo-structural analysis using Finite Element method (FEM) to determine the behaviour of each material under service condition. Cambridge Engineering Software (CES) was employed in the material selection process where GTD111, U500 and IN 738 were identified prior to analyzing U500 and IN 738 due to desired mechanical properties over GTD111. Employing ANSYS R15.0 in the steady state thermal analysis, maximum service temperature of 736.49°C and maximum Total heat flux of  $4.345 \times 10^3 \text{ W/m}^2$  was obtained for IN 738 material while maximum service temperature of 728.29°C and maximum Total heat flux of  $4.1746 \times 10^3 \text{ W/m}^2$  was obtained for U500 blade material. For structural static analysis, maximum von-mises stress of 454 MPa and total deformation of 0.16221 obtained for IN 738 while maximum von-mises stress of 416 MPa and total deformation of 0.12125 was obtained for U500 blade material. While the FEA analytical results for both materials exhibited less variations between each other, IN 738 displayed better thermal characteristics, whereas, U500 presented satisfactory structural static results and above all, von-mises stresses obtained for both materials was below their yield strength and melting temperature. Hence, gas turbine blade materials should be assessed thoroughly for structural and thermal conditions before manufacturing.

**Keywords:** Gas turbine, Turbine blade, Temperature, Material properties, Stress, Deformation.

### 1. Introduction

The gas turbine engines are more critical to the operation of power plants, aircraft and heavy duty vehicles. A typical gas turbine engine consists of three major parts namely; compressor, combustion chamber and the turbine in addition to the generator [1]. Gas turbine blades are the specific component responsible for extracting energy from the high temperature and high pressure gas produced from the combustion chamber. The combustible gas in the process converts potential energy of the stationary blade to kinetic energy of the blade which in turn generates electrical power. During the operation of gas turbine engine, the turbine blades are subjected to high temperatures and stresses [2]. Turbine blades are exposed to loads that can cause failure during operation, therefore, the gas turbine blade component must be design with



in-depth consideration of vibration and thermal stresses induced on the blade in service condition [3]. A major cause of turbine blade failure is High Cycle Fatigue (HCF) caused by repeated cyclic loads on the rotor blade [4]. Gas temperatures at the turbine inlet is between 1200°C to 1600°C, but some as a result of over loading have increased inlet temperatures as high as 1600°C which may cause fatigue and fracture of the blades/discs [5]. Boyce [6] reported that the 5th stage of the low pressure turbine operates at a temperature of about 800°C, while the 1st stage intermediate pressure turbine operates at a temperature of about 1100°C and the 1st stage high pressure turbine operates at a temperature of about 1500°C respectively. According to Ikpe et al. [7], the high pressure turbine is exposed to the most intense temperature (450°-1300°) and pressure while the Low Pressure (LP) turbine is exposed to lower temperature (80°-400°) air pressure. Hot gases from the combustor are accelerated prior to entering the gas turbine and this significantly lowers the turbine maximum temperature from approximately 1800°C to approximately about 1100°C while entering the first turbine stage [8]. These challenges can be unravelled through the use of materials with relatively high melting point (such as material with temperature above the operating condition of the gas turbine engine), surface coating and cooling techniques which are the areas that will be addressed in this paper. Choi and Lee [19] studied a gas turbine failure scenario by investigating the broken surface of the blade and stress analysis of the blade and was observed that the maximum stress occurred due to the pressure profiles developed during operation. Umamaheswararao and Mallikarjunarao [10] conducted a structural static analysis on three potential gas turbine blade materials which included mild steel, N-155 and Inconel 718. It was found that displacement is less for INCONEL 718 compared to mild steel and N- 155, while the von-mises stress was within the yield strength of the material with optimum deformation compared to mild steel and N-155. Kumar and Pandey [11] investigated the potentials of super alloy X, Nimonic 80A and Inconel 625 as possible turbine blade materials at three different speeds viz; 20000, 40000 and 60000 RPM and found out that the bent profile of Inconel 625 is the best combination for all the speeds. Sushila et al. [12] carried out failure analysis on first stage IN738 gas turbine blade tip cracking to determine the causes of gas turbine blade failure of 30MW thermal power plant. It was found that surface degradation due to overheating, oxidation, fatigue, degradation of coatings, hot corrosion, sulphidation, embrittlement and thermal aging are the major causes. Difference in operating condition of the HP and LP turbine has over the years resulted in the design of HP and LP turbine blades which are greatly different in material and cooling options despite the same thermodynamic and aerodynamic principles In this study, thermal-structural FEA was carried out on potential turbine blade materials to check their suitability.

## **2. Materials and Method**

The Initial search was performed using fatigue strength and density as the basis in Cambridge Engineering Software (CES) Edupack to determine the materials with maximum fatigue strength and minimum density under service temperature between 800°C and 1300°C without failure, and possible materials were captured as presented in Fig. 1.

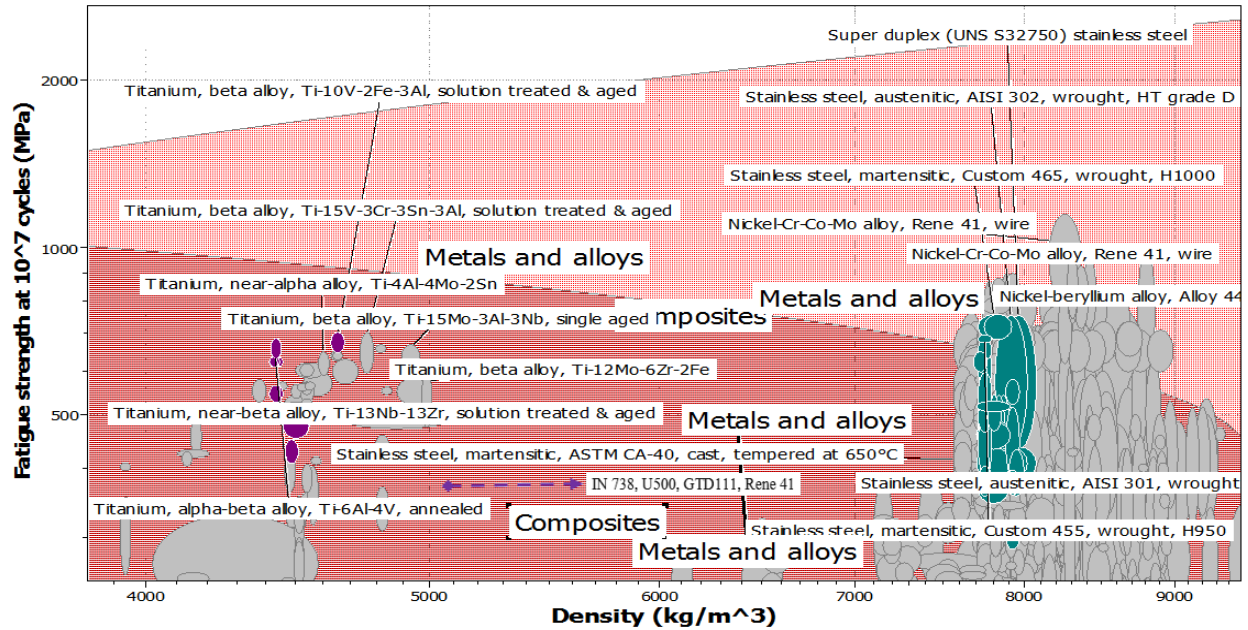


Fig. 1. Graph of Fatigue Strength against Density

Further search was performed using maximum yield strength and density as the basis in CES Edupack to determine the materials with reference service temperature (between 500°C and 950°C) according to existing literatures [13]. The box method was applied for optimization and selection of possible materials suitable for gas turbine blade as shown in Fig. 2.

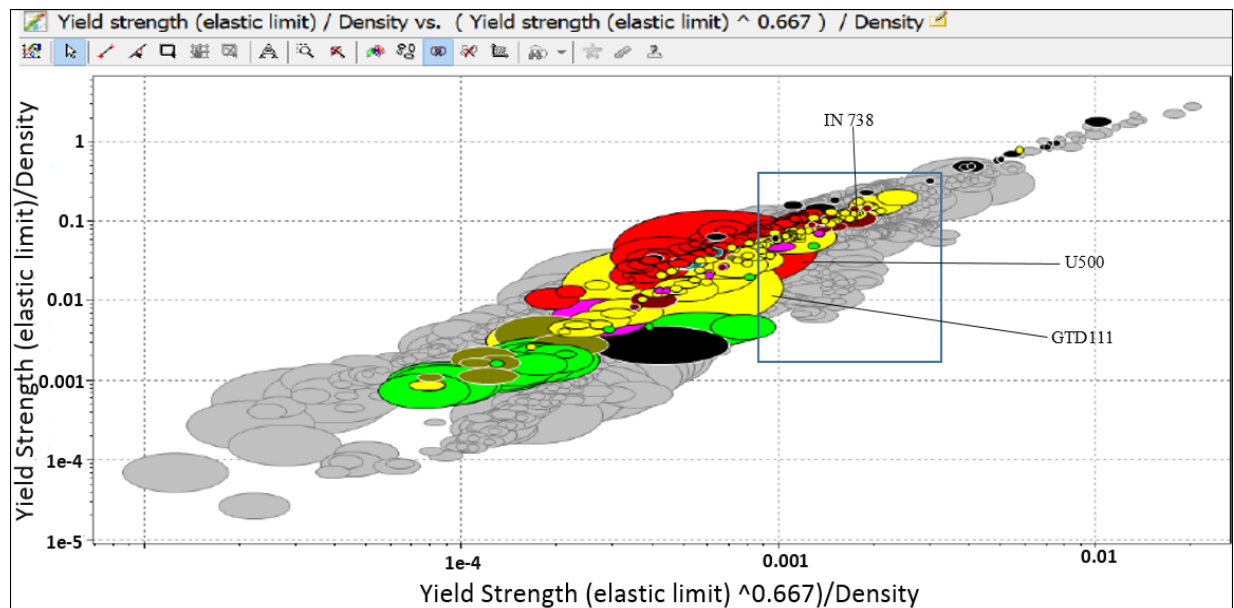


Fig. 2. Graph of Yield Strength against Density

As shown in Fig. 2, the three materials (GTD111, U500 and IN 738) were indicated in the second search which were also captured in the initial search indicated with broken arrow as shown in Fig. 1. These three super alloy materials are in agreement with studies on gas turbine blade materials by Nageswara [14]. These blade material properties were created with ANSYS by double clicking on the engineering material data located in ANSYS workbench. A new page having engineering materials data opened right next to project. The default material on ANSYS was structural steel. A list of several possible properties found on ANSYS was found in the Toolbox. After selecting the appropriate properties for the material intended to be created, the

material properties then displayed. Properties of the three possible gas turbine blade materials selected in Fig. 2 are summarized in Table 1. Nominal composition of the various blade material are provided in the Table 2.

Table 1. Material Properties of possible Gas Turbine Blade

Materials	GTD 111	U 500	IN 738
Specific Heat (J/KgK)	460	500	510
Young's Modulus (GPa)	130	190-210	149
Density (kg/m <sup>3</sup> )	8870	8027	8550
Poisson's ratio	0.33	0.27-0.30	0.30
Thermal conductivity (W/mk)	16	16.2	14.3
Thermal expansion (0C)	9x10 <sup>-6</sup>	17.5x10 <sup>-6</sup>	12.5x10 <sup>-6</sup>
Yield strength (MPa)	564.32	500	792
Melting temperature (0C)	1699	1360	1400
Bulk Modulus (Pa)	1.0833x10 <sup>11</sup>	1.583x10 <sup>11</sup>	1.247x10 <sup>10</sup>
Shear Modulus (Pa)	5x10 <sup>10</sup>	7.307x10 <sup>10</sup>	5.730x10 <sup>10</sup>

Table 2. Nominal Composition of Possible Gas Turbine Blade Material

Materials	Composition (Alloying Elements)											
	Ni	Cr	Co	Ti	Al	C	W	Mo	B	Nb	Ta	Fe
IN 738	Bal	16	8.3	3.4	3.4	0.10	2.6	1.75	0.001	0.9	1.75	0.2
GTD111	Bal	14	9.5	4.9	3	0.10	3.8	4.5	0.01	-	2.8	-
U500	Bal	17.5	16.5	3.9	2.9	-	0.8	4	0.01	-	-	4

## 2.1. FEA of Gas Turbine Blade

The FEA configured the turbine blade model for analysis using a complex system of points or nodes connected into a grid known as mesh. The nodes were arranged at a specific density throughout the model. The geometry of the gas turbine blade is modeled in SOLIDWORKS and then imported into ANSYS for meshing. The aero foil profile of the rotor blade was generated on the XZ plane with the help of key points defined by the coordinates. Then a number of splines were fitted through the key points, creating the 2D aero foil shape. The geometry of the blade was meshed with 8 noded tetrahedral brick element but the element type used for this purpose was Tetrahedron 10. It has 3 degrees of freedom per node, that is, translation in X, Y and Z directions were used. The element has plasticity, creep, swelling, stress stiffening, large deflection, and large strain capabilities etc. The blade dimensions are given in Table 3, while Fig. 3 represents the gas turbine blade geometrical models created in SOLIDWORKS and meshed gas Turbine blade using ANSYS. The steps employed in the course of the analysis are as follows;

- i. Creating a three dimensional model in SOLIDWORKS software 2016
- ii. Import the SOLIDWORKS model in ANSYS 15.0 software
- iii. Mesh the imported model in ANSYS
- iv. Apply boundary conditions and,
- v. Solve the system equations to find out the unknowns
- vi. Validation of solutions obtained with the operating conditions

Table 3. Gas Turbine Blade Dimensions

Parameter	Value
Name	NACA6409 9%
Blade Span (mm)	120mm
Blade Axial Chord Length (mm)	68.30mm
Blade Root Length (mm)	60mm
Thickness (%)	100
Pitch (deg)	14

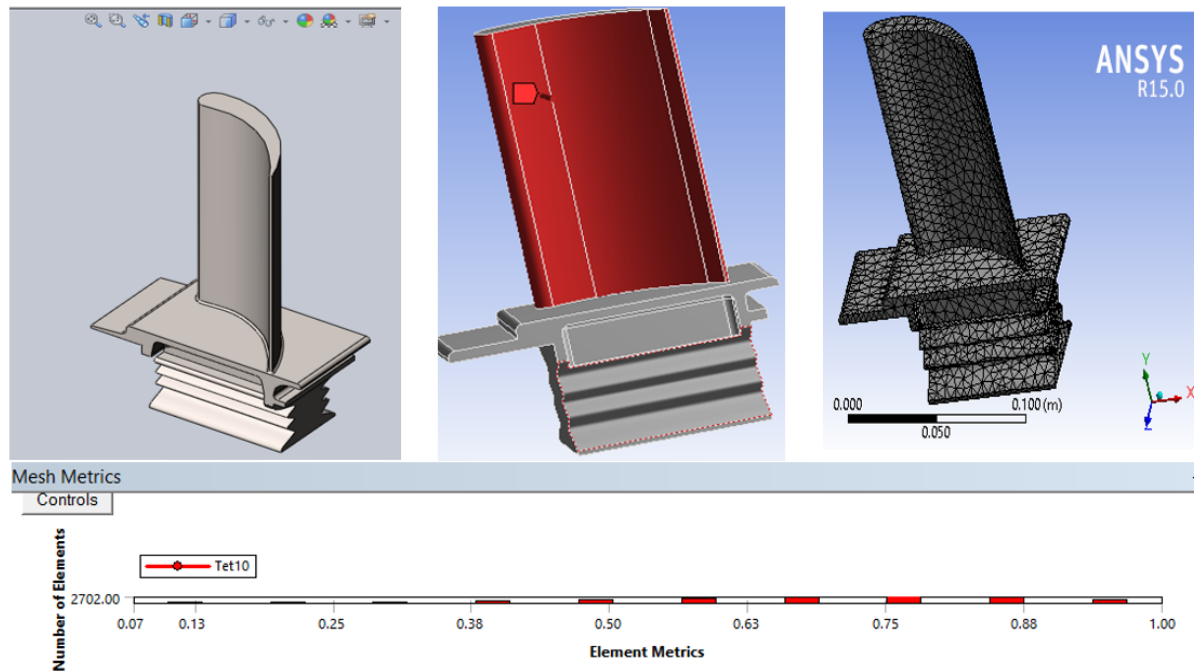


Fig. 3. Gas Turbine Blade Geometries in SOLIDWORKS and Meshed Blade using ANSYS

## 2.2. Thermal Analysis

Heat transfer in fluids occurs by means of conduction as well as convection. Force convection is the dominant phenomena in turbine flows. The boundary conditions for steady state thermal analysis as applied to the turbine blade in the analysis are indicated in Table 4. Operational Parameters of the Gas Turbine Blade are presented in Table 5.

Table 4. Steady-state Boundary Condition for the Thermal Analysis

Parameters	Value
Turbine Inlet Temperature ( $^{\circ}\text{C}$ )	950
Convective Heat Transfer Coefficient On Tip ( $\text{W}/\text{M}^2\text{K}$ )	800
Convective Heat Transfer Coefficient On Pressure Side ( $\text{W}/\text{M}^2\text{K}$ )	1000
Convective Heat Transfer Coefficient On Suction Side ( $\text{W}/\text{M}^2\text{K}$ )	1300
Turbine Exit Temperature ( $^{\circ}\text{C}$ )	480

Table 5. Operational Parameters of the Gas Turbine Blade

Pressure (bar)	8
Speed (rpm)	5100
Tangential force (N)	177.48
Axial force (N)	0.3439
Centrifugal (N)	40,680

### 3. Results and Discussion

Results obtained from the thermal-structural analysis in this study are presented in this section.

#### 3.1. Steady-state Thermal Analysis

In a gas turbine blade, boundary layer develops on the blade surface and the free stream temperature are of interest. This layer acts as a buffer between the solid blade and the hot free stream, and offers resistance to heat transfer. Heat transfer occurs in this viscous layer between the blade and the fluid through both conduction and convection. After inputting the boundary conditions presented in Table 4 and applying it on the gas turbine blade, the following results were obtained for IN 738 and U500 blade materials as shown in Figs. 4-7. This boundary condition caused convective heat transfer to occur through one or more flat or curved faces (in contact with a fluid). Exhaust gases from the combustor are directed through the turbine in such a manner that the hottest gases impinge on turbine blades. It was observed that the maximum temperature is experienced at the leading edge of the blade, however, there was a temperature fall from the leading edge to the trailing edge of the blade. Since heat is transferred from the region of high temperature to a region of low temperature, the maximum heat flux was observed at the trailing edge.

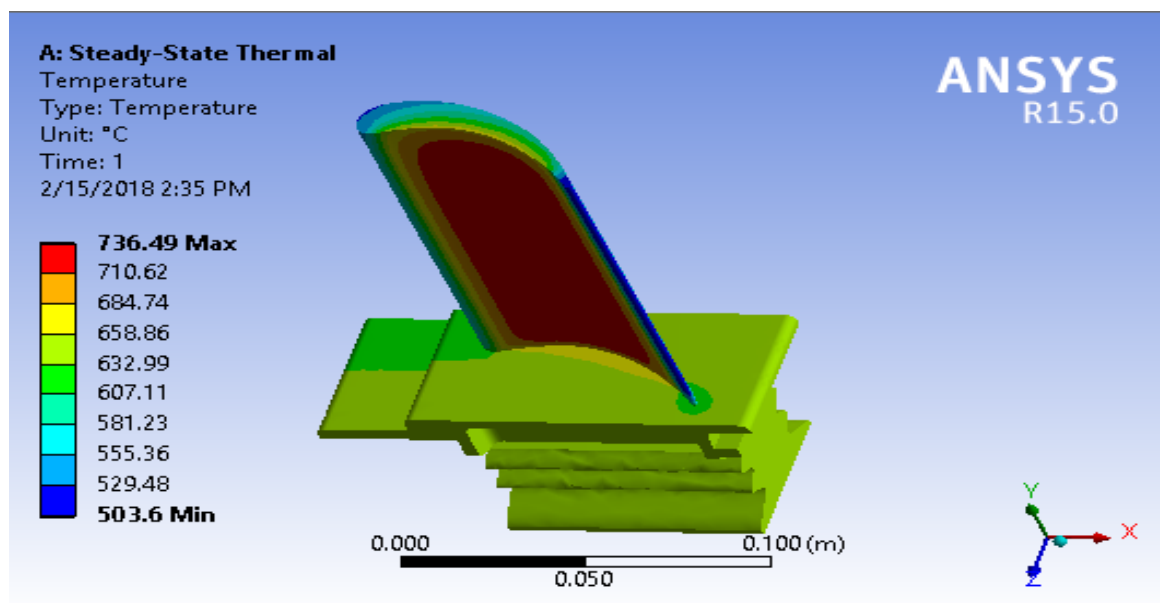


Fig. 4. Temperature distribution on IN738 Turbine Blade Material

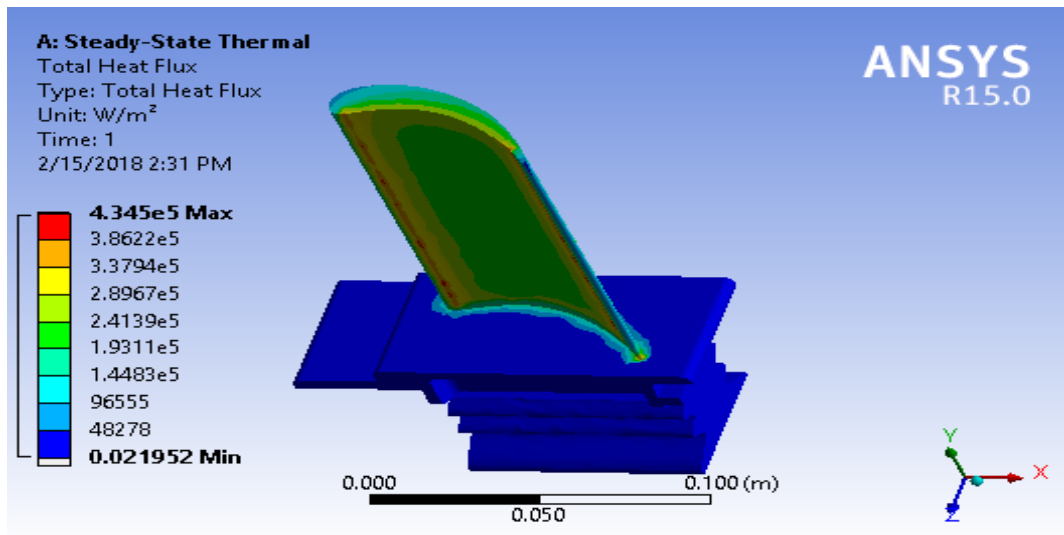


Fig. 5. Heat Flux on IN 738 Turbine Blade Material

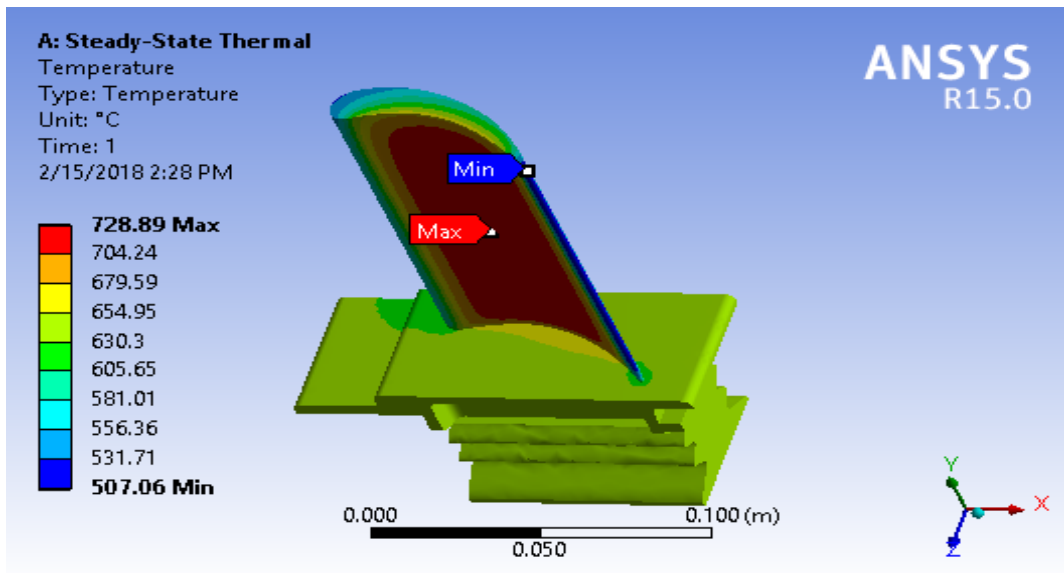


Fig. 6. Temperature distribution on U500 Turbine Blade Material

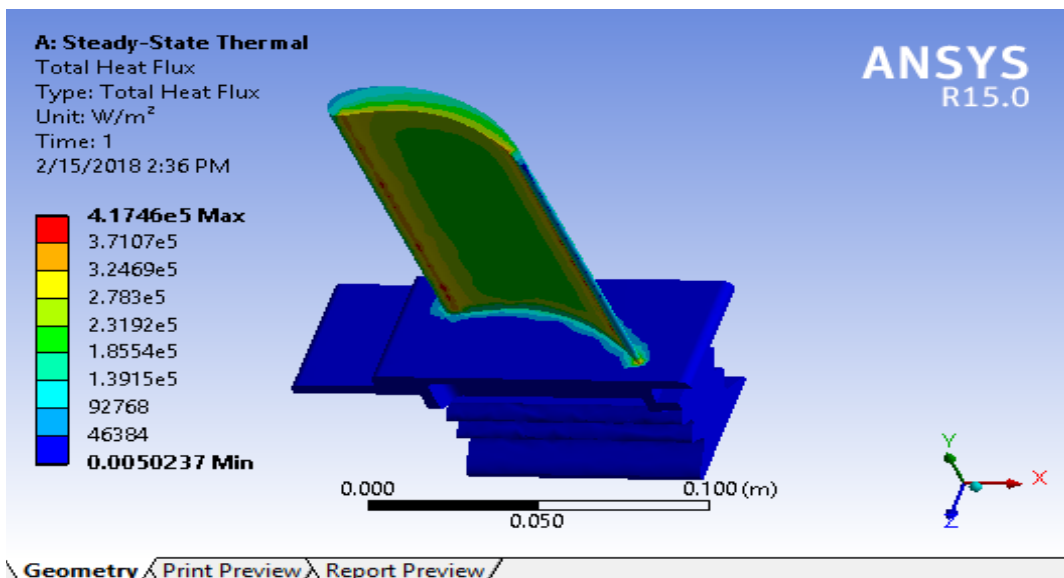


Fig. 7. Heat Flux on U500 Turbine Blade Material

From Fig. 8, it can be observed that the maximum temperature of the various blade material fall below their corresponding melting temperature. The maximum temperature and heat flux were closely varying between the two turbine blade materials. IN 738 a higher temperature and heat flux characteristics compared to U500. Variations in maximum temperature and heat flux between the two blade materials is due to their differences in material properties.

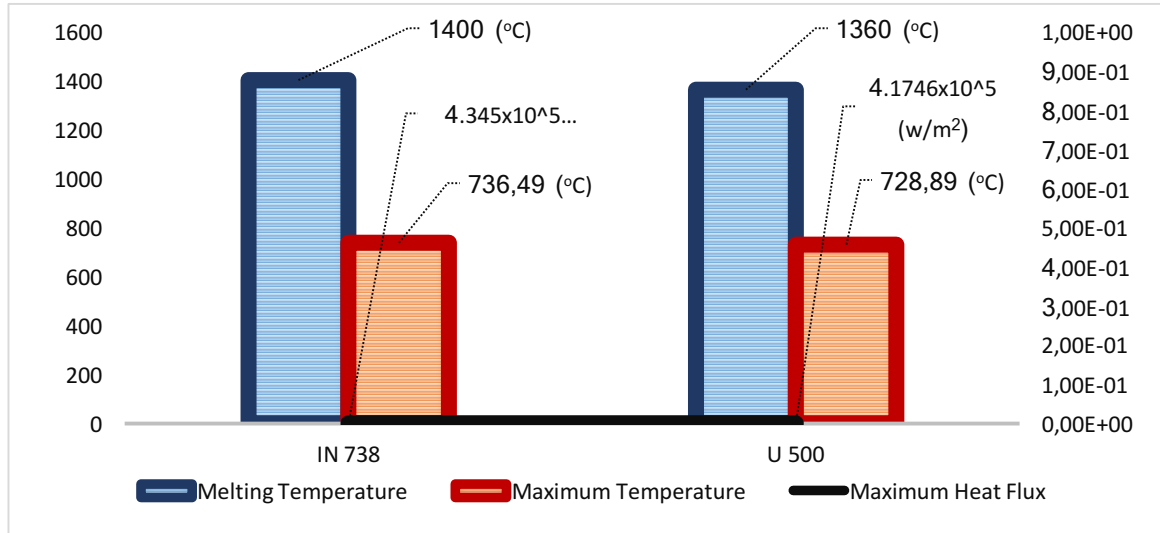


Fig. 8. Maximum Temperature and Heat Flux for Turbine Blade Materials

The temperatures observed were below the melting temperature of the blade materials, as both IN738 and U500 turbine blade materials exhibited high temperatures of 736°C and 728°C as shown in Fig 8. Depending on the severity of heat flux in the gas turbine engine, the temperature can have significant effects on the overall turbine blade performance. The non-uniform temperature distribution from the tip to the root of the blade materials may induce thermal stresses on the turbine blade, while thermal stresses along with the mechanical stresses set up in the turbine blade during service condition may reduce the life of blade material. Figs. 9-11 represent the results obtained when static structural analysis was performed on IN 738 turbine blade material while Figs. 12-14 represent the results obtained when static structural analysis was performed on U500 turbine blade material.

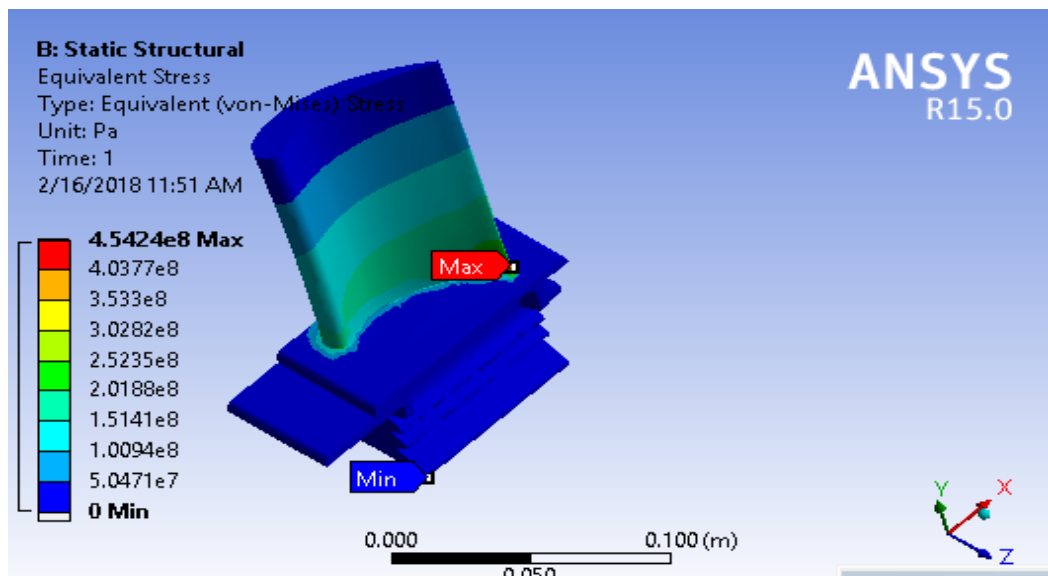


Fig. 9. Von-mises Stress on IN738 Turbine Blade Material

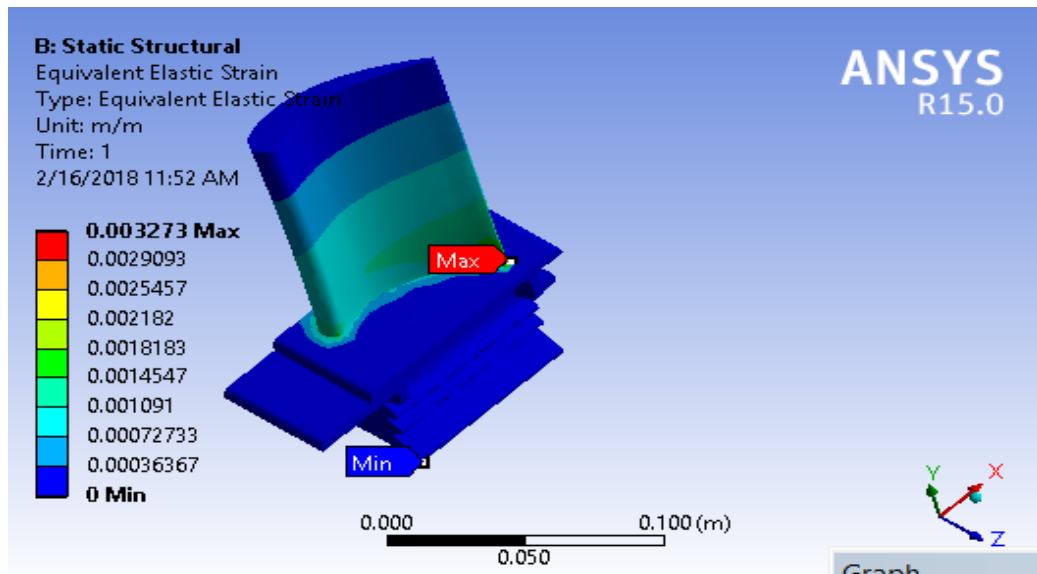


Fig. 10. Elastic Strain on IN738 Turbine Blade Material

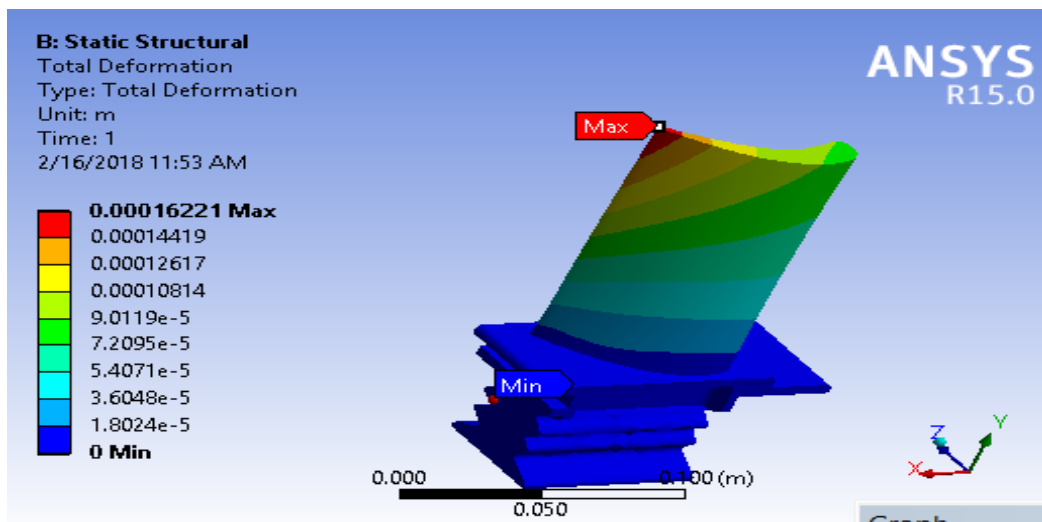


Fig. 11. Total Deformation on IN738 Turbine Blade Material

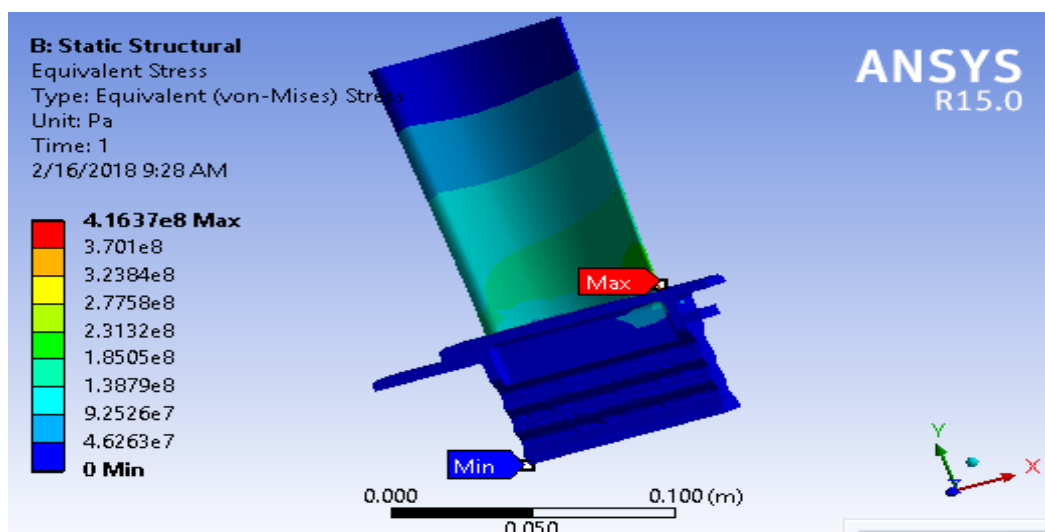


Fig. 12. Von-mises stress on U500 Turbine Blade Material

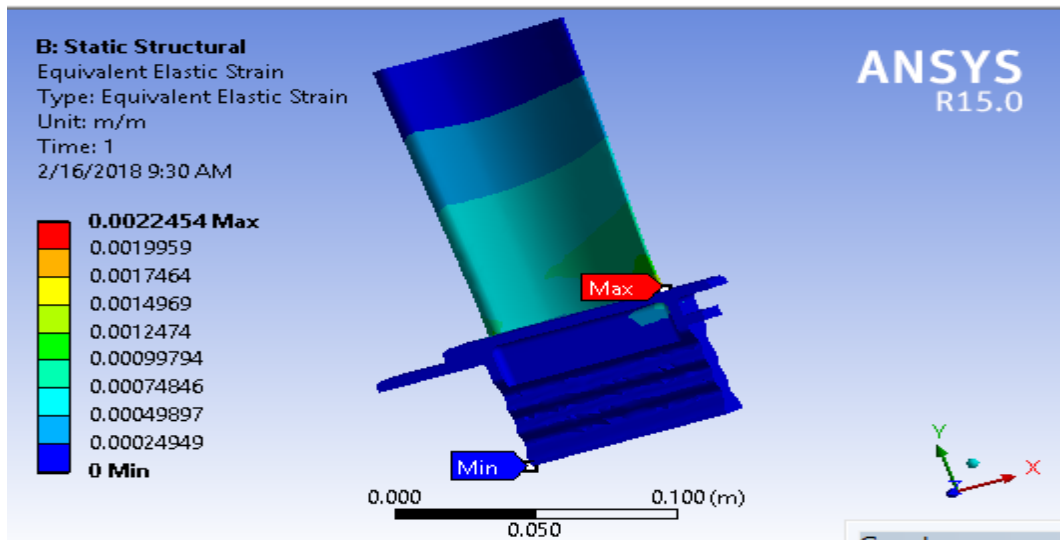


Fig. 13. Elastic Strain on U500 Turbine Blade Material

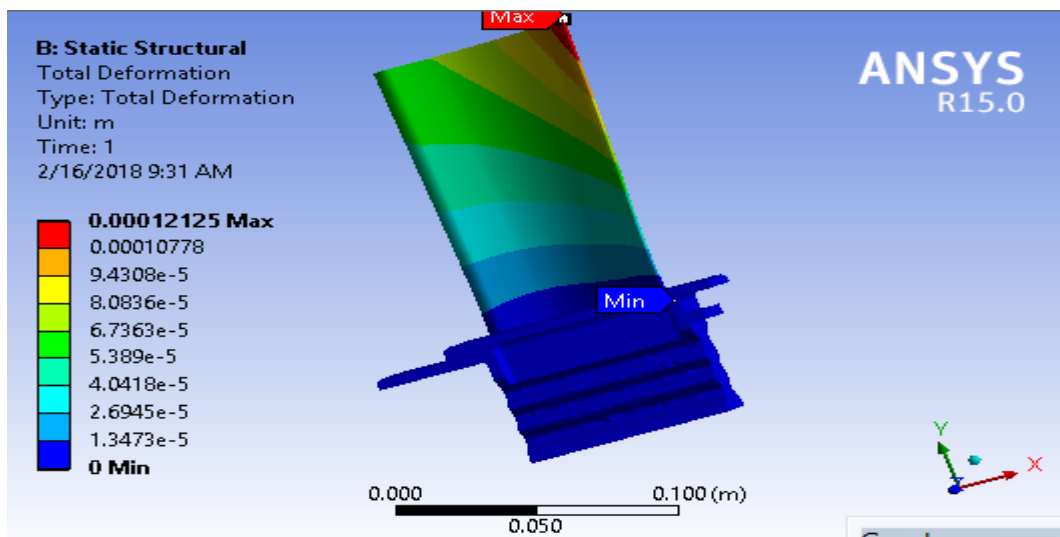


Fig. 14. Total Deformation on U500 Turbine Blade Material

A summary of results obtained from the static structural analysis for both IN738 and U500 turbine blade materials is presented in the in Fig. 15. The results presented in Fig. 15 were extracted from the results of stress, strain and deformation from the structural analysis in Figs. 12-14 respectively. The maximum stress exhibited by IN738 blade material and U500 is below their corresponding yield strength. For failure not to occur, the stresses exhibited by the blade materials must be below their yield strength. Therefore, IN738 and U500 are safe under the specified boundary conditions in this study.

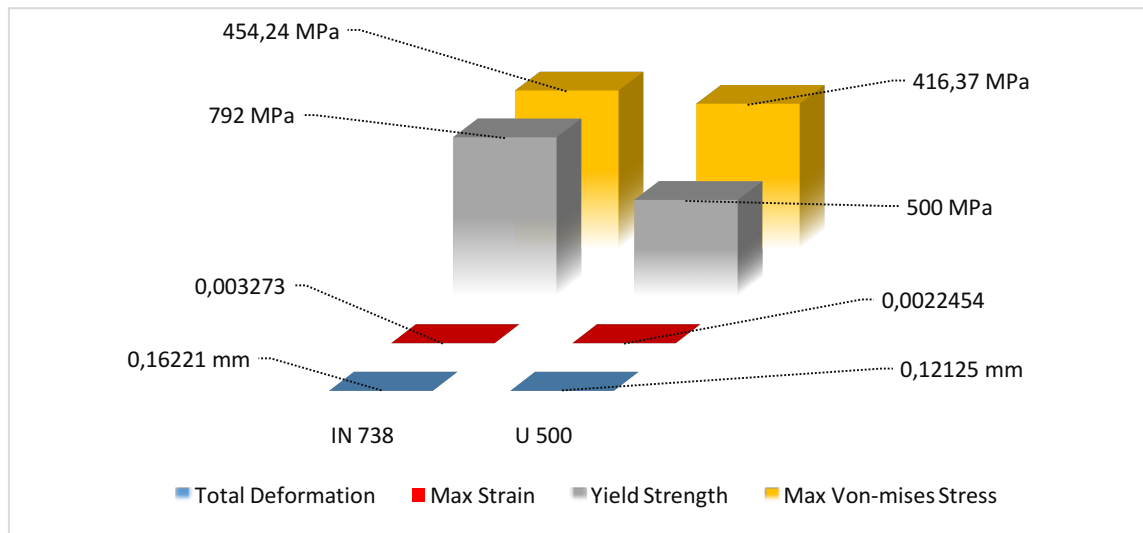


Fig. 15. Variations of Structural Parameters across Different Materials

Static-Structural analysis was performed on the turbine blade to analyze the stress, strain and deformation on the turbine blade. A pre-stress from the steady state thermal analysis in addition to the structural load was performed on the blade to determine the failure criteria on the blade material. The yield criteria was used to relate multi-axial stress state with the uniaxial stress state. Von-mises (Equivalent stress) is part of the maximum equivalent stress failure theory used to predict yielding in a ductile material. The actual structure usually exhibits multi-axial stress state. The yield criterion provides a scalar invariant measure of the stress state of the material which is compared with the uniaxial stress state. Generally, a stress state possesses two components namely;

- i. Hydrostatic stress: which generates change in volume.
- ii. Deviatoric stress: which generates angular distortion (change in shape).

The von Mises yield criterion states that yielding will occur whenever the distortion energy in a unit volume equals the distortion energy in the same volume when uni-axially stressed to the yield strength. Therefore, if von Mises equivalent stress exceeds the uniaxial material yield strength, yielding will occur. The blade root has more strength when compared to the blade span (free end of the blade). After incorporating the boundary conditions and various forces acting on the blade from Table 4 and 5, color profile on the turbine blade model indicated areas of maximum and minimum stress, strain and deformation. The red contours represents maximum values while the blue contours represents minimum values. It was found that maximum stress and strain developed at the joint sections of root and blade volumes (trailing edge), while maximum deformation is found at the blade tip. Variation of deformation, stress, and strain for the two materials were examined from the structural analysis. Maximum deformation was observed at the top blade tip sections and minimum elongations at the root of the blade as shown in Figs. 11 and 14. To avoid failure of the gas turbine blade due to creep, deformation on the blade must be as less as possible. Comparing the maximum deformation under the same load condition for both materials, total deformation for IN738 was 0.16221mm whereas, the total deformation obtained for U500 blade material was 0.12125mm as illustrated in Fig. 15. Deformation values obtained by Bhupendra et al. [15] from super alloy (N-155 nickel based alloy) in the category of IN738 and U500 ranged between 0.000177mm and 0.000274mm which are less compared to deformation values obtained in this study. This may have been due to the variations in material properties and compositions. Maximum stresses and strains were observed on the trailing edge, at the joint between the blade span and the root. The maximum

von-mises stress for U500 (yield strength of 500 MPa) and IN738 (yield strength of 7920) was below the corresponding yield strength of the materials. Comparing the maximum von-mises stresses for both materials under same loading condition, the von-mises stress on IN738 was 454MPa while von-mises stress of 416MPa was obtained for U500 blade material as shown in Figs. 9 and 12. Also, comparing the results obtained for maximum strain across the various materials, strain on IN738 was 0.003273 while the strain value obtained for U500 was 0.0022454 as shown in Figs. 10 and 13 respectively. The gas turbine blade is prone to failure when the maximum stress at the trailing edge near the root of the blade exceeds the yield stress of the blade material. From the result obtained from the thermal analysis, variations in the temperature of the two material indicated that maximum temperatures prevailed at the leading edge of the blade, while temperatures distribution below the maximum temperature was observed at the trailing edge and along the blade root. Hence, both turbine blade materials investigated in this study are safe as potential gas turbine blade materials, as their maximum service temperatures were below their melting temperature, also, as their yield strengths obtained in the course of the analysis were below their yield strength.

#### 4. Conclusion

Turbine Blades are one of the most important components in the gas turbine engine. The blades are operated in harsh environmental condition at elevated temperature, high pressure and large centrifugal forces that hampers the performance and longevity of the blade material in service condition. The turbine blade material is exposed to unforeseen failure depending on the severity, and this necessitated the thermal and structural static analysis carried out in this study. From the analysis of the results, it was observed that the temperature on the turbine blades for both materials was below the melting temperature of the blade materials. Maximum temperatures were observed at the leading edge of the blade and decreased towards the trailing edge and blade root. Maximum von-mises stresses and strains were observed near the root of the turbine blade and upper surface along the blade roots. Total deformation obtained from each blade analysis were negligible, as 0.16221mm was obtained for IN 738 and 0.12125 mm obtained for U 500. This report serves as a guideline for the selection of suitable materials for minimal gas turbine blade failure and optimal working scenario.

#### References

- [1] Sulaiman, K.S., Rameshkumar, G.R., Vibration Diagnosis Approach for Industrial Gas Turbine and Failure Analysis, *British Journal of Applied Science & Technology*, 14(2), 1-9, 2016.
- [2] Kalapala P., Prasad, B.A., Anandarao, M., Material Optimization and Dynamic Approach for performance criteria in application to Gas Turbine Blade to overcome resonance; *International Journal of Scientific & Engineering Research*, 8(6), 189-196, 2017.
- [3] Hassan M., *Vibratory Analysis of Turbomachinery Blades*, Rensselaer Polytechnic Institute, Hartford, Connecticut, 2008.
- [4] Gharzwan M.A., *High Cycle Fatigue Testing of Steel for Federal Aviation Administration (FAA)*, Department of Mechanical Engineering, California State University, Sacramento, (2017).
- [5] Mohamad, B.A., Abdelhussien, A., Failure Analysis of Gas Turbine Blade Using Finite Element Analysis, *International Journal of Mechanical Engineering and Technology (IJMET)* 7(3), 299-305, 2016.

- [6] Boyce, M.P., *The Gas Turbine Handbook*, Gulf Professional Publishing, Houston Texas, 2<sup>nd</sup> edition 2002.
- [7] Ikpe A.E., Owunna I., Ebunilo, P.O., Ikpe, E., Material Selection for High Pressure (HP) Turbine Blade of Conventional Turbojet Engines, *American Journal of Mechanical and Industrial Engineering* 1(1), 1-9, 2016.
- [8] Nathan, S., Jewel in the Crown: Rolls-Royce's Single-Crystal Turbine Blade Casting Foundry, [online] available at, <https://www.theengineer.co.uk/issues/june-2015-online/jewel-in-the-crown-rolls-royces-single-crystal-turbineblade-casting-foundry/>, 2015.
- [9] Choi Y, Lee K, Investigation of blade failure in a gas turbine, *Journal of Mechanical Science and Technology*, 24(10), 1969-1974, 2010.
- [10] Umamaheswararao, L., Mallikarjunarao, K., Design and analysis of a gas turbine blade by using FEM, *International Journal of Latest Trends in Engineering and Technology (IJLTET)*, 4(4), 19-24, 2014.
- [11] Kumar. R.R. Pandey, K.M., Static Structural and Modal Analysis of Gas Turbine Blade, *IOP Conference Series, Materials Science and Engineering* 225(012102), 1-9, 2017.
- [12] Sushila, R., Atul, K.A. Vikas, R., Failure Analysis of a First Stage IN738 Gas Turbine Blade Tip Cracking in a Thermal Power Plant, *Case Studies in Engineering Failure Analysis*, 8, 1-10, 2017.
- [13] Rao, V.N., Kumar, I.N., Madhulata, N., Abhijeet, A., Mechanical Analysis of 1<sup>st</sup> Stage Marine Gas Turbine Blade, *International Journal of Advanced Science and Technology*, 68, 57-64, 2014.
- [14] Nageswara, R.M., *Materials for Gas turbines*, *Advances in Gas Turbine Technology*, 293-314, Intech Publisher, ISBN: 978-953-307-611-9, 2011.
- [15] Bhupendra, E.G., Sachin, V.B., Kapil B.S., Vibration Analysis of Gas Turbine Blade Profile Using FEM Technique and Tool, *International Journal of Research in Advent Technology*, 2(1), 182-189, 2014.



## Derivation of Nonlocal Finite Element Formulation for Nano Beams

Hayri Metin Numanoglu<sup>a</sup>, Büşra Uzun<sup>b</sup>, Ömer Civalek<sup>c\*</sup>

<sup>a,b,c\*</sup> Akdeniz University, Civil Engineering Department, Antalya-TURKIYE

E-mail address: [metin\\_numanoglu@hotmail.com](mailto:metin_numanoglu@hotmail.com)<sup>a</sup>, [uzunbusra34@gmail.com](mailto:uzunbusra34@gmail.com)<sup>b</sup>, [civalek@yahoo.com](mailto:civalek@yahoo.com)<sup>c\*</sup>

ORCID numbers of authors:

0000-0003-0556-7850<sup>a</sup>, 0000-0002-7636-7170<sup>b</sup>, 0000-0003-1907-9479<sup>c</sup>

Received date: 01.08.2018

Accepted date: 14.08.2018

### Abstract

*In the present paper, a new nonlocal formulation for vibration derived for nano beam lying on elastic matrix. The formulation is based on the cubic shape polynomial functions via finite element method. The size effect on finite element matrix is investigated using nonlocal elasticity theory. Finite element formulations and matrix coefficients have been obtained for nano beams. Size-dependent stiffness and mass matrix are derived for Euler-Bernoulli beams.*

**Keywords:** Size-dependend vibration, cubic shape functions, Nonlocal elasticity, Euler-Bernoulli beam, new mass and stiffness matrix.

### 1. Introduction

It is known that the nanotechnology has enabled the opening of a new era in many areas in nano optics, microcomputers and micro devices, chemical, medicine, engineering, electronics. For keep up with technology fast, the correct solution method which considers the size effect is the most important factor. Experimental research is very difficult and expensive. Some methods such as Hybrid atomistic–continuum mechanics and related to the atomic modeling; molecular dynamics [1-3], tight-binding molecular dynamics, the density functional theory take into account the size effect. Therefore, various theories have been developed that gives importance to effects of small scale such as strain gradient theory [4,5], modified couple stress theory [6-9], couple stress elasticity theory [10-13], nonlocal elasticity theory [14-15]. Nonlocal elasticity theory of Eringen is the most widely used among them. According to the nonlocal elasticity theory of Eringen [14-15], the stress at any reference point is effecting the whole body which not depends only on the strains at this point but also on strains at all points of the body. This definition of the Eringen's nonlocal elasticity is based on the atomic theory of lattice dynamics, and some experimental observations on phonon dispersion. Nonlocal



theory considers long-range interatomic interaction and yields to results dependent on the size of a body [14-16]. Applying first the nonlocal elasticity theories to nanotechnology is by Peddieson et al. [17] and Sudak [18]. Nanostructures with nonlocal elasticity theory have been studied for different type ( numerical and analytical) solution with contributions continuum mechanics by finite element method [19-25], by finite difference method [26-27] by differential transform method [28-30], by differential quadrature method [31-34], and by analytical solution [35-43].

## 2. Size dependent formulation

The main equations for a homogenous and isotropic elastic continuum body can be stated as [14,15,16]:

$$\sigma_{ij,j} = 0, \quad (1)$$

$$\sigma_{i,j}(x) = \int_V \alpha(|x - x'|, \chi) C_{ijkl} \varepsilon(x') dV(x'), \quad (2)$$

$$\varepsilon_{ij}(x') = \frac{1}{2} (u_{i,j} + u_{j,i}), \quad (3)$$

where  $\sigma_{ij}$  is the nonlocal stress tensor,  $\rho$  is the mass density of the body,  $u$  is the displacement vector at a reference point  $x$  in the body,  $C_{ijkl}(x')$  is the classical (Cauchy) or local stress tensor at any point  $x'$  in the body,  $\varepsilon_{ij}(x')$  is the linear strain tensor at point  $x'$  in the body,  $t$  is denoted as time,  $V$  is the volume occupied by the elastic body,  $\alpha|x - x'|$  is the distance in Euclidean form,  $\lambda$  and  $\mu$  are the Lamé constants.  $\alpha|x - x'|$  is the nonlocal kernel which defines the impact of strain at point  $x'$  on the stress at point  $x$  in body. The nonlocal constitutive formulation is

$$[1 - (e_0 a)^2 \nabla^2] \sigma_{ij} = C_{ijkl} \quad (4)$$

The displacement components based on the Euler-Bernoulli beam theory may be written as [36-37]:

$$u = -z \frac{\partial w}{\partial x}, \quad v = 0 \quad w = w(x, t) \quad (5)$$

where ‘ $w$ ’ is the transverse displacement. The strain-displacement equations for Euler-Bernoulli beam is given by

$$\varepsilon_{xx} = \frac{\partial u}{\partial x} = -z \frac{\partial^2 w}{\partial x^2}(x, t) \quad \varepsilon_{yy} = \varepsilon_{zz} = \varepsilon_{xy} = \varepsilon_{xz} = \varepsilon_{yz} = 0 \quad (6)$$

Consider the stress-strain relation for Euler-Bernoulli beam is given by

$$\sigma_{xx} = -Ez \frac{\partial^2 w}{\partial x^2}(x, t) \quad \sigma_{yy} = \sigma_{zz} = \tau_{xy} = \tau_{xz} = \tau_{yz} = 0 \quad (7)$$

According to Eq. (4), the nonlocal stress-strain equations for beam can be written as [36-37]

$$\sigma_{xx} - (e_0 a)^2 \frac{\partial^2 \sigma_{xx}}{\partial x^2} = E \varepsilon_{xx}, \quad \sigma_{yy} = 0, \quad \sigma_{zz} = 0 \quad (8a)$$

The generalized Hamilton's principle has the form

$$\delta \int_0^t [T - (U - W)] dt = 0 \quad (9)$$

The strain and kinetic energies of the classic Euler-Bernoulli beam are equal to

$$U = \frac{1}{2} \int_V \sigma_{xx} \varepsilon_{xx} dV \quad (10)$$

$$T = \frac{1}{2} \rho \int_V \left[ \left( \frac{\partial w}{\partial t} \right)^2 \right] dV \quad (11)$$

The work done by the axial compressive force, Winkler foundation modulus ( $k_w$ ) and Pasternak foundation modulus ( $k_g$ ) can be expressed as

$$W = \frac{1}{2} \int_0^L \left[ (P - k_g) \left( \frac{\partial w}{\partial x} \right)^2 - k_w (w)^2 \right] dx \quad (12)$$

Substitution of Eqs.(10)-(11) into Eq.(9), acquired

$$\int_0^t \left[ \int_0^L \rho A \frac{\partial w}{\partial t} \delta \frac{\partial w}{\partial t} dx - \left( -M \delta \left( \frac{\partial^2 w}{\partial x^2} \right) dx \right) + \left( (P - k_g) \frac{\partial w}{\partial x} \delta \frac{\partial w}{\partial x} - k_w w \delta w \right) dx \right] dt = 0 \quad (13)$$

When Eq.(13) under the double integral equal to zero under the double integral, differential equations of motion,

$$\frac{\partial^2 M}{\partial x^2} = \rho A \frac{\partial^2 w}{\partial t^2} + (P - k_g) \frac{\partial^2 w}{\partial x^2} + k_w w \quad (14)$$

The nonlocal moment resultants for beam can be obtained via (8a) as

$$M_x - (e_0 a)^2 \frac{\partial^2 M_x}{\partial x^2} = -EI \frac{\partial^2 w}{\partial x^2} \quad (15)$$

Substitution of Eq.(14) in to Eq. (15) leads to

$$M = (e_0 a)^2 \left( \rho A \frac{\partial^2 w}{\partial t^2} + (P - k_g) \frac{\partial^2 w}{\partial x^2} + k_w w \right) - EI \frac{d^2 w}{dx^2} \quad (16)$$

Finally, by substituting Eq.(16) into Eq.(13), we obtained governing equations for nonlocal Euler-Bernoulli beam [21,22,28,34]

$$\rho A \frac{\partial^2 w}{\partial t^2} - \frac{\partial^2}{\partial x^2} \left[ (e_0 a)^2 \left( \rho A \frac{\partial^2 w}{\partial t^2} + (P - k_g) \frac{\partial^2 w}{\partial x^2} + k_w w \right) - EI \frac{\partial^2 w}{\partial x^2} \right] - (k_g - P) \frac{\partial^2 w}{\partial x^2} + k_w w = 0 \quad (17)$$

The Euler-Bernoulli beam element is a beam with four degrees of freedom (DOF) and has two end nodes: 1 and 2. The node displacement vector

$$w^e = [w_1 \quad \theta_1 \quad w_2 \quad \theta_2] \quad (18)$$

By multiplying shape function ( $\phi$ ) and discretized displacements at nodes ( $[w(t)]^{ne}$ ) of an element we obtain the displacement of element ( $w(x,t)^e$ )

$$w(x,t)^e = [\phi [w(t)]^{ne}] \quad \dot{w}(x,t)^e = [\phi [\dot{w}(t)]^{ne}] \quad (19)$$

To solve the equations the ‘Hermitian cubic shape functions’ are used. Dimensionless natural coordinate can be stated as below

$$\xi = \frac{2x}{L} - 1 \quad (20)$$

where  $L$  is the element length. By using the shape functions (Eq.(21)) and dimensionless natural coordinates (Eq.(20)), the stiffness matrix becomes (ignoring the axial load)

$$K^1 = \frac{EI}{L^3} \begin{bmatrix} 12 & 6L & -12 & 6L \\ 6L & 4L^2 & -6L & 2L^2 \\ -12 & -6L & 12 & -6L \\ 6L & 2L^2 & -6L & 4L^2 \end{bmatrix} \quad (21a)$$

Similarly

$$K^2 = (e_0 a)^2 \frac{(k_g)}{L^3} \begin{bmatrix} 12 & 6L & -12 & 6L \\ 6L & 4L^2 & -6L & 2L^2 \\ -12 & -6L & 12 & -6L \\ 6L & 2L^2 & -6L & 4L^2 \end{bmatrix} \quad (21b)$$

$$K^3 = \frac{(k_g)}{30L} \begin{bmatrix} 36 & 3L & -36 & 3L \\ 3L & 4L^2 & -3L & -L^2 \\ -36 & -3L & 36 & -3L \\ 3L & -L^2 & -3L & 4L^2 \end{bmatrix} \quad (21c)$$

$$K^4 = \frac{k_w}{420} \begin{bmatrix} 156L & 22L^2 & 54L & -13L^2 \\ 22L^2 & 4L^3 & 13L^2 & -3L^3 \\ 54L & 13L^2 & 156L & -22L^2 \\ -13L^2 & -3L^3 & -22L^2 & 4L^3 \end{bmatrix} \quad (21d)$$

$$K^5 = \frac{(e_0 a)^2 k_w}{30L} \begin{bmatrix} 36 & 3L & -36 & 3L \\ 3L & 4L^2 & -3L & -L^2 \\ -36 & -3L & 36 & -3L \\ 3L & -L^2 & -3L & 4L^2 \end{bmatrix} \quad (21e)$$

Also, the mass matrix can be given as

$$M^1 = \frac{\rho A}{420} \begin{bmatrix} 156L & 22L^2 & 54L & -13L^2 \\ 22L^2 & 4L^3 & 13L^2 & -3L^3 \\ 54L & 13L^2 & 156L & -22L^2 \\ -13L^2 & -3L^3 & -22L^2 & 4L^3 \end{bmatrix} \quad (22a)$$

$$M^2 = \frac{(e_0 a)^2 \rho A}{30L} \begin{bmatrix} 36 & 3L & -36 & 3L \\ 3L & 4L^2 & -3L & -L^2 \\ -36 & -3L & 36 & -3L \\ 3L & -L^2 & -3L & 4L^2 \end{bmatrix} \quad (22b)$$

$$K = K^1 + K^2 + K^3 + K^4 + K^5, \quad M = M^1 + M^2 \quad (22c)$$

Finally, the vibration of Euler-Bernoulli beam can be expressed as

$$\det|K - \omega^2 M| = 0 \quad (23)$$

### 3. Results

As numerical results, non-dimensional frequency values of boron nitride nanotube with clamped supports at both have been obtained and results listed in Table 1. The results obtained by discrete singular convolution are also given in this table. It is shown that, the frequency values are increased with the increasing value of nonlocal parameter.

Table 1. Dimensionless Frequency values of C-C boron nitride nanotube

$e_0 a/L$	Foundation parameters ( $K_w=10, K_g=50$ )					
	$\omega_1$		$\omega_2$		$\omega_3$	
	FEM	DSC	FEM	DSC	FEM	DSC
0.0	33.3266	33.3485	78.0638	78.0873	139.862	139.8836
0.1	34.9378	34.9403	74.1135	74.1205	116.255	116.2673
0.2	37.7969	37.8041	69.3394	69.3593	99.5596	99.5701
0.3	40.0275	40.0359	66.8639	66.8704	93.7733	93.7937
0.4	41.4571	41.4691	65.6397	65.6491	91.529	91.5383
0.5	42.3505	42.3712	64.9805	64.9907	90.5076	90.5214

### 4. Concluding remarks

Experimental studies have shown that the mechanical behaviors of nano-scaled systems are completely different from structures having conventional dimensions (centimeters, meter dimensions). Experimental study on nanostructures and nanostructures is both costly and time consuming. For this reason, by using higher-order elasticity theories, the results have been theoretically tried to be obtained closer and many higher order theories taking the size effect into account have been emerged. In this paper, nonlocal elasticity theory was used to investigate the dimensional effect for nano beams. Using the nonlocal elasticity theory, equation of free vibration of beams on elastic matrix has been obtained. Obtained differential equation is solved using the finite element methods.

### Acknowledgements

This study has been supported by The Scientific and Technological Research Council of Turkey (TÜBİTAK) with Project no: 117M495. This support is gratefully acknowledged.

### References

- [1] Sun, C. T., and Haitao, Z., Size-dependent elastic moduli of platelike nanomaterials. *Journal of Applied Physics* 93(2), 1212-1218, 2003.

- [2] Zhu, R., Pan, E., and Roy, A. K., Molecular dynamics study of the stress–strain behavior of carbon-nanotube reinforced Epon 862 composites. *Materials Science and Engineering: A*, 447(1), 51-57, 2007.
- [3] Liang, Y. C., Dou, J. H., and Bai, Q. S., Molecular dynamic simulation study of AFM single-wall carbon nanotube tip-surface interactions. *In Key Engineering Materials*, 339, 206-210, 2007.
- [4] Fleck, N. A., and Hutchinson, J. W., Strain gradient plasticity. *Advances in applied mechanics*, 33, 296-361, 1997.
- [5] Hadjesfandiari, A. R., and Dargush, G. F., Couple stress theory for solids. *International Journal of Solids and Structures*, 48, 2496–2510, 2011.
- [6] Yang, F. A. C. M., Chong, A. C. M., Lam, D. C. C., & Tong, P., Couple stress based strain gradient theory for elasticity. *International Journal of Solids and Structures*, 39(10), 2731-2743, 2002.
- [7] Ma, H. M., Gao, X. L., Reddy, J. N., A microstructure-dependent Timoshenko beam model based on a modified couple stress theory. *Journal of Mechanics Physics and Solids*, 56, 3379–3391, 2008.
- [8] Reddy, J. N., Microstructure-dependent couple stress theories of functionally graded beams. *Journal of the Mechanics and Physics of Solids*, 59, 2382–2399, 2011.
- [9] Zhou, S. J., & Li, Z. Q., Length scales in the static and dynamic torsion of a circular cylindrical micro-bar. *Journal of Shandong university of technology*, 31(5), 401-407, 2001.
- [10] Akgöz, B., Civalek, O., Longitudinal vibration analysis for microbars based on strain gradient elasticity theory. *Journal of Vibration and Control*, 20(4), 606-616, 2014.
- [11] Asghari, M., Kahrobaian, M. H., Ahmadian, M. T., A nonlinear Timoshenko beam formulation based on the modified couple stress theory. *International Journal of Engineering Science*, 48(12), 1749-1761, 2010.
- [12] Akgoz, B., Civalek, O., Shear deformation beam models for functionally graded microbeams with new shear correction factors. *Composite Structures* 112, 214-225, 2014.
- [13] Akgöz, B., Civalek, O., Buckling analysis of cantilever carbon nanotubes using the strain gradient elasticity and modified couple stress theories. *Journal of Computational and Theoretical Nanoscience*, 8(9), 1821-1827, 2011.
- [14] Eringen, A. C., On differential equations of nonlocal elasticity and solutions of screw dislocation and surface waves. *Journal of applied physics*, 54(9), 4703-4710, 1983.
- [15] Eringen, A. C., *Nonlocal continuum field theories*. Springer Science & Business Media, 2002.
- [16] Chen, Y., Lee, J. D., Eskandarian, A., Atomistic viewpoint of the applicability of microcontinuum theories. *International journal of solids and structures*, 41(8), 2085-2097, 2004.
- [17] Peddieson, J., Buchanan, G. R., McNitt, R. P., Application of nonlocal continuum models to nanotechnology. *International Journal of Engineering Science*, 41(3), 305-312, 2003.
- [18] Sudak, L.J., Column buckling of multiwalled carbon nanotubes using nonlocal continuum mechanics. *Journal of Applied Physics*, 94, 7281–7287, 2003.

- [19] Ansari, R., Rajabiehfard, R., Arash, B., Nonlocal finite element model for vibrations of embedded multi-layered graphene sheets. *Computational Materials Science*, 49(4), 831-838, 2010.
- [20] Mahmoud, F. F., Eltahir, M. A., Alshorbagy, A. E., & Meletis, E. I., Static analysis of nanobeams including surface effects by nonlocal finite element. *Journal of Mechanical Science and Technology*, 26(11), 3555-3563, 2012.
- [21] Pradhan, S. C., Nonlocal finite element analysis and small scale effects of CNTs with Timoshenko beam theory. *Finite Elements in Analysis and Design*, 50, 8-20, 2012.
- [22] Phadikar, J. K., Pradhan, S. C., Variational formulation and finite element analysis for nonlocal elastic nanobeams and nanoplates. *Computational materials science*, 49(3), 492-499, 2010.
- [23] Eltahir, M. A., Alshorbagy, A. E., Mahmoud, F. F., Vibration analysis of Euler–Bernoulli nanobeams by using finite element method. *Applied Mathematical Modelling*, 37(7), 4787-4797, 2013.
- [24] Demir, Ç., Civalek, O., Torsional and longitudinal frequency and wave response of microtubules based on the nonlocal continuum and nonlocal discrete models. *Applied Mathematical Modelling*, 37(22), 9355-9367, 2013.
- [25] Civalek, O., Demir, C., A simple mathematical model of microtubules surrounded by an elastic matrix by nonlocal finite element method. *Applied Mathematics and Computation*, 289, 335-352, 2016.
- [26] Ansari, R., Gholami, R., Hosseini, K., Sahmani, S., A sixth-order compact finite difference method for vibrational analysis of nanobeams embedded in an elastic medium based on nonlocal beam theory. *Mathematical and Computer Modelling*, 54(11), 2577-2586, 2011.
- [27] Karimi, M., Shahidi, A. R., Finite difference method for sixth-order derivatives of differential equations in buckling of nanoplates due to coupled surface energy and nonlocal elasticity theories. *International Journal of Nano Dimension*, 6(5), 525, 2015.
- [28] Pradhan, S. C., Reddy, G. K., Buckling analysis of single walled carbon nanotube on Winkler foundation using nonlocal elasticity theory and DTM. *Computational Materials Science*, 50(3), 1052-1056, 2011.
- [29] Senthilkumar, V., Buckling analysis of a single-walled carbon nanotube with nonlocal continuum elasticity by using differential transform method. *Advanced Science Letters*, 3(3), 337-340, 2010.
- [30] Ebrahimi, F., Salari, E., Size-dependent free flexural vibrational behavior of functionally graded nanobeams using semi-analytical differential transform method. *Composites Part B: Engineering*, 79, 156-169, 2015.
- [31] Pradhan, S. C., Kumar, A., Vibration analysis of orthotropic graphene sheets using nonlocal elasticity theory and differential quadrature method. *Composite Structures*, 93(2), 774-779, 2011.
- [32] Pradhan, S. C., Kumar, A., Vibration analysis of orthotropic graphene sheets embedded in Pasternak elastic medium using nonlocal elasticity theory and differential quadrature method. *Computational Materials Science*, 50(1), 239-245, 2010.

- [33] Danesh, M., Farajpour, A., Mohammadi, M., Axial vibration analysis of a tapered nanorod based on nonlocal elasticity theory and differential quadrature method. *Mechanics Research Communications*, 39(1), 23-27, 2012.
- [34] Murmu, T., Pradhan, S. C., Thermo-mechanical vibration of a single-walled carbon nanotube embedded in an elastic medium based on nonlocal elasticity theory. *Computational Materials Science*, 46(4), 854-859, 2009.
- [35] Civalek, O., Demir, Ç., Bending analysis of microtubules using nonlocal Euler-Bernoulli beam theory. *Applied Mathematical Modeling*, 35, 2053-2067, 2011
- [36] Reddy, J.N., Nonlocal theories for bending, buckling and vibration of beams. *International Journal of Engineering Science*, 45, 288- 307, 2007.
- [37] Reddy, J. N., Pang, S. D., Nonlocal continuum theories of beams for the analysis of carbon nanotubes. *Journal of Applied Physics*, 103(2), 023511, 2008.
- [38] Mercan, K., Civalek, O., DSC method for buckling analysis of boron nitride nanotube (BNNT) surrounded by an elastic matrix, *Composite Structures*, 143, 300-309, 2016.
- [39] Baltacıoğlu, A.K., Akgöz, B., Civalek, O., Nonlinear static response of laminated composite plates by discrete singular convolution method, *Composite Structures*, 93, 153–161, 2010.
- [40] Civalek, O., Application of differential quadrature (DQ) and harmonic differential quadrature (HDQ) for buckling analysis of thin isotropic plates and elastic columns. *Engineering Structures*, 26, 171–186, 2004.
- [41] Demir, Ç., Mercan, K., Civalek, O., Determination of critical buckling loads of isotropic, FGM and laminated truncated conical panel, *Composites Part B: Engineering*, 94, 1-10, 2016.
- [42] Civalek, O., Finite Element analysis of plates and shells. Elazığ: Firat University, 1998.
- [43] Mercan, K., Ö Civalek, O., Buckling analysis of Silicon carbide nanotubes (SiCNTs) with surface effect and nonlocal elasticity using the method of HDQ, *Composites Part B: Engineering*, 114, 34-45, 2017.